Spin-orbit coupling in chaotic quantum dots

Ph.D. Thesis

Benjámin Béri

Department of Physics of Complex Systems

Eötvös Loránd University, Budapest

Advisor: Dr. József Cserti, CSc, habil. associate professor

Graduate School for Physics

Doctoral Program for Statistical Physics, Biological Physics, and Quantum Systems

Head of School: Prof. Dr. Zalán Horváth, regular member of HAS

Head of Program: Prof. Dr. Tamás Vicsek, regular member of HAS

2007

Acknowledgments

I would like to thank my advisor, Dr. József Cserti for his help and constantly available support through the ups and downs during my PhD studies. Without his optimism and encouragement the completion of this thesis would not have been possible.

I would like to thank Prof. Dr. Carlo Beenakker for giving me the opportunity to work with him on two projects on Andreev quantum dots, and for making it possible to have several visits at the Theoretical Nanophysics group of the Lorentz Institute in Leiden. I would like to thank Carlo and my colleague and collaborator Jens Bardarson for the many constructive discussions we had throughout our work together.

And finally, I would like to thank my family for constantly providing me a supportive environment during all these years.

Contents

Chapter 1

Introduction

The material presented in this thesis should be considered as a modest contribution to the theoretical knowledge about mesoscopic physics. Mesoscopic physics, a branch of the rapidly developing field of nanoscience, deals with the physics of systems that are intermediate between the microscopic and macroscopic world. These systems are much larger than atomic sizes, but still small enough that the aspects of quantum mechanics should be taken into account. An actively studied class of mesoscopic systems are mesoscopic electronic systems. At the present stage of semiconductor technology it is a routine task to fabricate samples of such systems. The characteristic length for quantum mechanics is the coherence length. This is the typical length an electron can travel without loss of quantum mechanical phase coherence. Having electronic systems in the mesoscopic regime, therefore, requires sizes much smaller than the coherence length. An important direction of experimental research on mesoscopic electronic systems focuses on studying the properties of structures created in a two dimensional electron gas (2DEG). The most frequently used 2DEG is the one formed at the interface of GaAs and n-doped AlGaAs layers. In GaAs/AlGaAs 2DEGs the coherence length exceeds tens of microns at temperatures of the order of few hundred mK. Quantum dots, structures created by confining the electrons to a small region in the 2DEG, are one of the most actively studied mesoscopic electronic systems. An experimental realization of a quantum dot is shown in Fig. 1.1.

In the past years mesoscopic electronic systems with spin-orbit coupling attracted considerable attention both theoretically and experimentally, mainly due to the emergence of novel concepts, such as spintronics and solid state spin qubits which are of a potential relevance to the electronics industry. (For a review on spintronics and spin-qubits see Ref. [1]) The work

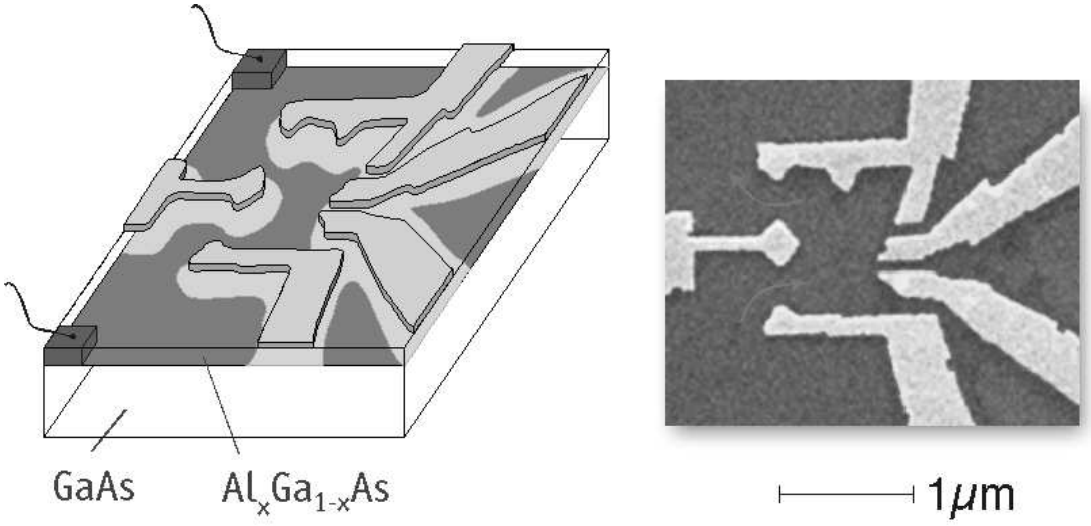

Figure 1.1: On the left is a schematic view of a quantum dot in a GaAs/AlGaAs 2DEG (the 2DEG is the dark grey area). The dot is defined by gates deposited on the top of the AlGaAs layer. A negative voltage applied to the gates depletes the 2DEG underneath (light grey area). On the right is a scanning electron micrograph of the dot. Figure taken from Ref. [2].

presented in this thesis deals with the effects of spin-orbit coupling in quantum dots. The questions discussed belong to two subbranches of the diverse field of quantum dot physics. The first type of questions deal with quantum effects in the transport through quantum dots. The questions of the second type are about the spectral properties of normal-superconducting heterostructures (Andreev billiards). The focus is on the generic situation that the classical dynamics in the dot is chaotic. In this case, a detailed description of an individual sample is not practically useful. The reason is that a slight change in the microscopic features of the system can significantly change the studied properties, such as the conductance or the size of the excitation gap in Andreev billiards. Instead, a statistical approach should be taken. The statistical ensemble consists of quantum dots with slight variation of the parameters defining the microscopic configuration, such as the details of the geometry or the Fermi energy. An analytical method for this statistical description is provided by Random Matrix Theory (RMT). This is the main theoretical tool used in this thesis.

The aim of the Introduction is to explain the aforementioned concepts in some detail and to provide some background information for the rest of the thesis.

1.1 Spin-orbit coupling in 2DEGs

For a non-relativistic electron in vacuum, the Dirac equation can be reduced to the Pauli equation, describing a two-component spinor and containing the Zeeman term. The Pauli equation also contains relativistic corrections—including the spin-orbit coupling

$$H_{\mathrm{SO,\,vac}} = \lambda_{\mathrm{vac}}\, \boldsymbol{\sigma} \cdot \left(\mathbf{k} \times \nabla \tilde{V}\right), \tag{1.1}$$

where $\boldsymbol{\sigma}$ is the vector of Pauli matrices and $\tilde{V}$ is the total potential acting on the electron. We used $\lambda_{\mathrm{vac}} = -\hbar^2/4m_0^2c^2$, vacuum electron mass m_0, velocity of light c, and $\mathbf{k} = \mathbf{p}/\hbar$.

Following the review of Engel *et al* [3] we briefly summarize how this relativistic correction manifests itself in a two dimensional electron gas (2DEG) formed at the interface of semiconductor heterostructures. In a semiconductor, we split the total potential $\tilde{V} = V_{\mathrm{cr}} + V$ into the periodic crystal potential V_{cr} and an aperiodic part V, which contains the potential due to confinement, boundaries, and external electrical field. One then tries to eliminate the crystal potential as much as possible and to describe the charge carriers in terms of the band structure. The Hamiltonian of electrons in a 2DEG stems from the effective Hamiltonian of electrons close to the bottom of the conduction band in the bulk semiconductor. In the absence of magnetic field it can be written as

$$H_{\mathrm{eff}} = \epsilon_k + V + H_{\mathrm{SO}}, \tag{1.2a}$$

$$H_{\mathrm{SO}} = \frac{1}{2}\, \mathbf{b}\left(\mathbf{k}\right) \cdot \boldsymbol{\sigma}, \tag{1.2b}$$

where $\mathbf{k} = -i\nabla$, and we assumed that V is only slowly varying on the scale of the lattice constant. The term H_{SO} describes the splitting of the spectrum due to spin-orbit coupling. The spin-orbit field $\mathbf{b}\left(\mathbf{k}\right)$ has the property $\mathbf{b}\left(\mathbf{k}\right) = -\mathbf{b}\left(-\mathbf{k}\right)$ due to time reversal symmetry. Therefore, for a three-dimensional system, $\mathbf{b}$ is nonzero only if the inversion symmetry is broken (bulk inversion asymmetry - BIA). The 2DEGs derive from (1.2a) by letting V to confine the electrons to two dimensions. It is then conventional to talk about the two-dimensional band structure of the system, and to include the confinement potential in ϵ_k and $\mathbf{b}\left(\mathbf{k}\right)$ (instead of including it explicitly in V). In this case $\mathbf{b}$ can also result from an asymmetry in the confinement (structure inversion asymmetry - SIA).

A routinely used 2DEG is the one formed at the interface of GaAs and AlGaAs layers

[4–7]. In GaAs, the bulk inversion asymmetry leads to the Dresselhaus term

$$H_{\mathrm{D,3d}} = \mathcal{B}\, k_x \left(k_y^2 - k_z^2\right) \sigma_x + \text{c.p.}, \tag{1.3}$$

where k_i are along the principal crystal axes. Here, c.p. stands for cyclic permutation of all indices. The prefactor $\mathcal{B}$ measures the strength of spin-orbit coupling [1].

When the electrons are confined to two dimensions, one should take the expectation value of the Dresselhaus term, $\langle H_{\mathrm{D,3d}} \rangle$, in the lowest lying mode of the confinement potential (we always assume the confinement to be along the z direction, which is taken to be [001]). While $\langle k_z \rangle = 0$, we see that the terms proportional to $\langle k_z^2 \rangle \approx (\pi/d)^2$ are large for small confinement width d, thus the main BIA contribution becomes

$$H_\beta = \beta \left(k_x \sigma_x - k_y \sigma_y\right), \tag{1.4}$$

with $\beta \approx -\mathcal{B}\,(\pi/d)^2$. In addition to the k-linear term in Equation (1.4), there is also a k^3-term,

$$H_{\mathrm{D,2d}} = \mathcal{B}\, k_x k_y \left(k_y \sigma_x - k_x \sigma_y\right), \tag{1.5}$$

which is small compared to H_β in the strong confinement limit $\pi/d \gg k_{\mathrm{F}}$, where k_{F} is the Fermi wave vector. Additionally, a spin-orbit coupling term arises if the confinement potential $V(z)$ along the z-direction is not symmetric, i.e., if there is a structure inversion asymmetry. It has a form similar to that Eq. (1.1) suggests,

$$H_\alpha = \alpha \left(k_y \sigma_x - k_x \sigma_y\right), \tag{1.6}$$

where $\alpha \propto \langle dV/dz \rangle$. The magnitude of the coupling constant α depends on the confinement potential and it can be in principle modified by applying an additional field via external gates [2].

Magnetic fields can be included using the minimal substitution $\hbar\mathbf{k} = -i\hbar\nabla - e\mathbf{A}$, where e is the electron charge and $\mathbf{A}$ is the vector potential. One also has to include the Zeeman term which is different from its form in vacuum by the appearance of an effective g factor.

Collecting the terms together, we find that the effective Hamiltonian in a 2DEG can be

[1] Its numerical value found from band structure calculations [8] is $\mathcal{B} \approx 27\,\mathrm{eV\AA}^3$. However, tight-binding calculations and interpretation of weak localization experiments indicate lower values [9,10].

[2] However, for single interface heterostructures such as GaAs/AlGaAs, α turns out to be determined mainly by the band offset at the heterointerface, which is roughly independent of the gate voltage [6].

written as

$$H_0 = \frac{\hbar^2 k^2}{2m^*} + U + \beta\left(k_x\sigma_x - k_y\sigma_y\right) + \alpha\left(k_y\sigma_x - k_x\sigma_y\right) + \frac{g^*}{2}\mu_B\boldsymbol{\sigma}\cdot\mathbf{B}, \tag{1.7}$$

where $\hbar\mathbf{k} = -i\hbar\nabla - e\mathbf{A}$ is the 2D kinetic momentum, $\mathbf{B} = \nabla\times\mathbf{A}$ is the magnetic field and we neglected the cubic Dresselhaus term (1.5). The parameters m^* and g^* are the effective mass and g factor, respectively. The potential term U allows for a further confinement in the lateral direction[3]. So far we have neglected the possibility of the presence of impurities. Electric fields due to impurities lead to further spin-orbit contributions, again of a similar form form that is suggested by (1.1).

1.2 Quantum transport

The subject of quantum transport is the transport through samples having a size of few hundred nanometers. On such length scales electrons maintain their phase coherence while propagating through the system. This means that it is essential to treat them quantum mechanically. In these mesoscopic devices novel transport phenomena show up that are not present in their classical analogs, such as the quantization of conductance in clean wires, weak (anti)localization, or the universal conductance fluctuations in chaotic conductors. Following the review of Beenakker [11] we give a brief summary of the elements of quantum transport that are used in the later parts of this thesis.

1.2.1 Scattering matrix approach

The scattering theory of electronic conduction is due to Landauer [12, 13], Imry [14], and Büttiker [15,16]. It provides a complete description of transport at low frequencies, temperatures, and voltages, under circumstances that electron-electron interactions can be neglected. (For an overview of the great variety of experiments in which the theory has been tested, see Ref [4].) A mesoscopic conductor is modeled by a phase-coherent scattering region (sample region) connected by ideal leads to two electron reservoirs (see Fig. 1.2). Ideal here means that it is assumed that any magnetic field, spin-orbit coupling or impurities are present only in the sample region not in the leads. Scattering in the phase-coherent region is elastic. All

[3]The lateral confinement is usually modeled with hard wall boundary conditions. In this case the spin-orbit coupling arising from U is inoperative.

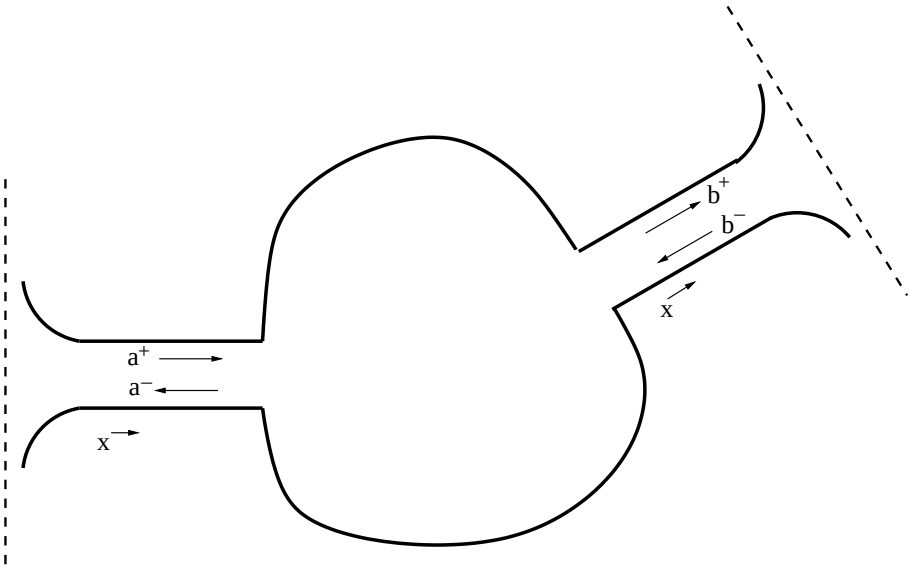

Figure 1.2: The sample as a scattering region connected by ideal leads to two electron reservoirs (to the left and right of the dashed lines). The scattering matrix S relates the amplitudes a^+, b^- of incoming waves to the amplitudes a^-, b^+ of outgoing waves.

inelastic scattering is assumed to take place in the reservoirs, which are in equilibrium at temperature zero and electrochemical potential (or Fermi energy) $E_{\rm F}$. The ideal leads are "electron waveguides", introduced to define a basis for the scattering matrix of the sample region.

The wavefunction ψ of an electron in a lead at energy $E_{\rm F}$ separates into a longitudinal and a transverse part,

$$\psi^{\pm}_{n\alpha\sigma}(\mathbf{r}\,) = \Phi_{n\alpha}(y)\exp(\pm {\rm i}k_{n\alpha}x)|\sigma\rangle, \tag{1.8}$$

where we assumed that the leads are two dimensional. The integer $n = 1, 2, \ldots N_\alpha$ labels the propagating modes in lead $\alpha = 1, 2$. The ket $|\sigma\rangle = |\uparrow\rangle,\ |\downarrow\rangle$ denotes the basis vectors in spin-space. The propagating modes are also referred to as scattering channels. Mode $n\alpha\sigma$ has a real wavenumber $k_{n\alpha} > 0$ and transverse wavefunction $\Phi_{n\alpha}$. The normalization of the wavefunction (1.8) is chosen such that it carries unit current. A wave incident on the scattering region is described in this basis by a vector of coefficients

$$c^{\rm in} \equiv (a^+_1, a^+_2, \ldots a^+_{N_1}, b^-_1, b^-_2, \ldots b^-_{N_2}), \tag{1.9}$$

where the coefficients have a further spinor structure. The first set of N_1 coefficients refers

to the left lead, and the second set of N_2 coefficients to the right lead in Fig. 1.2. Similarly, the reflected and transmitted wave has vector of coefficients

$$c^{\rm out} \equiv (a_1^-, a_2^-, \ldots a_{N_1}^-, b_1^+, b_2^+, \ldots b_{N_2}^+). \tag{1.10}$$

Denoting the total number of modes as $N = N_1 + N_2$, the scattering matrix S is a $N \times N$ matrix which relates these two vectors,

$$c^{\rm out} = S(E_{\rm F})c^{\rm in}, \tag{1.11}$$

where we denoted explicitly the energy dependence of S. It has the block structure

$$S = \begin{pmatrix} r_{N_1\times N_1} & t'_{N_1\times N_2} \\ t_{N_2\times N_1} & r'_{N_2\times N_2} \end{pmatrix}, \tag{1.12}$$

with reflection matrices r and r' (reflection from left to left and from right to right) and transmission matrices t and t' (transmission from left to right and from right to left). The indices in the block structure (1.12) refer to the dimensions of the submatrices. These dimensions do not include spin; the elements of S have a further matrix structure in spin space.

Current conservation implies that S is a unitary matrix: $S^{-1} = S^\dagger$. It is a consequence of unitarity that for the four Hermitian matrices $tt^\dagger$, $t't'^\dagger$, $1 - rr^\dagger$, and $1 - r'r'^\dagger$ the (sub)set of eigenvalues that can be nonzero is the same, $\{T_1, T_2, \ldots T_{2\min(N_1,N_2)}\}$. (The factor of 2 in $2\min(N_1, N_2)$ is due to the spin.) These eigenvalues are called transmission eigenvalues, and each of them is a real number between 0 and 1.

If the system is time-reversal invariant (absence of magnetic fields) the scattering matrix obeys the self duality condition $S = \sigma_2 S^T \sigma_2$, where the superscript T refers to matrix transposition. In this case the transmission eigenvalues are twofold degenerate. If spin-rotation invariance is present (absence of spin-orbit coupling) the scattering matrix is proportional to the unit matrix in spin-space. The self-duality constraint in this case implies that the scattering matrix is symmetric, $S = S^T$. In the presence of magnetic fields the unitarity of S is the only requirement. The two-fold degeneracy of the transmission eigenvalues is removed only if both the time-reversal and the spin-rotation invariance is broken.

1.2.2 Conductance, shot noise, linear statistics

The transmission eigenvalues determine a variety of transport properties. First of all the conductance $G = \lim_{V\to 0} \bar{I}/V$, defined as the ratio of the time-averaged electrical current $\bar{I}$ through the conductor and the voltage difference V between the two electron reservoirs — in the limit of vanishingly small voltage. This is the limit of linear response, to which we restrict ourselves in this thesis. At zero temperature, the conductance is given by

$$G = \frac{e^2}{h}\mathrm{Tr}\ tt^\dagger = \frac{e^2}{h}\sum_n T_n. \tag{1.13}$$

Equation (1.13) is known as the Landauer formula, because of Landauer's pioneering 1957 paper, Ref. [12].

In an ideal wire all the transmission eigenvalues are equal to unity. The conductance is then given as

$$G = \frac{2e^2}{h}N_1, \tag{1.14}$$

where the factor of two is due to spin. In a wire of width W, assuming hard wall boundary conditions, the number of propagating modes is given as $N_1 = N_2 = \mathrm{Int}(k_F W/\pi)$. As the width of the wire is increased continously, the conductance increases in steps of $2e^2/h$. This is the phenomenon of conductance quantization. Sometimes $2e^2/h$ is referred to as the conductance quantum.

The discreteness of the electron charge causes time-dependent fluctuations of the current $I(t) = \bar{I} + \delta I(t)$, which persist down to zero temperature. These fluctuations are known as shot noise. The power spectrum of the noise has the zero-frequency limit

$$P = 4\int_0^\infty dt\, \overline{\delta I(t+t_0)\delta I(t_0)}, \tag{1.15}$$

where the overline indicates an average over the initial time t_0 in the correlator. The shot-noise power is related to the transmission eigenvalues by the formula of Büttiker [17],

$$P = \frac{2e^3V}{h}\mathrm{Tr}\ tt^\dagger\left(1 - tt^\dagger\right) = \frac{2e^3V}{h}\sum_n T_n(1-T_n). \tag{1.16}$$

More generally, one can study transport properties of the form

$$A = \sum_{n=1} a(T_n). \tag{1.17}$$

The quantity A is called a linear statistic on the transmission eigenvalues. The word "linear" indicates that A does not contain products of different eigenvalues, but the function $a(T)$ may well depend non-linearly on T — as it does in the case of the shot-noise power (1.16), where $a(T)$ depends quadratically on T. The conductance (1.13) is special because it is a linear statistic with a linear dependence on T.

1.2.3 Weak (anti)localization

Weak (anti)localization is one of the most well known phenomena where the presence or absence of spin-orbit coupling has consequences on the transport properties. It is a quantum interference effect, therefore it requires that the carriers maintain their phase coherence: it becomes important in the quantum transport regime. The essence of the effect is a change in the return probability (as compared to the classical value) for time-reversal invariant systems. Approaching from the classical regime $\lambda_F \ll L$ where λ_F is the Fermi wavelength and L is the typical length scale of the system, this change shows up as an interference term, originating from pairs of geometrically identical return trajectories traversed in the opposite direction. We give here a qualitative description of the effect following the article of Bergmann [18].

Assuming an electron at position $\mathbf{x}$ in spin state $|s\rangle$ the probability of return to $\mathbf{x}$ is given by

$$P_R = \langle A|A\rangle, \tag{1.18}$$

where the amplitude is

$$|A\rangle = \sum_{\gamma} \rho_\gamma e^{i\phi_\gamma} R_\gamma |s\rangle. \tag{1.19}$$

This is an intuitive generalization of the Feynman path sum to spin-1/2 particles. In the sum only classical return trajectories γ are considered, and the spin is treated as evolved by the SU(2) matrix R_γ during the propagation along the trajectory. The real number ρ_γ is the weight of trajectory γ. The phase accumulated during the propagation along trajectory γ is

given by the classical action,

$$\phi_\gamma = \frac{1}{\hbar}\oint_\gamma \mathbf{p}d\mathbf{x} = \frac{1}{\hbar}\oint_\gamma m\mathbf{v}d\mathbf{x} - 2\pi\frac{\Phi_\gamma}{\Phi_0}. \tag{1.20}$$

Here Φ_γ is the flux[4] through the loop corresponding to γ and $\Phi_0 = h/e$ is the flux quantum. The probability is given by

$$P_R = \sum_\gamma \rho_\gamma^2 + \rho_\gamma\rho_{\gamma^{-1}}e^{-i4\pi\Phi_\gamma/\Phi_0}\left\langle s\left|R_{\gamma^{-1}}^\dagger R_\gamma\right|s\right\rangle, \tag{1.21}$$

where γ^{-1} is the trajectory γ traversed in the opposite direction. The first term is the classical return probability P_R^{cl}. The second term represents the interference of a trajectory with its opposite direction pair. We neglected the other terms, their contribution is expected to be small due to the large variation of the phase ϕ across the variety of return trajectories. In the following we calculate the average return probability. Considering a chaotic conductor, the averaging is over the parameters defining the microscopic configuration of the system; it can be over variations of the conductor boundary or over different realizations of a weak disorder. We assume that in the corresponding ensemble ρ_γ, ϕ_γ, and R_γ are independent random variables. Three limiting cases can be distinguished:

- There is no magnetic field, neither spin-orbit coupling. Then the weight ρ_γ and the action of a path is the same as for its opposite traversed pair, in accord with the time-reversal symmetry of the system. The spin-orbit "phase" is trivial, $R = 1$. The return probability is
$$P_R = 2P_R^{cl} \qquad (\beta = 1).$$

- The magnetic field is strong enough that the phase factor due to the flux is uniformly distributed on the unit circle in the complex plane[5]. In this case the interference correction is absent,
$$P_R = P_R^{cl} \qquad (\beta = 2).$$

- There is no magnetic field, but the spin-orbit coupling is strong enough that the spin-

[4] Throughout this thesis, the magnetic field is assumed to be such that its orbital effect is merely the appearance of an extra phase [cf. Eq. (1.20)], it does not affect the classical dynamics.

[5] This is achieved already for $\Phi \lesssim \Phi_0$, where Φ is the flux through the system. Such magnetic field does not conflict our assumption in Footnote 4. In this thesis, strong magnetic field means $\Phi \lesssim \Phi_0$ for the component perpendicular to the 2DEG's plane.

orbit "phase" is uniformly distributed in SU(2) (with respect to its Haar measure). Due to time-reversal symmetry the weight ρ_γ and the action of a path is the same as its opposite traversed pair, and $R_{\gamma^{-1}} = R_\gamma^{-1}$. Therefore, the quantity to average is $\langle s \left| R_\gamma^2 \right| s \rangle$. Averaging over SU(2) gives $\langle R_\gamma^2 \rangle = -1/2$, resulting in

$$P_R = \frac{1}{2} P_R^{cl} \qquad (\beta = 4).$$

We labeled the cases with an index β that will appear several times later in this thesis. The results can be summarized as

$$P_R = \frac{2}{\beta} P_R^{cl}. \tag{1.22}$$

The consequence of this enhancement(decrease) of the average return probability is a negative (positive) correction of order e^2/h to the classical average conductance. This correction is called weak localization correction [4, 19–21].

1.3 Random matrix theory for chaotic quantum dots

The idea to give a statistical description of the quantum properties of complex systems using random matrices comes from Wigner, who proposed this method in the context of nuclear resonance spectra [22]. Since his work Random Matrix Theory (RMT) has found application in many other fields of physics ranging from QCD to econophysics. The relevance of RMT for quantum chaos became clear after the work of Bohigas Giannoni and Schmidt [23]. They numerically showed that, statistically, quantum properties of chaotic billiards can very well be described by random matrices. In the RMT context, the adjective "chaotic" refers to [11] chaotic systems (neighboring trajectories diverge exponentially in time) which are ergodic (each trajectory approaches every point in the classical phase space arbitrarily closely).

Nanostructures corresponding to billiard systems can be created in 2DEGs, confining the electrons using metallic gates deposited on the surface of the heterostructure with negative voltage applied to them. Such systems are called quantum dots. Quantum mechanical phase coherence strongly affects their electronic properties, hence the adjective "quantum". In a quantum dot, electron motion is confined in all spatial directions. In this sense, quantum dots can be considered as zero dimensional – hence the name "dot".

The theoretical justification of the RMT method was given by Efetov [24,25] and Andreev

et al [26] using the supersymmetry technique and very recently by Müller *et al* [27, 28] based on a semiclassical approach. These calculations show that the RMT description for chaotic quantum dots is appropriate as long as one is interested in properties for which the relevant time scales are much longer than the electron transit time $\tau_{\rm fl}$. This is the time of flight of an electron across the quantum dot. For a quantum dot of typical linear size L and mean free path l, with Fermi velocity v_F it is $\tau_{\rm fl} = L^2/(v_F \min(l, L))$. On the language of energies, this condition means that the level correlations are described well by RMT as long as the energy separations considered are much smaller than $\hbar/\tau_{\rm fl}$. This implies $\delta \ll \hbar/\tau_{\rm fl}$ for the mean level spacing[6] δ. In the regime where the RMT description is valid, the statistical properties are the same no matter whether the system is diffusive ($L \gg l$) and the chaos is due to disorder, or ballistic ($L \ll l$) and the chaos is because of the shape of the boundaries. In this section we give a brief overview of the concepts of RMT relevant to this thesis. For a detailed monograph about RMT the reader is referred to the book of Mehta [29]. The method of applying RMT to transport problems is reviewed in Ref. [11].

1.3.1 RMT for closed quantum dots

The basic idea of the RMT approach to the description of chaotic quantum dots is the following: One chooses a discrete basis in the Hilbert space of the dot and represents the Hamiltonian as a matrix. If the dot is chaotic, the elements of this matrix are very sensitive to the slight variations of the boundary shape, or the disorder realization. For an ensemble of dots created by varying these components, the ensemble of Hamiltonians will be similar to one drawn from an ensemble of random matrices.

In the RMT approach one models the Hamiltonian matrix with a finite Hermitian matrix H of dimension $2M$ (the factor of two corresponds to spin). At the end of the calculations the limit $M \to \infty$ is taken. It is in this limit that the intuitive picture above can be made quantitative: the level correlations of chaotic systems become universal for energy separations much smaller than $\hbar/\tau_{\rm fl}$, once the energies are measured in units of the mean level spacing δ ($\ll \hbar/\tau_{\rm fl}$). The RMT approach reproduces these universal correlations in the limit $M \to \infty$ of large matrix size [23–25, 27, 28].

The matrix H should have the symmetries of the dot Hamiltonian. For chaotic dots the

[6] The energy levels of a chaotic quantum dot are twofold degenerate, unless both the magnetic field and spin-orbit coupling are nonzero. Usually δ refers to the mean spacing between the doublets.

only symmetries can be time-reversal and spin-rotation[7]. The presence or absence of these symmetries leads to the three fundamental symmetry classes of Dyson, usually labeled with the index β.

- $\beta = 1$: In the absence of magnetic fields and spin-orbit coupling there is both time-reversal and spin rotation symmetry. This requires H to be a real symmetric matrix. As spin-rotation symmetry is present, H is proportional to the unit matrix in spin space.
- $\beta = 2$: In the presence of magnetic fields time-reversal symmetry is broken. The only requirement for H is Hermicity. If spin-rotation symmetry is present H is proportional to the unit matrix in spin space.
- $\beta = 4$: In the absence of magnetic fields, but in the presence of spin-orbit coupling the system is time-reversal invariant, but there is no spin-rotation symmetry. In this case H can be written as

$$H = H_0 + i \sum_{k=1}^{3} \sigma_k A_k, \tag{1.23}$$

with

$$H_0 = H_0^T, \quad A_k = -A_k^T \tag{1.24}$$

being $M \times M$ real matrices.

The ensemble of Hamiltonians is represented with the probability distribution of H

$$P(H)dH \propto \exp\left[-\frac{\beta}{2s^2}\mathrm{Tr}\ V(H)\right]\ dH, \tag{1.25}$$

where V is some function of H and dH is the product of infinitesimals of independent matrix elements. The prefactor in the exponent is inserted for convenience. The index s counts the level degeneracy, it is $s = 1$ for $\beta = 2$ in the absence of spin-rotation symmetry, and $s = 2$ otherwise, corresponding to spin, or Kramers degeneracy. The distribution is invariant under basis transformations that preserve the symmetry of the Hamiltonian. These are orthogonal, unitary and symplectic transformations for $\beta = 1$, $\beta = 2$ and $\beta = 4$, respectively. For this reason, matrices distributed according to Eq. (1.25) are sometimes referred to as members of the orthogonal, unitary, symplectic ensembles. It turns out that in the limit of $M \to \infty$ the correlations of the eigenvalues of H are independent of V if the energies are measured in

[7] We assume that the systems under consideration have no spatial reflection symmetries.

units of the mean level spacing δ_{RMT} of the random matrices, provided that one stays away from the edge of the mean level density. This is the universality of RMT. The role of V is to determine the mean level density, and thus the mean level spacing. With this freedom of choosing V one usually considers the Gaussian ensemble, $V(H) = (1/v^2)H^2$. The advantage of this choice lies in its simplicity: the elements of H are independently distributed. Denoting the eigenvalues of H as $\{E_j\}$ and the RMT average with angular brackets, the mean level density $\rho(E)$ is given by the Wigner semicircle,

$$\rho(E) = \langle \sum_{j=1}^{2M} \delta(E - E_j) \rangle = \frac{1}{\pi v^2} \sqrt{4Mv^2 - E^2}. \tag{1.26}$$

Near the center of the semicircle, the mean level spacing is $\delta_{\mathrm{RMT}} = \pi v/(2\sqrt{M})$. Denoting with δ the mean spacing between the degenerate doublets (present for cases with $s = 2$), we have $\delta = 2\delta_{\mathrm{RMT}}$. (Unless it would lead to confusion, we do not make a distinction in the notation between the mean level spacing δ of the physical system and of the RMT model.)

Dyson's three symmetry classes corresponding to the different values of β can be considered as limiting cases of symmetry breaking. One can in general ask the question what is the adequate description of chaotic quantum dots that interpolate between these limits (this interpolation is sometimes called crossover between symmetry classes). For example, what is the critical strength of spin-orbit coupling that brings the system to the $\beta = 4$ class, or how certain quantities depend on the strength of spin-orbit coupling.

The answer can be formulated in the language of time scales [30]. In quantum mechanics, treating the symmetry breaking as perturbation, its strength can be characterized with the decay rate of an unperturbed eigenstate. According to the Fermi golden rule the average decay rate is given by

$$\frac{\hbar}{\tau_{\mathrm{pert}}} = 2\pi \langle |H_{ij}^{(\mathrm{pert})}|^2 \rangle \rho, \tag{1.27}$$

where $H_{ij}^{(\mathrm{pert})}$ denotes the typical matrix element of the symmetry breaking perturbation between the initial eigenstate (of the unperturbed Hamiltonian) and an other eigenstate with approximately the same energy. The angular brackets mean ensemble averaging. The factor ρ is the average density of states (accessible by transitions due to the perturbation) around the energy of the initial eigenstate. The symmetry is effectively broken on a time scale τ if $\tau \gg \tau_{\mathrm{pert}}$. The characteristic time of a given perturbation τ_{pert} can be calculated from microscopic theories. In RMT it is taken as an input parameter. We briefly discuss the

formulation of the interpolating RMT model for the simplest case of a $\beta = 1 \to 2$ transition. In this case $H_{\rm pert}$ is a perturbation due to a magnetic field applied perpendicular to the plane of the dot. The dot Hamiltonian is modeled as

$$H = (H_0 + \frac{\alpha}{\sqrt{M}}\, iX)\mathbb{I}_2,$$

where $\mathbb{I}_2$ is the unit matrix in spin space[8] and the real number α measures the strength of the perturbation. The matrices H_0 and X are of dimension $M \times M$, and they satisfy

$$H_0 = H_0^T, \quad X = -X^T,$$

where the superscript T refers to matrix transposition. Both matrices are distributed according to [9]

$$P(A) \propto \exp\left[-\frac{1+\alpha^2/M}{4v^2} AA^T\right]. \tag{1.28}$$

Using the Golden rule with $(\alpha/\sqrt{M})\; iX$ in place of $H_{\rm pert}$ and taking the RMT average, one finds the correspondence

$$\alpha = \sqrt{\frac{\pi\hbar}{2\tau_{\rm pert}\delta}}. \tag{1.29}$$

1.3.2 RMT for open quantum dots

Transport through a quantum dot can take place if the dot is coupled to two electron reservoirs and a voltage is applied between them. We concentrate our attention to the case that the coupling to the reservoirs is via quantum point contacts, i.e. narrow constrictions that can be very well modeled by ideal leads [4]. For a discussion of the case that the coupling is via tunnel barriers we refer the reader to the review [11].

The time scale of transport is the dwell time $\tau_{\rm dw}$, the typical time an electron spends in the quantum dot before escaping through the openings. A criterion for the applicability of RMT to transport calculations is therefore $\tau_{\rm dw} \gg \tau_{\rm fl}$. This ensures that the chaotic motion has enough time to develop before the electron exits the dot. This criterion is formulated

[8] The characteristic energy corresponding to the orbital effect of a perpendicular magnetic field [31,32] is $\hbar/\tau_{\rm B} \sim \hbar/\tau_{\rm fl}(\Phi/\Phi_0)^2$, where $\Phi_0 = h/e$ is the flux quantum. In the RMT regime $\hbar/\tau_{\rm B} \ll \hbar/\tau_{\rm fl}$, therefore, the Zeeman energy $E_{\rm Z} \sim \delta(\Phi/\Phi_0)$ is negligible.

[9] The factor $(1+\alpha^2/M)$ in the exponent ensures that the mean level spacing is fixed at $\delta = \pi v/\sqrt{M}$.

using classical quantities, since it is essentially a condition on the geometry: it is equivalent to $1 \ll L/W_\alpha$, where W_α is the width of the contacts, $\alpha = 1, 2$. There is an additional criterion to be fulfilled that is related to quantum mechanics. The applicability of RMT for calculating transport properties requires $\tau_{\rm dw} \gg \tau_E$, where τ_E is the typical time up to which electrons follow classical trajectories [33–36]. For point contacts of width W_α, the RMT limit $\tau_E \sim \tau_{\rm fl}$ corresponds to $N_\alpha \leq L/W_{1,2}$, where N_α is the number of modes in lead α and L is the typical linear size of the system [34].

In the spirit of the scattering matrix approach to quantum transport, an RMT model for the scattering matrix should be given. An important difference from the RMT of the dot Hamiltonian is that the scattering matrix S is a finite, $2N \times 2N$ (the factor of two is due to spin and N is the total number of modes) dimensional matrix. In experiments $N_1 = N_2 = 1$ can be realized, therefore, this RMT has physical relevance even for 4×4 matrices.

The starting point is the RMT model of a closed quantum dot. Using the matrix H modeling the Hamiltonian of the quantum dot, the scattering matrix can be written as [11, 37, 38]

$$S = 1 - 2\pi i W^\dagger (E_{\rm F} - H + i\pi W W^\dagger)^{-1} W, \tag{1.30}$$

where the $2M \times 2N$ matrix W describes the coupling between the dot and the leads. It is given by

$$W_{mn} = \delta_{mn} \left(\frac{M\delta}{\pi^2} \right)^{1/2}, \; m = 1, 2, \ldots 2M, \; n = 1, 2, \ldots 2N.$$

In the limiting cases of Dyson's symmetry classes and in the limit $M \to \infty$, the result for the distribution of the scattering matrix is appealingly intuitive [39]: for a given energy $E_{\rm F}$, the scattering matrix S is uniformly distributed in the unitary group, subject only to the symmetry and self-duality constraints imposed by time-reversal and spin-rotation symmetry (see Sec. 1.2.1). Uniformity is defined with respect to the Haar measure $d\mu(S)$ which is invariant under multiplication: $d\mu(S) = d\mu(USV)$ for arbitrary unitary matrices U, V such that the product USV still satisfies the constraints imposed on S. (This requires $V = U^{\rm T}$ for $\beta = 1$ and $V = \sigma_2 U^T \sigma_2$ for $\beta = 4$.) The probability distribution is thus given by

$$P(\{x_n\}) \prod_i dx_i = \frac{1}{\mathcal{V}} \, d\mu(S), \tag{1.31}$$

where $\mathcal{V} = \int d\mu(S)$ is the volume of the matrix space and $\{x_n\}$ is a set of independent variables parameterizing S. The ensembles of matrices that are described by the distribution

(1.31) are called circular orthogonal (COE), unitary (CUE), symplectic (CSE) ensembles for $\beta = 1$, $\beta = 2$ and $\beta = 4$, respectively. (The name "circular" originates from the fact that (1.31) implies that the density of eigenvalues of S is uniform on the unit circle in the complex plane.)

To relate the RMT method to our discussion in Sec. 1.2.3 we give the result [11, 40] for the conductance following from the distribution(1.31). According to the Landauer formula (1.13), the average conductance $\langle G \rangle$ is obtained from the scattering matrix as

$$\langle G \rangle = \frac{e^2}{h} \sum_{n=1}^{N_1} \sum_{m=N_1+1}^{N} \sum_{\sigma,\sigma'} \langle |S_{nm\ \sigma\sigma'}|^2 \rangle. \tag{1.32}$$

Performing the RMT average the result is

$$\langle G \rangle = \frac{2e^2}{h} \left[\frac{N_1 N_2}{N} + (1 - \frac{2}{\beta}) \frac{N_1 N_2}{N(N - (1 - 2/\beta))} \right]. \tag{1.33}$$

The first term is $G_{\text{series}} = (1/G_1 + 1/G_2)^{-1}$, the classical series conductance of the two point contacts, where G_α is given according to Eq. (1.14). The second term is the weak localization correction, which is negative for $\beta = 1$, zero for $\beta = 2$, positive for $\beta = 4$.

For the description of the scattering matrix in the case of crossovers between symmetry classes there are two equivalent choices. One obvious way is to use the interpolating RMT Hamiltonian in (1.30). An alternative way is a parameterization of the scattering matrix introduced by Brouwer *et al* [41]. Consider that the crossover RMT Hamiltonian is given by

$$H = H_0 + \frac{x}{\sqrt{M}} H_1, \tag{1.34}$$

where H_0, H_1 Hermitian $2M \times 2M$ matrices, and the real number x measures the strength of the perturbation causing the crossover. The unperturbed matrix H_0 is from the orthogonal ensemble, H_1 is a random matrix with the same mean level spacing as H_0. In the alternative approach of Ref. [41], the scattering matrix is parameterized as

$$S = PU(1 - RU)^{-1} P^\dagger, \tag{1.35}$$

with

$$R = Q^\dagger r Q. \tag{1.36}$$

In the above expression U is a $(2N + 2N_s) \times (2N + 2N_s)$ random unitary symmetric matrix (the factors of two in the dimension are due to spin) taken from the COE and r is a unitary matrix of size $2N_s$. The $2N \times (2N + 2N_s)$ matrix P and the $2N_s \times (2N + 2N_s)$ matrix Q are projection matrices with $P_{ij} = \delta_{i,j}$ and $Q_{ij} = \delta_{i+2N,j}$. The matrix r is given by

$$r = \exp\left[-\frac{2\pi i}{M'^{3/2}\delta}\, xA\right], \tag{1.37}$$

where $M' = N + N_s$ and A is a $2N_s \times 2N_s$ random Hermitian matrix taken from the same ensemble as H_1. As proven in Ref. [41], the parameterization (1.35) with r as (1.37) and the parameterization (1.30) with the Hamiltonian (1.34) become equivalent in the limit $M, N_s \to \infty$.

1.3.3 A numerical model: quantum kicked rotator

In the previous sections we have briefly reviewed the RMT method which is a tool for obtaining analytical results for quantum chaotic systems. A possibility for comparing these calculations with numerical simulations is based on creating an ensemble using numerically generated random matrices. But this method still has the RMT model as an input. Instead, it would be more desirable to test the results in "real life" systems, i.e. using dynamical models of quantum chaos. In this section we briefly summarize how this can be done using quantum maps.

Our goal is to simulate the behavior of quantum dots. To see how quantum maps can serve this purpose, it is an instructive first step to summarize how to simulate classical billiards with classical maps. If one is interested about time scales much larger than the typical time between collisions with the billiard boundaries, to describe the dynamics it suffices to keep track with the bounces off the billiard walls. This description uses two coordinates, the position $s \in (0, 1)$ along the boundary (normalized by the total circumference) and the angle of incidence $\phi \in (-\pi/2, \pi/2)$. This procedure is one way to create a so called Poincaré surface of section. The dynamics in the billiard is described by the Poincaré map

$$(s_{n+1}, \sin(\phi_{n+1})) = F(s_n, \sin(\phi_n)). \tag{1.38}$$

The map is area preserving because the Hamiltonian of the billiard does not depend on time [42].

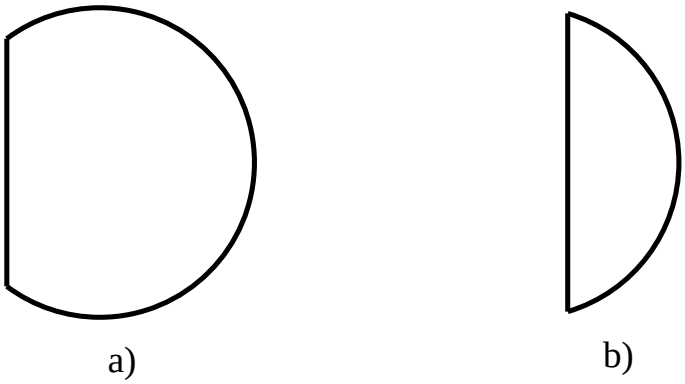

Figure 1.3: Geometry of the cut-circle billiard. The x coordinate of the cut, x_0 (in units of the circle radius R) controls the nature of the dynamics. For $x_0 < 0$ (Fig. a) the billiard displays hard chaos, for $x_0 > 0$ (Fig. b) the system shows soft chaos. The half circle corresponding to $x_0 = 0$ is integrable.

If the motion inside the billiard is chaotic, the map generates points that look randomly placed in the surface of section. In the opposite limit of regular motion the Poincaré map follows smooth curves in the surface of section. Chaotic systems where all initial conditions result in chaotic motion are said to exhibit "hard chaos". There are systems where some of initial conditions result in chaotic, some to regular motion. These chaotic systems exhibit "soft chaos". The systems where all initial condition correspond to regular motion are called regular or integrable. The chaotic systems referred to in the context of RMT show hard chaos. An example for the Poincaré map is shown in Fig.1.4 for the case of the cut-circle billiard (Fig. 1.3) studied in Ref. [43]. Depending on the position of the cut, this system can be regular, or display hard or soft chaos.

Besides being area conserving, the key property of the Poincaré map of chaotic systems is its nonlinearity. This observation leads to the idea to model chaotic systems by modeling the Poincaré map with some other area preserving nonlinear map. A famous example is the standard map,

$$\theta_{n+1} = \theta_n + p_n + \frac{K}{2}\sin(\theta_n), \tag{1.39a}$$

$$p_{n+1} = p_n + \frac{K}{2}\left(\sin(\theta_n) + \sin(\theta_{n+1})\right). \tag{1.39b}$$

The map is periodic both in θ and p with periodicity of 2π. Consequently, the dynamics can be described in a phase space that has a topology of a torus. The standard map is integrable

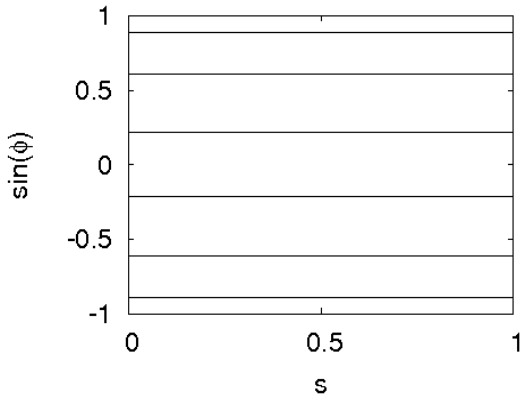

a. Cut-circle billiard, $x_0 = 0$.

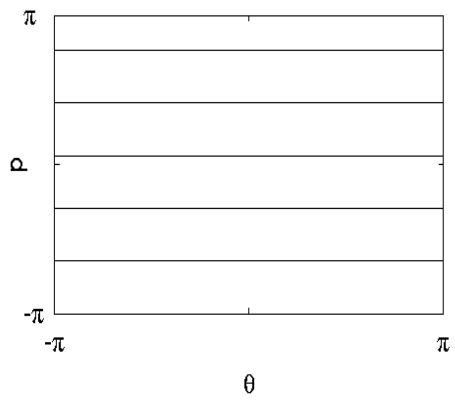

b. Standard map, $K = 0$.

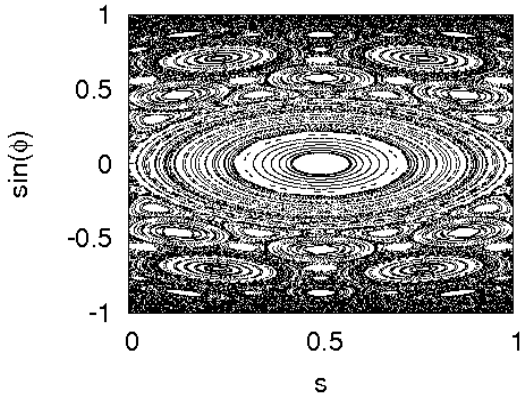

c. Cut-circle billiard, $x_0 = 0.1$.

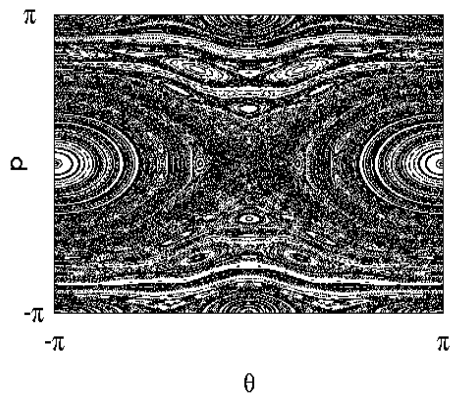

d. Standard map, $K = 0.9$.

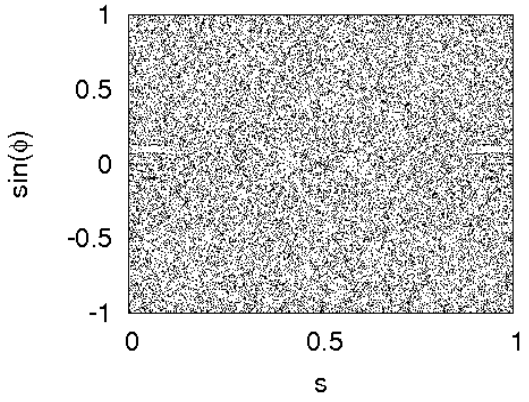

e. Cut-circle billiard, $x_0 = -0.1$.

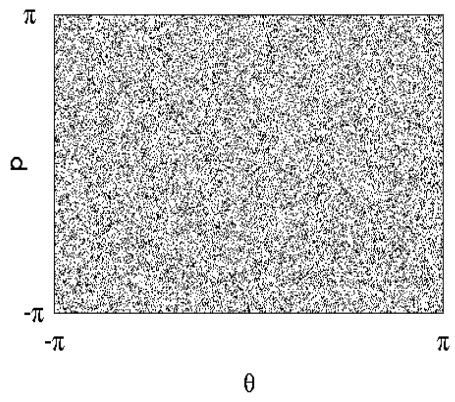

f. Standard map, $K = 41$.

Figure 1.4: Comparison of the Poincaré map of the cut-circle billiard (corresponding to bounces off the circular part of the boundary) with the standard map. The phase space portraits in the integrable cases (Fig. a and b) show the orbits of ∼30 initial conditions iterated 2000 times. The soft chaos cases (Fig. c and d) were run from ∼ 500 initial conditions for ∼200 iterations. In the cases of hard chaos (Fig. e and f) one initial condition was iterated 40000 times. For the standard map, due to its periodicity, only the unit torus $\theta \in [-\pi, \pi)$, $p \in [-\pi, \pi)$ is shown.

for $K = 0$ and for $K > 0$ it undergoes a transition to chaos. From Fig. 1.4 it is seen that the map has the same qualitative behavior as the Poincaré map of billiard systems.

With this preparation we now turn to the simulation of quantum billiards (quantum dots) using quantum maps with the standard map as an example. The key observation is that the standard map (1.39) can be deduced from the Hamiltonian

$$H(t) = \frac{p^2}{2} + K\cos(\theta)\sum_{m=-\infty}^{\infty}\delta_s(t-n), \tag{1.40}$$

where $\delta_s(t) = [\delta(t+\epsilon)+\delta(t-\epsilon)]/2$ is the symmetrized delta function, with ϵ an infinitesimal [10] . Expression (1.40) can be interpreted as the Hamiltonian of a rotator (a particle freely moving along a circle) with moment of inertia I_0, kicked periodically at time intervals τ_0 with a kicking strength that is a function of the angle θ. In this interpretation, the Hamiltonian (1.40) uses energy units I_0/τ_0^2, time units τ_0, and $p = \tau_0 J/I_0$ is a dimensionless momentum variable, with J being the angular momentum. The standard map gives a stroboscopic description of the time evolution, it keeps track with the dimensionless conjugate variables θ, p at integer values of t. Therefore, using the Poincaré map analogy, the stroboscopic time τ_0 corresponds to the the typical time between bounces off the billiard boundary.

The quantization of the standard map is done by imposing the canonical commutation relation

$$[\hat{\theta}, \hat{p}] = i\hbar_{\text{eff}}, \tag{1.41}$$

where $\hbar_{\text{eff}} = \hbar\tau_0/I_0$ in the rotator interpretation. The stroboscopic description in the quantum model amounts to keeping track with the wavefunction at integer values of t,

$$|\psi_{n+1}\rangle = \mathcal{F}|\psi_n\rangle, \tag{1.42}$$

where the unitary Floquet operator is

$$\mathcal{F} = \mathrm{T}\exp\left[-\frac{i}{\hbar_{\text{eff}}}\int_0^1 H(t)dt\right]. \tag{1.43}$$

Here T denotes time ordering of the exponential. For $\hbar_{\text{eff}} = 4\pi/M$, with M an integer,

[10] The equations (1.39) are sometimes referred to as the symmetrized standard map, where the word symmetrized refers to the property that the time evolution deriving from the Hamiltonian (1.40) is recorded at times which reflect the $t \to -t$ symmetry of $H(t)$.

the Floquet operator reduces to an $M \times M$ matrix. This choice is known as a resonance condition [44]. In the corresponding finite dimensional Hilbert space we denote the basis states of $\hat{\theta}$ and $\hat{p}$ as $|\theta_n\rangle$, $|p_n\rangle$, $n = 0, 1, \ldots, M-1$. They obey

$$\hat{\theta}|\theta_n\rangle = 2\pi\frac{n}{M}|\theta_n\rangle, \tag{1.44a}$$

$$\hat{p}|p_n\rangle = 4\pi\frac{n}{M}|p_n\rangle, \tag{1.44b}$$

and are related as

$$\langle\theta_n|p_m\rangle = \frac{1}{\sqrt{M}}\exp\left(i\frac{2\pi}{M}nm\right). \tag{1.45}$$

The eigenvalues in (1.44) suggest the interpretation of the finite Floquet matrix as a mapping on the torus $\theta \in [0, 2\pi)$, $p \in [0, 4\pi)$. The resonance condition thus corresponds to quantizing the classical dynamics on a phase space with a torus topology.

The Floquet matrix has M unimodular eigenvalues $\exp(-i\varepsilon_\nu)$ and orthonormal eigenvectors $|\nu\rangle$,

$$\mathcal{F}|\nu\rangle = e^{-i\varepsilon_\nu}|\nu\rangle. \tag{1.46}$$

The real numbers ε_ν are called the quasienergies. In the Poincaré map analogy they correspond to the energy levels of the quantum dot. The M dimensional Hilbert space the Floquet matrix acts upon will be called dot Hilbert space.

In order to simulate quantum dots that interpolate between Dyson's symmetry classes we use a generalized Hamiltonian instead of Eq. (1.40), the symplectic kicked rotator [45,46]

$$H = \frac{1}{2}(p + p_0)^2 + V(\theta)\sum_{n=-\infty}^{\infty}\delta_s(t-n), \tag{1.47a}$$

$$V(\theta) = K\cos(\theta + \theta_0) + K_{\mathrm{so}}(\sigma_1 \sin 2\theta + \sigma_3 \sin\theta). \tag{1.47b}$$

This Hamiltonian results in a $2M \times 2M$ Floquet matrix if the resonance condition is fulfilled (The factors of two are due to spin). Spin-rotation symmetry is present if $K_{\mathrm{so}} = 0$. The generalized time-reversal symmetry [45]

$$\mathcal{T}: \quad \theta \mapsto -\theta, \quad p \mapsto p, \quad \sigma_i \mapsto -\sigma_i, \quad t \mapsto -t, \tag{1.48}$$

is preserved if $\theta_0 = 0$ and is broken if $\theta_0 \in (0, \pi)$. A nonzero p_0 ensures that the Hamiltonian

has no other unitary or antiunitary symmetries [45]. The transformation properties of θ are dictated once $\sigma_i \mapsto -\sigma_i$ under time-reversal is imposed: if θ is not transformed it would be impossible to have a time-reversal invariant H with nonzero $K_{\rm so}$. The way p and θ are transformed under time-reversal suggest that in the Poincaré map analogy p and θ correspond to s and $\sin(\phi)$, respectively.

So far we have discussed how the quantum map deduced from the kicked rotator models closed quantum dots. In order to model a quantum dot with two leads attached to it, the quantum map should be opened up [47–51]. This is done by coupling a subspace of the dot Hilbert space to the Hilbert space of the lead modes. In the Poincaré map analogy p corresponds to the position along the billiard boundary. Consequently, in the classical phase space, the positions where the leads are attached to the dot correspond to strips parallel to the θ-axis. Therefore, we choose the subspace spanned by $\hat{p}$ eigenstates corresponding to the "position of the leads" to be coupled to the lead modes.

The dynamics of the open system is given by [47]

$$\begin{pmatrix} \psi_{n+1} \\ \phi_{n+1}^{(\rm out)} \end{pmatrix} = \begin{pmatrix} (1-P^TP)\mathcal{F} & P^T \\ P\mathcal{F} & 0 \end{pmatrix} \begin{pmatrix} \psi_n \\ \phi_{n+1}^{(\rm in)} \end{pmatrix}, \tag{1.49}$$

where ψ_m is a $2M$ dimensional vector describing the state in the dot. Lead α supports N_α modes, $\alpha = 1, 2$. The amplitudes of incoming and the outgoing lead modes are collected in the $2N = 2(N_1 + N_2)$ dimensional vectors $\phi_m^{(\rm in)}$ and $\phi_m^{(\rm out)}$, respectively. In Eq. (1.49) it is assumed that $\mathcal{F}$ is written in p representation. The $2N \times 2M$ projection matrix P is

$$P_{kk'} = \begin{cases} \mathbb{I}_2 & \text{if } k' = l_k^{(\alpha)}, \\ 0 & \text{otherwise.} \end{cases} \tag{1.50}$$

where $\mathbb{I}_2$ is the unit matrix in spin space. In the indices $l_k^{(\alpha)}$ the subscript $k = 1, 2, \ldots N$ labels the modes (both spin directions), and the superscript α labels the leads.

The interpretation of the dynamics (1.49) is quite clear: the dot state is evolved for one period by $\mathcal{F}$ and at the end of the period, the projection of the dot state at the leads is taken as outgoing state ("absorption") and the ingoing state is added to to the dot state components at the leads ("injection"). In the chaotic regime, starting from one $\hat{p}$ eigenstate in the dot, it is equally probable to end in any of the $\hat{p}$ eigenstates after one period. The probability of absorption after one period is thus N/M, which leads to $\tau_{\rm dw} = M/N$ for the

dwell time of the open system (in units of the stroboscopic time).

If the vector $\Psi = (\psi, \phi^{(\mathrm{in})}, \phi^{(\mathrm{out})})$ represents a scattering state (an energy eigenstate of the open system), its time evolution is $\Psi_n = \exp(-i\varepsilon n)\Psi_\varepsilon$, where ε corresponds to the energy of the scattering state (Fermi energy). This time evolution implies

$$\phi_\varepsilon^{(\mathrm{out})} = S(\varepsilon)\phi_\varepsilon^{(\mathrm{in})}, \qquad S(\varepsilon) = P[e^{-i\varepsilon} - \mathcal{F}(1 - P^T P)]^{-1}\mathcal{F}P^T. \tag{1.51}$$

The $2N \times 2N$ matrix $S(\varepsilon)$ can be identified with the scattering matrix of the system. It is unitary, and fulfills the symmetry and self-duality constraints following from the symmetries present.

We conclude the section about quantum maps with briefly discussing how the kicked rotator model is used to test the predictions of RMT in numerical simulations. Focusing on the transport properties, the scheme is to generate a statistical ensemble of scattering matrices using the definition in Eq. (1.51). The ensemble consists of scattering matrices with different values of K, ε, and different lead positions. The Floquet matrix can be calculated numerically efficiently using the fast-Fourier-transformation algorithm, which enables a fast calculation of the scattering matrix. This method is numerically much more tractable than a direct simulation of quantum dots by solving the 2D Schrödinger equation and generating the statistical ensemble by varying the dot parameters. With the kicked rotator several hundred lead modes are well within reach, as opposed to 2D billiard simulations where to date, $N \sim 50$ is the limit.

1.3.4 Some details that were not discussed

The basic assumption of the scattering matrix approach is that electron-electron interactions (more precisely, interactions between quasiparticles beyond the effective mass approximation) can be neglected and that electrons maintain their phase coherence while propagating through the sample. Before going on, is worthwhile to discuss how much these criteria are fulfilled in experiments. In chaotic quantum dots the most important effect of electron-electron interactions is the capacitive charging of the quantum dot [52]. This dominates transport in the form of Coulomb blockade in the case that the quantum point contacts connecting the dot to the reservoirs have conductances much smaller than e^2/h. Experiments [5, 7, 53] show that the noninteracting RMT describes the transport well already in the case of single channel point contacts with conductances $2e^2/h$. The temperatures of these experiments

range from tens to few hundred mK. In this case the phase coherence length is much larger than the typical system size, consequently, the phase coherence time τ_ϕ is much larger than the electron transit time $\tau_{\rm fl}$. For full phase coherence, however the relation $\tau_{\rm dw}/\tau_\phi \to 0$ is needed, which is not completely fulfilled, the ratio is small but finite. The finiteness of this ratio is the remaining effect of electron-electron interactions, which are the main source of dephasing at such low temperatures [54, 55]. The scattering formalism can be extended to handle finite phase coherence times [56–61], this extension is needed to reach such a good agreement with the experiments. In our calculations we assume zero temperature, then the ratio $\tau_{\rm dw}/\tau_\phi$ is expected to be zero [54, 55] [11].

In the preceding sections we described the crossovers between Dyson's symmetry classes by taking the decay rates corresponding to the different ways of symmetry breaking as an input (cf. Eq. (1.29)). The symmetry class transitions are achieved by tuning these decay rates. Here we briefly discuss how this tuning can be done in practice. The crossovers $\beta = 1 \to 2$, $\beta = 4 \to 2$ simply correspond to varying the strength of a perpendicular magnetic field. To achieve the $\beta = 1 \to 4$ transition for transport properties, one has to change the ratio $\tau_{\rm dw}/\tau_{\rm so}$, where $\tau_{\rm so}$ is the spin-orbit time. The Hamiltonian (1.7) suggests the naive picture of tuning the coupling constants α and β. In reality however, for quantum dots created in GaAs/AlGaAs heterostructures, the values of α and β are practically fixed [6]. In experiments, the tuning of $\tau_{\rm dw}/\tau_{\rm so}$ is achieved by varying the dot size [5], as follows from the theory of Aleiner and Falko [31], or by changing the electron density [5, 6].

The theory of Aleiner and Falko [31] also predicts that the interplay of the dot size dependence of the spin-orbit coupling strength and a magnetic field applied in the plane of the quantum dot can realize symmetry classes beyond Dyson's threefold classification scheme. The validity of their prediction was experimentally demonstrated in Refs. [5, 7]. For the details of the theory and the extension of the symmetry classification we refer the reader to Refs. [31, 77]. The chapters in this thesis that deal with crossovers can be understood without a deeper discussion about these results.

[11] As a matter of fact, this expectation is a subject of an intensive debate [62–73], due to the experimentally observed saturation of dephasing times as the temperature was lowered [74–76].

1.4 Excitation spectrum of normal-superconducting systems

If a quantum dot is brought in contact with superconductors a new type of quantum dot is created, a so called Andreev quantum dot, or Andreev billiard [78] (See Fig. 1.5). The name derives from the unusual reflection at the interface between a normal metal (N) and a superconductor (S) discovered by Andreev [79] in 1964. The reflection process is illustrated in Fig. 1.6. On the superconducting side there are no states with excitation energy (relative to the Fermi energy, which is assumed to be the same for the N and S regions) smaller than the superconducting gap Δ. Therefore, an electron incident from the normal metal with excitation energy $E < \Delta$ cannot enter the superconductor. It can either be reflected in the usual way (normal reflection), i.e. as it happens at an insulating interface (Fig. 1.6, left), or it can grab an other electron and they can enter the superconductor together as a Cooper pair. This can be interpreted as the incident electron being reflected as a hole. The hole is reflected in the direction of the incidence (retroreflection), due to the fact that the Cooper pairs are formed by pairs of electrons in states that are related to each other through time-reversal. The charge is not conserved in such a reflection, since the electron is negatively, the hole is positively charged. The group velocity of a hole points to the opposite direction of its momentum, so momentum is conserved. In contrast, normal reflection conserves charge but not momentum. This anomalous reflection together with its counterpart, when an incident hole is retroreflected as an electron is called Andreev reflection. For $\Delta \ll E_{\mathrm{F}}$ and in the absence of a barrier at the NS interface the dominant reflection process is Andreev reflection, the probability of normal reflection can be neglected.

The process of Andreev reflection is the key feature that is behind the qualitative differences between normal quantum dots and quantum dots with NS interfaces. Classically, for an ergodic system, any initial condition leads to a complete exploration of the boundary, i.e. there are no (stable) periodic orbits. In contrast, the presence of a superconducting segment renders every orbit periodic [12]. Quantum mechanically, the energy spectrum of normal dots can be compared to the spectrum of Andreev levels (excitation energies of Andreev billiards below Δ). The presence of superconducting interfaces brings an additional energy scale, the superconducting gap Δ to the problem. Depending on the relative magnitude of Δ and $\hbar/\tau_{\mathrm{dw}}$

[12] More precisely, the orbits become almost periodic, since incident and Andreev reflected trajectory segments are only approximately parallel for nonzero E. For a detailed discussion of this point see Ref. [78] and the references therein.

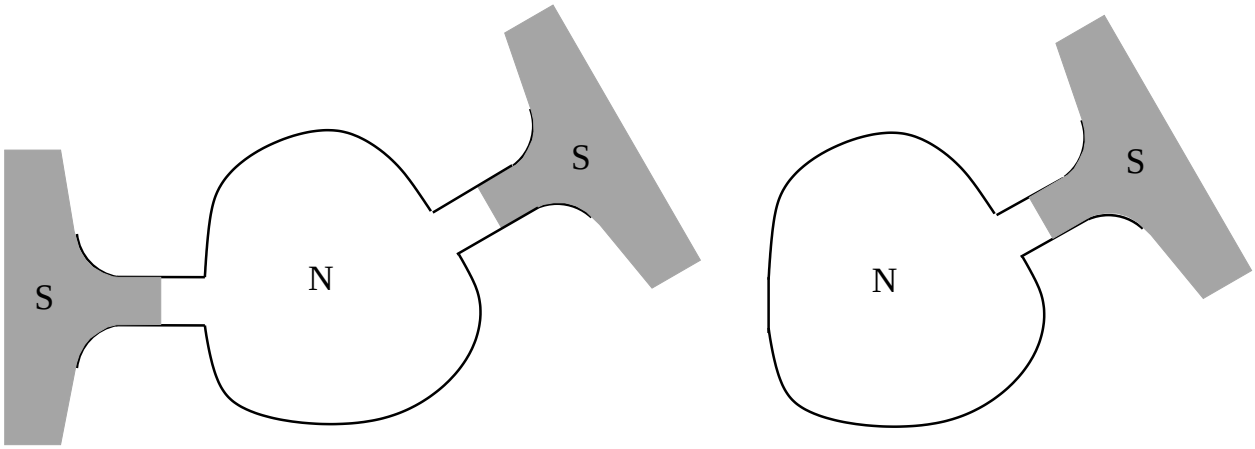

Figure 1.5: Sketch of Andreev quantum dots. The superconductor(s) (S) are brought in contact with the normal region (N) through quantum point contacts. In the case of two superconductors (left), the phases of the superconductors can be different.

($\tau_{\rm dw}$ is the dwell time corresponding to the open quantum dot without superconductors), two different limits can be studied. The Andreev level spectrum is qualitatively different in the two cases. In the limit $\Delta\tau_{\rm dw}/\hbar \ll 1$, for a Josephson junction, i.e. in the case that the quantum dot is connected to two superconductors with a phase difference ϕ, in zero magnetic field, the Andreev levels are determined by the normal state transmission eigenvalues introduced in Sec. 1.2.1. The relationship is [80]

$$E_n = \Delta\sqrt{1 - T_n \sin^2(\phi/2)}. \tag{1.52}$$

Expression (1.52) assumes that the quantum dot is contacted to the superconductors through leads that support the same number of propagating modes. To translate this result to the case of an Andreev billiard with one superconductor, we split up the scattering matrix of the normal region artifically to reflection and transmission blocks. The phase difference ϕ is zero, therefore all Andreev levels are just below Δ. In the opposite limit $\Delta\tau_{\rm dw}/\hbar \gg 1$, there are many (much more than the number of modes in the contacts) Andreev levels with an average spacing that is half the level spacing corresponding to the closed normal billiard. The level density is suppressed at sufficiently low excitation energies [81–84]. This suppression may take the form of an excitation gap, at an energy $E_{\rm gap}$ well below the gap Δ in the bulk superconductor (hence the name "minigap"). It may also take the form of a level density that vanishes smoothly (typically linearly) upon approaching the Fermi level, without an

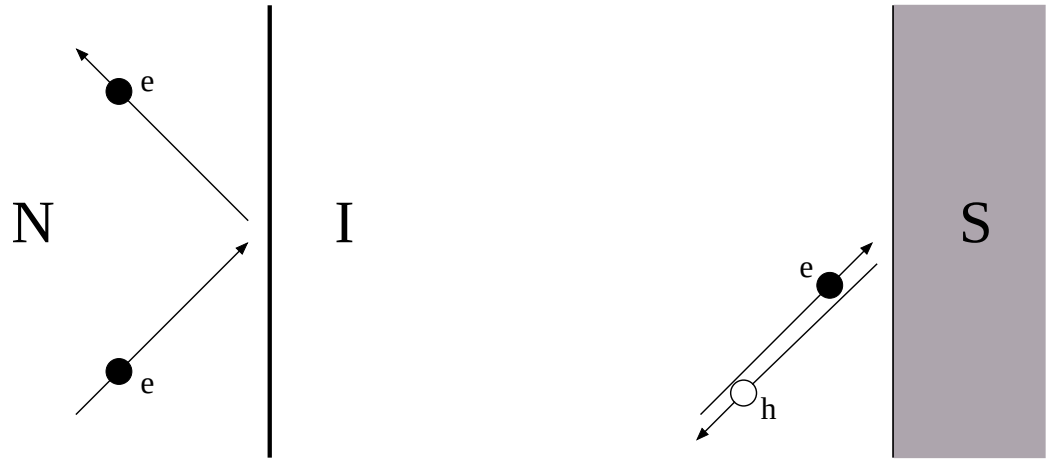

Figure 1.6: Normal reflection by an insulator (I) versus Andreev reflection by a superconductor (S) of an electron excitation in a normal metal (N) near the Fermi energy E_F.

actual gap. The presence or absence of a gap is a quantum signature of chaos [83]. That is a fundamental difference between normal billiards and Andreev billiards, since in a normal billiard the level density can not distinguish chaotic from integrable classical dynamics, for that one has to study level correlations.

In this thesis, the studies of Andreev quantum dots are focused on the spectral properties in the energy range $E < \Delta$. In the next section, partly following the reviews Ref. [78,85], we briefly summarize the quantum mechanical description of normal superconducting structures and the relation of the Andreev levels to the scattering matrix of the normal quantum dot. Regarding other important properties related to transport or the Josephson effect we refer the reader to the reviews [11, 85].

1.4.1 Andreev levels and scattering matrix

The quantum mechanical description of normal-superconducting systems is based on the Bogoliubov-de Gennes equation [86], a Schrödinger equation for the electron and hole wavefunctions $u(\mathbf{r})$ and $v(\mathbf{r})$,

$$\mathcal{H}_{\mathrm{BdG}} \begin{pmatrix} u \\ v \end{pmatrix} = E \begin{pmatrix} u \\ v \end{pmatrix}, \tag{1.53}$$

$$\mathcal{H}_{\mathrm{BdG}} = \begin{pmatrix} H - E_{\mathrm{F}} & \Delta(\mathbf{r}) \\ \Delta^*(\mathbf{r}) & E_{\mathrm{F}} - \mathcal{T}H\mathcal{T}^{-1} \end{pmatrix}. \tag{1.54}$$

Here H is the single particle Hamiltonian (cf. Eq. (1.7)). We assume non-interacting electrons in the normal region. The electrons and the holes are coupled by the superconducting pair-potential. The operator $\mathcal{T}$ stands for time-reversal, in position representation it is $\mathcal{T} = i\sigma_2\mathcal{K}$ where $\mathcal{K}$ is the operator of complex conjugation. If (u, v) is an eigenfunction with eigenvalue E, then $(-\mathcal{T}v, \mathcal{T}u)$ is also an eigenfunction, with eigenvalue $-E$. The complete set of eigenvalues thus lies symmetrically around zero. The quasiparticle excitation spectrum consists of all positive E.

In a uniform system with $\Delta(\mathbf{r}) \equiv \Delta$, $\mathbf{A}(\mathbf{r}) \equiv 0$, $U(\mathbf{r}) \equiv 0$, the excitation spectrum is continuous, with excitation gap Δ. The eigenfunctions (u, v) are plane waves characterized by a wavevector $\mathbf{k}$. The coefficients of the plane waves are the two coherence factors of the BCS (Bardeen-Cooper-Schrieffer) theory.

At an interface between a normal metal and a superconductor the pairing interaction drops to zero over atomic distances at the normal side. Therefore, $\Delta(\mathbf{r}) \equiv 0$ in the normal region. At the superconducting side of the NS interface, $\Delta(\mathbf{r})$ recovers its bulk value Δ only at some distance from the interface. This suppression of $\Delta(\mathbf{r})$ is neglected in the step-function model

$$\Delta(\mathbf{r}) = \begin{cases} \Delta e^{i\phi_\alpha} & \text{if } \mathbf{r} \in S_\alpha, \\ 0 & \text{if } \mathbf{r} \in N, \end{cases} \tag{1.55}$$

where α labels the superconducting interfaces. The step-function pair potential is also referred to in the literature as a "rigid boundary condition" [87]. It greatly simplifies the analysis of the problem without changing the results in any qualitative way.

An Andreev quantum dot consists of a quantum dot brought in contact with superconductor(s) via quantum point contact(s) (See Fig. 1.5). The step-function approximation of the position dependence of the pair potential enables to express the excitation energies in terms of the scattering matrix of the open normal dot. The strategy is to express the solution of the Bogoliubov-de Gennes equation in the normal part with the help of the scattering matrix using the basis (1.8), and to match the wavefunction to the solution in the superconductor.

In the normal region, since $\Delta(\mathbf{r})$ is zero in the Bogoliubov-de Gennes Hamiltonian, the

electrons and holes are not coupled. This translates to the scattering matrix

$$S_N(E) = \begin{pmatrix} S_{\rm e}(E) & 0 \\ 0 & S_{\rm h}(E) \end{pmatrix}, \quad S_{\rm h}(E) = \mathcal{T} S_{\rm e}(-E) \mathcal{T}^{-1} \tag{1.56}$$

relating the vector of coefficients of ingoing waves $c^{\rm in} = (c_e^{\rm in}, c_h^{\rm in})$ to the vector of coefficients of outgoing waves $c^{\rm out} = (c_e^{\rm out}, c_h^{\rm out})$. Note that ingoing or outgoing refers to the direction of the current, therefore, an ingoing hole has longitudinal wave vector pointing in the opposite direction of the wave vector of an ingoing electron. The matrix $S_{\rm e}(E)$ is the scattering matrix associated with the single electron Hamiltonian H. It is an $2N(E) \times 2N(E)$ matrix (the factors of two are due to spin), with $N(E)$ the total number of propagating modes at energy E. The dimension of $S_{\rm N}(E)$ is $2N(E) + 2N(-E)$.

In the superconductor, for energies $E < \Delta$, there are only decaying solutions, due to the absence of propagating modes at such energies. Therefore, for $E < \Delta$ the system supports bound states. Restricting ourselves to that energy range, we can define a scattering matrix $r_{\rm A}^{\alpha}$ for Andreev reflection at the NS interface (labeled by α) by $c_\alpha^{\rm in} = r_{\rm A}^{\alpha} c_\alpha^{\rm out}$. The elements of $r_{\rm A}^{\alpha}$ are obtained by matching the wavefunction in an ideal lead in the normal region to the decaying wavefunction in the superconductor (which is represented by the H of an ideal lead in $\mathcal{H}_{\rm BdG}$ with $\Delta(\mathbf{r}) = \Delta e^{i\phi_\alpha}$) at the NS interface. Since $\Delta \ll E_F$ one may ignore normal reflections at the NS interface and neglect the difference between $N_\alpha(E)$ and $N_\alpha(-E)$. This is known as the Andreev approximation [79]. The result is

$$r_{\rm A}^{\alpha}(E) = \gamma(E) \begin{pmatrix} 0 & e^{i\phi_\alpha} \\ e^{-i\phi_\alpha} & 0 \end{pmatrix}, \tag{1.57a}$$

$$\gamma(E) = e^{-i \arccos(E/\Delta)} = \frac{E}{\Delta} - i\sqrt{1 - \frac{E^2}{\Delta^2}}. \tag{1.57b}$$

Andreev reflection transforms an electron mode into a hole mode, without changing the mode index. The transformation is accompanied by a phase shift $-\arccos(E/\Delta) \mp \phi_\alpha$. (The minus sign is for reflection from electron to hole, the plus sign is for the reverse process.)

Introducing the Andreev scattering matrix S_A for two superconducting contacts with phases $\phi_\alpha = (-1)^\alpha \phi/2$, $\alpha = 1, 2$,

$$S_{\rm A} = \gamma(E) \begin{pmatrix} \emptyset & r_{\rm A} \\ r_{\rm A}^* & \emptyset \end{pmatrix}, \quad r_{\rm A} \equiv \begin{pmatrix} {\rm e}^{{\rm i}\phi/2} \mathbb{I}_{N_1} & \emptyset \\ \emptyset & {\rm e}^{-{\rm i}\phi/2} \mathbb{I}_{N_2} \end{pmatrix}, \tag{1.58}$$

the condition for matching the solution in the normal part to the solution in superconducting part can be written as[13] $c_{\rm in} = S_{\rm A} S_{\rm N} c_{\rm in}$ which implies

$$\mathrm{Det}\,(1 - S_{\rm A} S_{\rm N}) = 0. \tag{1.59}$$

The case of systems with one NS interface can be obtained from the two contact case by taking $\phi = 0$ (the phase is relevant only as a phase difference between different interfaces) and attributing the matrix elements to pairs of modes of this single lead. Using the identity

$$\mathrm{Det}\begin{pmatrix} a & b \\ c & d \end{pmatrix} = \mathrm{Det}\,(ad - aca^{-1}b) \tag{1.60}$$

(which holds for arbitrary square matrices a, b, c, d of equal dimension, with $\mathrm{Det}\, a \neq 0$), Eq. (1.59) can be rewritten as [80]

$$\mathrm{Det}\,\left[1 - \gamma(E)^2 r_{\rm A}^* S_{\rm e}(E) r_{\rm A} S_{\rm h}(E)\right] = 0, \tag{1.61}$$

The roots E_p of this determinantal equation constitute the spectrum of Andreev levels.

1.5 Outline of the thesis

The rest of the thesis is organized by publications. It can be divided to two parts. The first part consists of Chapter 2 and Chapter 3. These chapters focus on studying the behavior of the ensemble average of transport properties in chaotic quantum dots. In Sec. 1.2.3 we saw that quantum interference alters the average return probability in a way that depends on the symmetries present. This results in a symmetry dependent quantum correction to the classical average conductance, known as weak localization correction [4,19–21]. Conductance is the simplest linear statistic (Sec. 1.2.2). The goal of the first two chapters is to determine how interference corrections to averages of other linear statistics depend on the strength of spin-orbit coupling and magnetic fields. Before, this parametric dependence was known only for the conductance [31,77]. For other linear statistics results were available [88] for the limiting cases of Dyson's symmetry classes. The importance of weak localization corrections[14]

[13] This equation is valid if the evanescent modes in the leads can be neglected. It is possible to fabricate quantum point contacts for which this condition is approximately fulfilled [4].

[14] Interference corrections to transport properties other than the conductance are also called weak localization corrections.

is that ensemble averages of transport properties depend on spin-orbit coupling and magnetic fields through these corrections. The classical contributions (that one would get in the absence of phase coherence) do not depend on these symmetry breaking parameters. We work in the regime $N \gg 1$, with N being the number of modes in the pair of quantum point contacts connecting the dot to the electron reservoirs. In this limit, the classical contribution is the $O(N)$ term, the weak localization correction is the $O(1)$ term [cf. Eq.(1.33)].

In Chapter 2 we calculate $\delta\rho$, the weak localization correction to the density of transmission eigenvalues, for the crossovers between Dyson's three symmetry classes, in the case that each of the two quantum point contacts supports $N/2$ propagating modes. The knowledge of $\delta\rho$ allows one to obtain the weak localization correction to any linear statistic by an integration. This chapter is published in Ref. [89].

In Chapter 3 we concentrate on crossover behavior of the shot noise. We release the assumption of mode number symmetry. We perform our calculation in such a way that does not rely on the specific parameterization of the crossover Hamiltonian. Therefore, the result of this chapter is valid also for the transitions between the novel symmetry classes predicted by Aleiner and Falko (Sec. 1.3.4). The chapter is published in Ref. [90].

Chapters 4 and 5 form the second part of the thesis. These chapters deal with the effect of spin-orbit coupling on the excitation spectrum of chaotic Andreev quantum dots.

In Chapter 4 we introduce the spin Andreev map. This is the generalization of the quantum Andreev map, a dynamical model for quantum chaos in Andreev billiards [49], valid in the regime $\Delta\tau_{\rm dw}/\hbar \gg 1$. The spin Andreev map provides us with the possibility to verify the predictions of RMT [82,91,92] about the effects of spin-orbit coupling on the statistics of Andreev levels. In our simulations we demonstrate three effects: In zero magnetic field: (i) the narrowing of the distribution of the excitation gap; (ii) the appearance of oscillations in the average density of states. In strong magnetic field: (iii) the appearance of a peak in the average density of states at zero energy. (The magnetic field is assumed to be perpendicular to the plane of the dot.) In this chapter it is assumed that the quantum dot is coupled to one superconductor through a quantum point contact that supports $N \gg 1$ modes. The results of the chapter are published in Ref. [93].

In Chapter 5 we consider the opposite limit, we assume $\Delta\tau_{\rm dw}/\hbar \ll 1$. We study the effect of spin-orbit coupling on the Andreev levels of a Josephson junction, i.e. a quantum dot coupled to two superconductors through a pair of quantum point contacts. We focus on the level splitting arising from the combined effect of spin-orbit coupling and time-reversal

symmetry breaking by the phase difference between the superconductors. Using the scattering matrix approach we establish a simple relation between the quantum mechanical time delay matrix $-iS(dS/dE)$ and the effective Hamiltonian for the level splitting [94]. As an application we calculate the distribution of level splittings for an ensemble of single-channel chaotic Josephson junctions. The chapter is published in Ref. [95].

Chapter 2

Weak localization correction to the density of transmission eigenvalues *

2.1 Introduction

Transport in a two dimensional electron gas is affected by the spin-orbit coupling. The most common signature is the weak (anti)localization (Sec. 1.2.3). It is a small correction to the conductance due to the interference of time reversed trajectories. The sign of the correction depends on the presence or absence of the spin-orbit scattering. The correction is suppressed if a time reversal symmetry breaking magnetic field is present [4,19–21]. The spin-orbit term in the Hamiltonian has a form of a non-abelian vector potential [96]. In the case of quantum dots, if the spin-orbit coupling strength is position independent, a gauge transformation can be done, which results in an effective Hamiltonian with reduced spin-orbit coupling, and a rich variety of symmetry classes [31]. If the spin-orbit coupling depends on the position the transformation can not be done any more [77, 97]. As a consequence, the accessible symmetry classes are the three standard classes of Dyson, classifying the systems according to the presence or absence of time reversal and spin rotation symmetry.

For quantum dots with chaotic dynamics random matrix theory gives a convenient way to describe the transport properties, provided that the electron transit time $\tau_{\rm fl}$ is much shorter than the other time scales of the problem (mean dwell time $\tau_{\rm dw}$, spin-orbit time $\tau_{\rm so}$,

*This chapter is published in Phys. Rev. B **74**, 235314 (2006)

magnetic time τ_B, inverse level spacing) [11]. Constructing the appropriate RMT models for the crossover between the symmetry classes, the magnetic field and spin-orbit coupling dependence of the average conductance was calculated in Refs. [31, 77, 97]. The theoretical results are confirmed by numerical simulations [51] and they are in good agreement with the experiments [5, 7].

If one would like to calculate the averages of other transport properties, such as the shot noise power, higher order cumulants of the distribution of the transmitted charge, or any other linear statistics, the density of transmission eigenvalues is needed [11]. Jalabert et al. [88] gave the weak localization correction to the transmission eigenvalue density for chaotic quantum dots belonging to Dyson's three symmetry classes. Our work extends this result to the crossover regime between these classes. We present a calculation of the dependence of the weak localization correction to the transmission eigenvalue density on spin-orbit coupling and perpendicular magnetic field. For the sake of simplicity we restrict our attention to symmetric dots, i.e. we assume that the two leads attached to the cavity support the same number of channels [1] N, and for technical reasons we consider the case of $N \gg 1$.

In some other sense we complement the work done by Nazarov [98], who calculated the crossover behaviour of the weak localization correction to the transmission eigenvalue density for disordered samples in dimensions $d = 1, 2, 3$. Here we give the results for $d = 0$ corresponding to a quantum dot.

The study of the transmission eigenvalue density is interesting not only because of the practical implications related to the linear statistics, but it is instructive by itself as well, since it gives a deeper insight to the weak (anti)localization phenomenon. In the cases of Dyson's symmetry classes the weak localization correction to the transmission eigenvalue density is of the form of Dirac delta peaks at the endpoints of the spectrum [88]. Our analytical, closed-form result shows that these peaks broaden in the crossover regime, but the correction still remains singular. Furthermore, similarly to higher dimensional cases of Ref. [98], it is possible to identify the peaks as originating from the singlet and triplet sectors of the Cooperon modes of conventional diagrammatic perturbation theory. Our result also enables us to study the transition from weak localization to weak antilocalization on the level of transmission eigenvalues.

[1] Note that in this chapter we depart from the notation used in Chapter 1, there N referred to the total number of modes.

As applications, we calculate the weak localization correction to the conductance, the shot noise power and the third cumulant of the distribution of the transmitted charge. In the case of the conductance we recover the result of Ref. [97], giving a verification of our calculations. For the shot noise we find that for the symmetric cavities studied in this chapter the weak localization correction is absent in the full crossover regime. The third cumulant of the transmitted charge behaves the opposite way. It is "crossover induced" in the sense that the classical contribution vanishes [99, 100] and the weak localization term is nonzero only in the crossover regime.

The chapter is organized as follows. In the next section we specify the systems under consideration and the model applied for the RMT description. We briefly summarize the formal definition and the practical importance of the density of transmission eigenvalues. In Sec. 2.3 we present our main result, the weak localization correction to the transmission eigenvalue density, and analyze its behaviour as a function of the degree of time reversal and spin rotation symmetry breaking. In Sec. 2.4 we apply our result to the transport properties above. Finally we conclude in Sec. 2.5.

2.2 Description of the systems and the RMT model

Let us consider a chaotic quantum dot with two leads attached to it. We assume, that the number of propagating modes is the same for both leads. We choose the spin-orbit coupling to depend on the position to avoid the reduction of the coupling strength. The magnetic field is perpendicular to the plane of the dot. The assumptions for the spin-orbit coupling and the magnetic field ensure that our system exhibits a crossover between Dyson's standard symmetry classes.

The transmission eigenvalues are the eigenvalues of the matrix product $t't'^{\dagger}$. Denoting the number of modes in a lead with N, the transmission matrix t', describing the transmission from lead 2 to lead 1, is an $N \times N$ matrix that has elements with a further structure in spin space. It is a submatrix of S, the $2N \times 2N$ scattering matrix of the system:

$$t' = W_1 S W_2, \tag{2.1}$$

where W_1 is an $N \times 2N$ matrix defined by $(W_1)_{ij} = 1$ if $i = j$ and 0 otherwise, W_2 is a $2N \times N$ matrix with $(W_2)_{ij} = 1$ if $i = j + N$ and 0 otherwise. The product $t't'^{\dagger}$ has $2N$

eigenvalues, where the factor two comes from the spin structure of the matrix elements. If the system is time reversal invariant, there are N twofold degenerate levels.

We assume that the system can be described with random matrix theory, i.e. $\tau_{\rm fl} \ll \tau_{\rm dw}$, $\tau_{\rm B}$, $\tau_{\rm so}$, where the magnetic time is related to the flux Φ through the system as [31,32]

$$\frac{1}{\tau_{\rm B}} = \frac{\kappa}{\tau_{\rm fl}} \left(\frac{\Phi}{\Phi_0} \right)^2 ,$$

where Φ_0 is the flux quantum and κ is a numerical factor of order unity.

To give a statistical description of the crossover behaviour of the transmission eigenvalues we need an RMT model for the scattering matrix in the crossover regime. A convenient choice is the model introduced in Ref. [41], which was adapted for the systems under consideration in Ref. [97]. The S matrix is represented as

$$S = PU(1 - RU)^{-1} P^\dagger, \tag{2.2}$$

with

$$R = Q^\dagger r Q.$$

In the above expression U is an $M \times M$ random unitary symmetric matrix taken from Dyson's circular orthogonal ensemble [11] (COE) and r is a unitary matrix of size $M - 2N$. The $2N \times M$ matrix P and the $(M-2N) \times M$ matrix Q are projection matrices with $P_{ij} = \delta_{i,j}$ and $Q_{ij} = \delta_{i+2N,j}$. In spin space, the elements of the matrices U, P, and Q are all proportional to the 2×2 unit matrix $\mathbb{I}_2$. The matrix r is given by

$$r = \mathrm{e}^{-\frac{i}{M} H'}, \tag{2.3}$$

where H' is an $(M-2N)$ dimensional matrix with elements having a further matrix structure in spin space. It generates the perturbations to the dot Hamiltonian,

$$H' \;=\; ixX\mathbb{I}_2 + ia_{\rm so}(A_1\sigma_x + A_2\sigma_y). \tag{2.4}$$

Here A_j $(j = 1, 2)$ and X are real antisymmetric matrices of dimension $M - 2N$, with $\mathrm{Tr}\,\langle A_i A_j^{\rm T} \rangle = M^2 \delta_{ij}$ and $\mathrm{Tr}\,\langle X X^{\rm T} \rangle = M^2$ and σ_i are the Pauli matrices. The first term in (2.4) describes the time reversal symmetry breaking through the magnetic field. The second term, having a symplectic symmetry, corresponds to the Rashba and/or Dresselhaus terms

in the case of position dependent spin-orbit coupling [101]. The dimensionless parameters x and $a_{\rm so}$ are related to the corresponding time scales as

$$x^2 = \frac{2\pi\hbar}{\tau_{\rm B}\Delta}, \quad a_{\rm so}^2 = \frac{2\pi\hbar}{\tau_{\rm so}\Delta},$$

where Δ is the mean level spacing of the dot. At the end of the calculation the limit $M \to \infty$ should be taken.

The density of transmission eigenvalues is defined as

$$\rho(T) = \left\langle \sum_i \delta(T - T_i) \right\rangle = -\frac{1}{\pi} \lim_{\epsilon \to 0^+} \mathrm{Im} \left\langle \mathrm{Tr} \frac{1}{\mathrm{T} - \mathrm{t}'\mathrm{t}'^{\dagger} + \mathrm{i}\epsilon} \right\rangle, \tag{2.5}$$

where the trace is taken over channel and spin indices. Having $\rho(T)$ at hand we can calculate the ensemble average of any linear statistics [11]

$$A = \sum_{i=1}^{2N} a(T_i),$$

as

$$\langle A \rangle = \int \rho(T) a(T) dT.$$

Prominent examples for linear statistics are the conductance, the shot noise power, or the cumulants of the distribution of transmitted charge [11, 102, 103]. The weak localization correction for the linear statistics can be obtained from the weak localization correction to the transmission eigenvalue density.

2.3 Result and discussion

To find the density of transmission eigenvalues, one has to substitute the scattering matrix (2.2) into the definition (2.5) using (2.1), expand the inverses and calculate the average with the help of the diagrammatic technique of Ref. [104] up to subleading order in the small parameter $1/N$. The details of the calculation can be found in the Appendix. The result is

$$\rho(T) = \rho_0(T) + \delta\rho(T).$$

With the $O(N)$ contribution

$$\rho_0(T) = \begin{cases} \frac{2N}{\pi\sqrt{T(1-T)}} & \text{if } 0 < T < 1 \\ 0 & \text{otherwise} \end{cases}, \tag{2.6}$$

we recover the known result of Refs. [11, 40, 88, 105]. The factor of two accounts for the spin, as a consequence of the known fact, that the $O(N)$ term is insensitive to the spin-orbit interaction and the magnetic field.

The main result of the chapter is the closed-form, analytical expression for the weak localization correction to the density of transmission eigenvalues,

$$\delta\rho(T) = \frac{1}{\pi\sqrt{T(1-T)}} \sum_{n=0,1} (-1)^n \left(\frac{\Gamma_1(y_n)}{2} + \frac{\Gamma_2(y_n) - \Gamma_3(y_n)}{4} \right) \tag{2.7}$$

for $0 < T < 1$ and 0 otherwise. The variables y_n are $y_0 = T$ and $y_1 = 1 - T$. The expression for Γ_m is

$$\Gamma_m(y) = \frac{\gamma_m(\gamma_m + 2N)}{\gamma_m^2 + 4N(\gamma_m + N)y},$$

with

$$\gamma_1 = a_{\mathrm{so}}^2 + x^2, \quad \gamma_2 = 2a_{\mathrm{so}}^2 + x^2, \quad \gamma_3 = x^2.$$

Note that $\delta\rho(T)$ is antisymmetric with respect to the point $T = 1/2$.

As a verification of (2.7), we consider the limits of Dyson's symmetry classes. Labeling them in the usual way with the index β, they correspond to $x^2, a_{\mathrm{so}}^2 \ll N$ for $\beta = 1$ i.e. systems with time reversal and spin rotation symmetry, $x^2 \gg N$ for $\beta = 2$, that is, systems where the time reversal symmetry is broken by the magnetic field and $x^2 \ll N \ll a_{\mathrm{so}}^2$ for $\beta = 4$, for time reversal invariant systems without spin rotation symmetry. In these limits expression (2.7) recovers the known result

$$\delta\rho(T) = 2\frac{2-\beta}{4\beta} \left[\delta(T - 0^+) - \delta(T - 1 + 0^+) \right] \tag{2.8}$$

of Refs. [11, 88]. The factor of two in (2.8) is due to the twofold degeneracy of transmission eigenvalues for $\beta = 1, 4$, mentioned in Sec 2.2.

To get some insight how the weak (anti)localization peaks in (2.8) emerge, let us have a closer look at $\delta\rho(T)$ as it approaches the different limits. For $\gamma_m \ll N$ the expression for

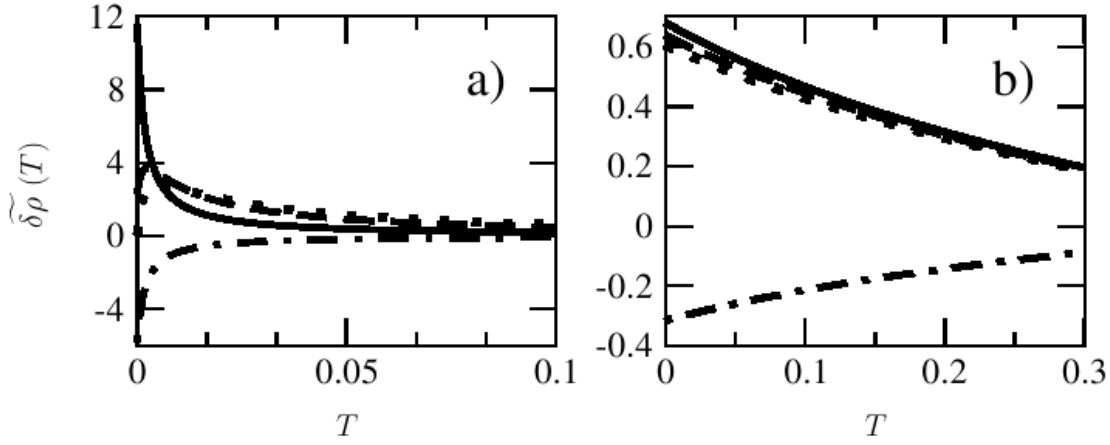

Figure 2.1: The weak localization – weak antilocalization transition for two values of the magnetic field, $x/\sqrt{N} = 0.3$ (a) and $x/\sqrt{N} = 1.3$ (b). We removed the parameter independent singularities at the endpoints, $\widetilde{\delta\rho}\,(T) = \sqrt{T(1-T)}\delta\rho(T)$. The spin-orbit coupling strength is characterized by $a_{\rm so}/\sqrt{N} = 0.0\,, 0.3\,, 0.4\,, 10$ for solid, dashed, dotted and dot-dashed lines respectively.

$\Gamma_m(y)$ is well approximated by a Lorentzian in the variable $\sqrt{y}$,

$$\Gamma_m(y) \approx \frac{\gamma_m/2N}{(\gamma_m/2N)^2 + (\sqrt{y})^2}.$$

In the opposite limit, $\gamma_m \gg N$, the functions Γ_m become independent of y. Thus going to $\beta = 1$, Γ_2 and Γ_3 cancel, and Γ_1, together with the inverse square root prefactor evolves to the peaks in (2.8) at the edge of the spectrum. Close to $\beta = 2$ the correction vanishes. Notice, that Γ_3 is independent of the spin-orbit coupling parameters. Specially in zero magnetic field it always gives Dirac delta contributions at $T = 0$ and at $T = 1$. Approaching $\beta = 4$, the contributions from Γ_1, Γ_2 disappear, thus the zero magnetic field peaks associated with Γ_3 show up as the weak antilocalization correction.

In the crossover regime the weak localization peaks in (2.8) broaden, but the correction remains singular at the endpoints. If all the γ_m-s are finite, the singularity is present through a inverse square root factor proportional to the $O(N)$ contribution. The second, nonsingular factor in (2.7) determines the form of the weak localization correction as the function of the magnetic field and spin-orbit coupling. In the absence of the magnetic field ($\gamma_3 = 0$) this

picture is modified by the inclusion of the remanent Dirac delta contribution in place of the Γ_3 term. On Fig. 2.1 we illustrated the transition from weak localization to weak antilocalization for two values of the magnetic field. The relevant regions are close to the endpoints, where the peaks of the pure symmetry cases (2.8) are located. Due to the antisymmetry of $\delta\rho(T)$ we plotted only the part around $T = 0$.

The presence of spin-orbit coupling dependent and spin-orbit coupling independent contributions is analogous to the case of higher dimensional systems studied by Nazarov [98], where they correspond to contributions coming from spin-triplet and spin-singlet Cooperon modes. The situation is very similar in our case. The basic building block of the diagrammatic expansion for $\delta\rho(T)$ is the combination $\mathcal{T}C\mathcal{T}$, with $\mathcal{T} = \mathbb{I}_2 \otimes \sigma_2$ and

$$C^{-1} = M\mathbb{I}_2 \otimes \mathbb{I}_2 - \operatorname{Tr} R \otimes \overline{R},$$

where $\overline{R} \equiv \sigma_2 R^* \sigma_2$ (the asterisk denotes complex conjugate). The tensor product is defined with a backwards multiplication:

$$(\sigma_i \otimes \sigma_j)(\sigma_{i'} \otimes \sigma_{j'}) = (\sigma_i \sigma_{i'}) \otimes (\sigma_{j'} \sigma_j). \tag{2.9}$$

The trace in the second term is understood as

$$\left(\operatorname{Tr} R \otimes \overline{R}\right)_{\alpha\beta,\gamma\delta} = R_{ij,\alpha\beta}\overline{R}_{ji,\gamma\delta},$$

where latin letters are channel indices, Greek letters refer to spin space and summation over repeated indices is implied. The very same structure emerges in the work of Brouwer et. al. [97], where the authors identify C as the equivalent of the Cooperon in the conventional diagrammatic perturbation theory. In the limit $M \to \infty$ it becomes:

$$C^{-1} = 2(N + x^2 + a_{\mathrm{so}}^2)(\mathbb{I}_2 \otimes \mathbb{I}_2) - a_{\mathrm{so}}^2(\sigma_x \otimes \sigma_x + \sigma_y \otimes \sigma_y). \tag{2.10}$$

If according to the multiplication rule (2.9) we define the action of a matrix on a vector as $(Av)_{\alpha\beta} = A_{\alpha\rho,\sigma\beta} v_{\rho\sigma}$, the spin-singlet and spin-triplet basis turns out to be the eigenbasis of the matrix $\mathcal{T}C\mathcal{T}$ with eigenvalues

$$\lambda_{00}^{-1} = 2(N + \gamma_3),\ \lambda_{1\pm1}^{-1} = 2(N + \gamma_1),\ \lambda_{10}^{-1} = 2(N + \gamma_2).$$

As in Ref. [98], only the triplet eigenvalues depend on the spin-orbit coupling strength. The correction (2.7) can be expressed as

$$\delta\rho(T) = \frac{1}{4\pi\sqrt{T(1-T)}} \sum_{n=0,1} (-1)^n \left(\sum_{m=-1}^{1} \Gamma(\lambda_{1m}, y_n) - \Gamma(\lambda_{00}, y_n) \right), \tag{2.11}$$

where the function Γ is

$$\Gamma(\lambda, y) = \frac{1 - 4N^2\lambda^2}{(1-2N\lambda)^2 + 8N\lambda y}.$$

The appearance of the spin-orbit coupling independent term is because of the decoupling of the singlet and triplet sectors of $\mathcal{T}C\mathcal{T}$. Going back to the discussion of the weak localization - weak antilocalization transition with (2.11) in mind, we find that the weak localization peak is due to the triplet terms with eigenvalue $\lambda_{1\pm1}$, and the weak antilocalization peak comes from the singlet contribution.

An other property of the higher dimensional cases that persists also for quantum dots is the breakdown of the perturbation theory for small magnetic fields near $T = 0, 1$. More precisely, for fields $x^2 \lesssim 1$ the applicability condition $\delta\rho \ll \rho$ of the perturbation theory is violated in an interval of order $O(x/N^2)$ from the endpoints of the spectrum. The conclusion is the same as in Ref. [98], namely, at small fluxes, for obtaining the detailed behaviour of the density near $T = 0, 1$ one has to treat the problem in a nonperturbative way.

2.4 Applications

Having obtained the $\delta\rho(T)$, let us see some applications. In the following we assume zero temperature. First we compute the conductance. We find

$$G = \frac{e^2}{h} \int_0^1 dT(\rho_0(T) + \delta\rho(T))T = \frac{e^2}{h} N \left[1 - \left(\frac{1}{2(\gamma_1 + N)} + \frac{1}{4(\gamma_2 + N)} - \frac{1}{4(\gamma_3 + N)} \right) \right], \tag{2.12}$$

where the second term represents the weak localization correction. It is another verification of (2.7), as we recover the corresponding result of Brouwer et. al. in Ref. [97]. Note that the correction is of the form $\delta G \propto \lambda_{00} - \sum_{m=-1}^{1} \lambda_{1m}$ (Ref. [20, 31]).

As a second application we consider the shot noise power. We get

$$P = \frac{2e^3V}{h}\int_0^1 dT(\rho_0(T)+\delta\rho(T))T(1-T) = \frac{2e^3V}{h}\frac{N}{4},$$

that is, the $O(1)$ contribution from $\delta\rho(T)$ is absent. In the case of pure symmetry classes it is a known result, that the weak localization correction to the shot noise power vanishes if the number of modes is the same in both leads [11, 88]. It was shown in Ref. [106] that this persists to the case of a $\beta = 1 \to 2$ transition too. Our result allows us to extend this prediction to the more general crossover interpolating between all of Dyson's symmetry classes. The reason behind the absence of the $O(1)$ contribution is that $T(1-T)$ is symmetric with respect to the point $T = 1/2$ and it is integrated with the antisymmetric density function $\delta\rho(T)$.

To see an example, where the weak localization correction is absent in the limit of pure symmetry classes, but not in the crossover regime, let us take the third cumulant of the distribution of the transmitted charge. It is the opposite of the shot noise in the sense, that for cavities with leads supporting the same number of channels the $O(N)$ term vanishes [99, 100], thus the leading order of this quantity is determined by $\delta\rho$. The third cumulant is proportional to

$$f_3 = \int_0^1 dT(\rho_0(T)+\delta\rho(T))T(1-T)(1-2T).$$

The weak localization correction trivially vanishes in the pure symmetry case because of the factor $T(1-T)$ and the Dirac delta functions in (2.8). In the crossover regime we find

$$f_3 = N\left(\frac{\gamma_1(\gamma_1+2N)}{16(\gamma_1+N)^3} + \frac{\gamma_2(\gamma_2+2N)}{32(\gamma_2+N)^3} - \frac{\gamma_3(\gamma_3+2N)}{32(\gamma_3+N)^3}\right),$$

that is, the (ensemble average of the) third cumulant is "crossover induced" for a symmetric cavity.

2.5 Conclusions

We investigated the crossover behaviour of the weak localization correction to the density of the transmission eigenvalues between Dyson's three symmetry classes $\beta = 1, 2, 4$ for a case of a chaotic cavity with symmetric leads. Using the RMT model introduced in Ref. [41],

with the help of the diagrammatic method of Brouwer and Beenakker [104], we carried out a subleading order calculation in the small parameter $1/N$. Our main finding is a closed-form, analytical expression for the correction.

We studied the weak localization - weak antilocalization transition in detail. We found that the weak (anti)localization peaks (2.8) of the case of pure symmetry classes broaden in the crossover regime, but the correction still remains singular at the endpoint of the spectrum. With our result (2.7) at hand, we gave a quantitative description of the broadening and the crossover from localization to antilocalization as the function of the magnetic field and spin-orbit coupling.

We compared our results to the known cases of higher dimensionalities, and found strong similarities. First, our result also splits into spin-singlet and spin-triplet parts, with only the triplet contribution depending on the spin-orbit coupling. In the limits of pure symmetry classes, the weak localization peak comes from the triplet contribution, while the antilocalization peak is due to the singlet part. Second, we also find that for small magnetic fields, the perturbation theory fails to describe the details of the density near the endpoints of the transmission eigenvalue spectrum.

We applied our results to the conductance, the shot noise power and the third cumulant of the distribution of the transmitted charge. The conductance served as a test for our calculations, we recovered the result of Ref. [97] obtained in the framework of the same model. For the shot noise power we found that the weak localization correction is absent in the full crossover, due to the symmetry of the transmission eigenvalue density. For the third cumulant we found opposite behaviour. It is "crossover induced", i.e. the $O(N)$ term is absent and the $O(1)$ contribution is nonzero only in the crossover regime.

Further directions of research could be to apply our result to obtain the weak localization correction to the full statistics of the transmitted charge. Another possibility would be to extend our calculations to the case of cavities with asymmetric leads. In that case, differently from the present results, we expect a nontrivial magnetic field and spin-orbit coupling dependence also for the shot noise power.

Appendix: Details of the calculation

In this appendix we give the details of the derivation of our main result (2.7). We adapt a procedure of Brouwer and Beenakker [104] that removes the nested geometric series in (2.5),

appearing due to the inverse in the expression (2.2) for the S matrix. The price for this is the introduction of more complicated matrix structures.

Let us introduce the $2M \times 2M$ matrices

$$\begin{gathered}\mathbf{S} = \begin{pmatrix} S & 0 \\ 0 & S^\dagger \end{pmatrix}, \quad \mathbf{C} = \begin{pmatrix} 0 & C_2 \\ C_1 & 0 \end{pmatrix}, \quad \mathbf{U} = \begin{pmatrix} U & 0 \\ 0 & U^\dagger \end{pmatrix}, \\ \mathbf{F}(z) = \begin{pmatrix} 0 & F'(z) \\ F(z) & 0 \end{pmatrix}, \quad \mathbf{R} = \begin{pmatrix} R & 0 \\ 0 & R^\dagger \end{pmatrix},\end{gathered} \tag{2.13}$$

where for S we use the representation (2.2) with P being $M \times M$ matrix

$$P_{ij} = 1 \text{ if } i = j \leq 2N \text{ and 0 otherwise,}$$

and the $M \times M$ matrices C_1 and C_2 are

$$\begin{aligned}(C_1)_{ij} &= 1 \text{ if } i = j \leq N \text{ and 0 otherwise} \\ C_2 &= P - C_1.\end{aligned}$$

The Green functions $F_1(z)$ and $F_2(z)$ are defined as

$$F(z) = C_1(z - SC_2S^\dagger C_1)^{-1}, \tag{2.14a}$$

$$F'(z) = C_2(z - S^\dagger C_1 S C_2)^{-1}. \tag{2.14b}$$

The density of transmission eigenvalues can be obtained from $F(z)$ as

$$\rho(T) = -\pi^{-1} \lim_{\epsilon \to 0^+} \operatorname{Im} \operatorname{Tr} \langle F(T + i\epsilon) \rangle. \tag{2.15}$$

The matrix Green function $\mathbf{F}(z)$ can be expressed as

$$\begin{aligned}\mathbf{F}(z) &= (2z)^{-1} \textstyle\sum_\pm \left(\mathbf{C} \pm \mathbf{C} \left[1 - \mathbf{U}(\mathbf{R} \pm \mathbf{C} z^{-1/2}) \right]^{-1} \mathbf{U}\mathbf{C} z^{-1/2} \right) \\ &= (2z)^{-1} \textstyle\sum_\pm \left[\mathbf{C} \pm \mathbf{A}_\pm (\mathbf{F}_\pm - \mathbf{X}_\pm) \mathbf{B}_\pm \right],\end{aligned} \tag{2.16}$$

with $\mathbf{X}_\pm = \mathbf{R} \pm \mathbf{C} z^{-1/2}$ and $\mathbf{F}_\pm = \mathbf{X}_\pm (1 - \mathbf{U}\mathbf{X}_\pm)^{-1}$. We defined $\mathbf{A}_\pm$ and $\mathbf{B}_\pm$ such that

$\mathbf{A}_\pm\mathbf{X}_\pm = \mathbf{C}$, $\mathbf{X}_\pm\mathbf{B}_\pm = \mathbf{C}z^{-1/2}$.

To get the ensemble average of $\mathbf{F}$, one has to calculate the COE average of $\mathbf{F}_\pm$. In the following $\mathbf{F}_\pm$ refers to this unitary average. It is related to the self energy $\mathbf{\Sigma}_\pm$ through the Dyson equation

$$\mathbf{F}_\pm = \mathbf{X}_\pm \left(1 + \mathbf{\Sigma}_\pm \mathbf{F}_\pm\right), \tag{2.17}$$

We can express $\langle \mathbf{F} \rangle$ directly through $\mathbf{\Sigma}_\pm$ as

$$\langle \mathbf{F} \rangle = (2z)^{-1} \sum_\pm \left(\mathbf{C} \pm \mathbf{C} \left\langle (1 - \mathbf{\Sigma}_\pm \mathbf{X}_\pm)^{-1} \mathbf{\Sigma}_\pm \right\rangle \mathbf{C} z^{-1/2} \right) \tag{2.18}$$

First we calculate $\mathbf{F}_\pm$ to leading order in $\frac{1}{N}$. To this order we have to consider the planar diagrams only. Denoting the resulting series as $\mathbf{F}_\pm^{(0)}$, for the self energy we find

$$\mathbf{\Sigma}_\pm^{(0)} = \sum_{n=1}^{\infty} W_n \left(\mathcal{P} \mathbf{F}_\pm^{(0)} \right)^{2n-1}, \tag{2.19}$$

where the coefficients W_n are given as [104]

$$W_n = \frac{1}{n} N^{1-2n} (-1)^{n-1} \binom{2n-2}{n-1}.$$

The operator $\mathcal{P}$ acts on a $2M \times 2M$ matrix $\mathbf{A}$ as

$$\mathbf{A} = \begin{pmatrix} A_{11} & A_{12} \\ A_{21} & A_{22} \end{pmatrix}, \quad \mathcal{P}\mathbf{A} = \begin{pmatrix} 0 & \operatorname{tr} A_{12} \\ \operatorname{tr} A_{21} & 0 \end{pmatrix}.$$

With the help of the generating function

$$h(z) = \sum_{n=1}^{\infty} W_n z^{n-1} = \frac{1}{2z} \left(\sqrt{M^2 + 4z} - M \right)$$

we can write equation (2.19) as

$$\mathbf{\Sigma}_\pm^{(0)} = \left(\mathcal{P} \mathbf{X}_\pm (1 - \mathbf{\Sigma}_\pm^{(0)} \mathbf{X}_\pm)^{-1} \right) h \left(\left(\mathcal{P} \mathbf{X}_\pm (1 - \mathbf{\Sigma}_\pm^{(0)} \mathbf{X}_\pm)^{-1} \right)^2 \right).$$

The solution is

$$\mathbf{\Sigma}_{\pm}^{(0)} = \pm\left(\sqrt{z} - \sqrt{z-1}\right)\begin{pmatrix} 0 & 1 \\ 1 & 0 \end{pmatrix}. \tag{2.20}$$

From (2.20) it follows that

$$\mathrm{Tr}F_0(z) = \mathrm{Tr}F_0'(z) = \frac{2N}{\sqrt{z(z-1)}},$$

from which we get the well known result (2.6) for the density of transmission eigenvalues.

In accounting for the weak localization correction let us write the self energy as

$$\mathbf{\Sigma}_{\pm} = \mathbf{\Sigma}_{\pm}^{(0)} + \delta\mathbf{\Sigma}_{\pm}. \tag{2.21}$$

It follows from (2.18), that $\mathbf{F}$ splits up too,

$$\mathbf{F} = \mathbf{F}^{(0)} + \delta\mathbf{F},$$

with $\delta\mathbf{F}$ containing the weak localization correction to the Green functions (2.14) in its off-diagonal blocks. Up to first order in $\delta\mathbf{\Sigma}_{\pm}$, after a little algebra we get

$$\delta\mathbf{F} = \frac{1}{2}\left(\frac{1}{z} - \frac{1}{z-1}\right)\sum_{\pm} \mp\sqrt{z}\ \mathbf{C}\ \delta\mathbf{\Sigma}_{\pm}\mathbf{C}. \tag{2.22}$$

The contributions to the self energy correction $\delta\mathbf{\Sigma}_{\pm}$ come from the $O(\frac{N^{\alpha}}{M^{\alpha+1}})$ terms in the large-M expansion of $\mathbf{\Sigma}_{\pm}$. These can be sorted as

$$\delta\mathbf{\Sigma}_{\pm} = \delta\mathbf{\Sigma}_{\pm}^{(e)} + \sum_{n=1}^{\infty} W_n \delta\left(\mathcal{P}\mathbf{F}_{\pm}\right)^{2n-1}. \tag{2.23}$$

The first term consists of diagrams with the outermost U-cycle being non-planar (see Fig. 2.2), and a term due to the sub-leading order in the large-M expansion of the cumulant coefficients

$$\delta\mathbf{\Sigma}_{\pm}^{(e)} = \delta\mathbf{\Sigma}_{\pm}^{(1)} + \delta\mathbf{\Sigma}_{\pm}^{(2)} + \underbrace{\sum_{n=1}^{\infty} \delta W_n \left(\mathcal{P}\mathbf{F}_{\pm}^{(0)}\right)^{2n-1}}_{\delta\mathbf{\Sigma}_{\pm}^{(\delta W)}}, \tag{2.24}$$

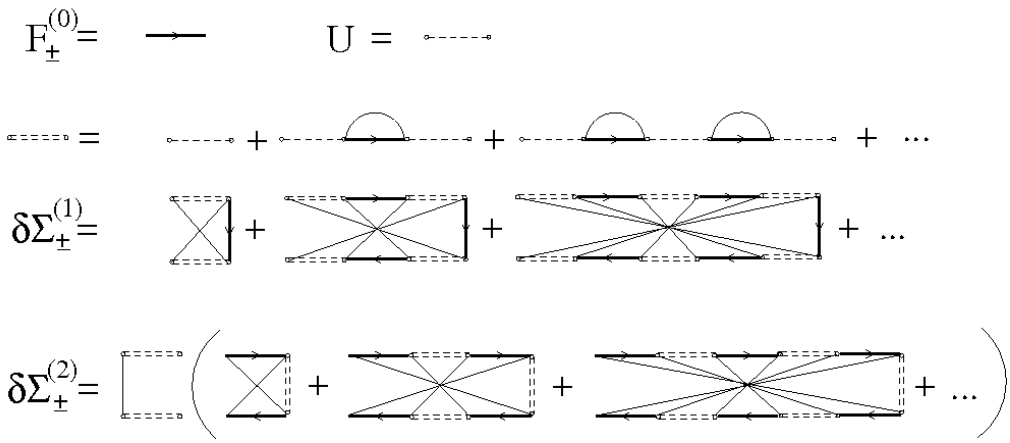

Figure 2.2: Diagrams contributing to the explicit part $\delta\mathbf{\Sigma}_{\pm}^{(e)}$ of the weak localization correction to the self energy.

with $\delta W_n = -\frac{(-4)^{n-1}}{M^{2n}}$. Evaluating the diagrams of Fig. 2.2 for $\delta\mathbf{\Sigma}_{\pm}^{(1)}$ we find

$$\delta\mathbf{\Sigma}_{\pm}^{(1)} = \begin{pmatrix} aE_{\alpha\sigma,\alpha'\sigma'}R^*_{\sigma'\sigma} & bG_{\alpha\sigma,\alpha'\sigma'}\left(R^\dagger R + 2C_2\right)_{\sigma'\sigma} \\ bG_{\alpha\sigma,\alpha'\sigma'}\left(R^\dagger R + 2C_1\right)_{\sigma'\sigma} & aE_{\alpha\sigma,\alpha'\sigma'}R^T_{\sigma'\sigma} \end{pmatrix} \tag{2.25}$$

where Greek indices refer to spin space and we assumed summation for repeated indices. Furthermore

$$\begin{aligned} a &= \frac{\sqrt{z}+\sqrt{z-1}}{2\sqrt{z-1}}, \quad b = \pm\frac{1}{2\sqrt{z-1}}, \\ E &= -2Nb^2\ \mathcal{T}\Pi\mathcal{T}, \quad G = a^2\ \mathcal{T}\ C^{-1}\Pi\ \mathcal{T}, \end{aligned} \tag{2.26}$$

with

$$\Pi = \left(a^4C^{-2} - (2Nb^2)^2\right)^{-1}.$$

The matrices $\mathcal{T}$ and C are defined as in Sec. 2.3.

The second term $\delta\mathbf{\Sigma}_{\pm}^{(2)}$ is

$$\delta\mathbf{\Sigma}_{\pm}^{(2)} = \left((s_1+s_2)Q_{11} + 2s_1Q_{12}\right)_{\alpha\sigma,\alpha'\sigma'} \begin{pmatrix} 0 & 1 \\ 1 & 0 \end{pmatrix}, \tag{2.27}$$

where

$$Q = M \begin{pmatrix} a^2G + b^2E & a^2E + b^2G \\ a^2E + b^2G & a^2G + b^2E \end{pmatrix} \begin{pmatrix} a^2\mathrm{Tr}R \otimes R^* & b^2(M-2N) \\ b^2(M-2N) & a^2\mathrm{Tr}R \otimes R^*, \end{pmatrix}$$

where the trace is defined as in Sec. 2.3 and

$$s_1 = -\frac{b}{M^2}\left(\frac{z-1}{z}\right)^{3/2} \qquad s_2 = \left(1 - 4z\frac{b^2}{a^2}\right) s_1.$$

Doing the summation in the third term in (2.24) we get

$$\delta\mathbf{\Sigma}_{\pm}^{(\delta W)} = -\frac{b}{M}\frac{z-1}{z}\begin{pmatrix} 0 & 1 \\ 1 & 0 \end{pmatrix}. \tag{2.28}$$

The second term in (2.23) contains sub-leading order diagrams, that have planar outermost U-cycles. Up to first order in $\delta\mathbf{\Sigma}_{\pm}$

$$\delta\left(\mathcal{P}\mathbf{F}_{\pm}\right)^{2n-1} = \left(\mathcal{P}\mathbf{F}_{\pm}^{(0)} + \mathcal{P}\left(\mathbf{F}_{\pm}^{(0)}\delta\mathbf{\Sigma}_{\pm}\mathbf{F}_{\pm}^{(0)}\right)\right)^{2n-1} - \left(\mathcal{P}\mathbf{F}_{\pm}^{(0)}\right)^{2n-1}.$$

Putting everything together we see, that (2.23) is a (linear) self-consistency equation for $\delta\mathbf{\Sigma}_{\pm}$, which can be solved straightforwardly, if from (2.22) we notice, that for the transmission eigenvalue density it is enough to get $\mathrm{Tr}_2\ \delta\mathbf{\Sigma}_{\pm}$, where we denoted the spin-trace as Tr_2. Substituting the solution in (2.22) in the lower left block we get the weak localization correction to $F(z)$, from which using (2.15) we arrive to the result (2.7).

Chapter 3

Effect of symmetry class transitions on the shot noise *

The time dependent fluctuations in the electrical current due to the discreteness of the electrical charge are known as shot noise [102, 107]. In the quantum regime it is influenced by the magnetic field and the spin-orbit coupling through weak (anti)localization [11, 106, 108–111], a correction of order e^2/h to the classical value of the noise power.

The motivation for studying the weak localization correction to the shot noise is the recent theoretical [31, 77, 97, 112] and experimental [5, 7, 113] interest in the transport properties of GaAs based quantum dots. Aleiner and Falko showed that in such systems the interplay between spin-orbit scattering and in-plane magnetic field results in a remarkably rich set of symmetry classes characterized by the relative strength of the system parameters [31]. Consequently, the question of symmetry class transitions is far more complicated than in the case of the usual weak localization - weak antilocalization physics. This latter, simpler crossover is also achievable, if the spin-orbit coupling strength is spatially modulated [97].

For quantum dots with chaotic dynamics random matrix theory (RMT) gives a convenient way to describe the transport properties. The RMT approach is applicable if the mean dwell time $\tau_{\rm dw}$ is much larger than both the electron transit time $\tau_{\rm fl}$, and the Ehrenfest time $\tau_{\rm E}$, up to which the electrons follow classical trajectories [11, 33–36, 114]. Assuming a two terminal device with N_1 and N_2 modes in the leads which have width W_1, W_2, the first condition requires $1 \ll L/W_j$, where L is the characteristic length of the dot. It ensures that the chaotic dynamics inside the dot has enough time to develop. The second condition, fulfilled

*This chapter is published in Phys. Rev. B **75**, 041308(R) (2007)

if $N_j \leq L/W_{1,2}$, is needed for the electron dynamics to have a quantum mechanical, thus stochastic nature [115]. It is also assumed that $\tau_{\rm fl}$ is much smaller that the typical time scales characterizing the spin-orbit scattering and the magnetic field [31, 97].

Constructing the appropriate RMT models describing the various crossovers above, the average and the variance of conductance was calculated in Refs. [31, 77, 97]. The theoretical results are confirmed by numerical simulations [51] and they are in good agreement with the experiments [5, 7].

The RMT related aspects of shot noise are also under active research [33–35, 106, 116–123]. Braun et. al. give a semiclassical prediction for the simplest type of symmetry class transition, the orthogonal-unitary crossover [106]. Physically this is the effect of a perpendicular magnetic field in the case of spinless electrons. The prediction for the average of the shot noise power P reads as

$$\frac{\langle P\rangle}{P_0} = \frac{2N_1^2N_2^2}{N^3} + \frac{2N_1N_2(N_1-N_2)^2}{N^4(1+\xi)} + O(\frac{1}{N}), \tag{3.1}$$

where $P_0 = 2e^3|V|/h$ and $N = N_1 + N_2$ is the total number of modes. The factors of two are due to the spin degeneracy. The dependence on the magnetic field $B_\perp$ enters through the parameter

$$\xi = c\frac{e^2L^4B_\perp^2}{\hbar\tau_{\rm fl}N\Delta},$$

where Δ is the mean level spacing of the dot and c is a numerical factor of order unity. Comparing this result to the case of the conductance [30, 124–126],

$$\frac{\langle G\rangle}{G_0} = \frac{2N_1N_2}{N} - \frac{2N_1N_2}{N^2(1+\xi)} + O(\frac{1}{N}), \tag{3.2}$$

where $G_0 = e^2/h$, we find the simple relation

$$\frac{\delta P}{P_0}/\frac{\delta G}{G_0} = -\left(\frac{N_1-N_2}{N_1+N_2}\right)^2 \tag{3.3}$$

between the weak localization correction to the conductance and the shot noise, denoted by δG and δP, respectively (the second terms in (3.1) and (3.2)).

The behavior of the shot noise under more general crossovers is yet unknown. In this chapter we address this question and present an RMT calculation for the average shot noise

power allowing for any symmetry class transitions induced by in-plane and perpendicular magnetic fields and spin-orbit coupling studied in Ref. [31,77,97]. For technical reasons we restrict our attention to the case of $N_1, N_2 \gg 1$ and obtain $\langle P \rangle$ up to the $O(1)$ correction in the small parameter $1/N$. Our result shows that the relation (3.3) is valid for all of these crossovers. As a particular consequence, in the special case of the orthogonal-unitary transition we find a perfect agreement with Braun et. al. [106] demonstrating the equivalence of their semiclassical approach to RMT.

In the Landauer-Büttiker formalism the shot noise power can be expressed as [17,127,128]

$$P = P_0 \mathrm{Tr}\left[tt^\dagger \left(1 - tt^\dagger\right)\right],$$

where the trace is taken over channel and spin indices. The matrix t describes the transmission from lead 1 to lead 2. It is the submatrix of S, the $N \times N$ scattering matrix of the system (S has elements with a further matrix structure in spin space) [11],

$$t = W_2 S W_1^\dagger,$$

where W_1 is an $N_1 \times N$ matrix defined by $(W_1)_{ij} = \delta_{i,j}$, W_2 is an $N_2 \times N$ matrix with $(W_2)_{ij} = \delta_{i+N_1,j}$. For an RMT model of the crossover regime we apply the description given in Ref. [41,77,97], and parameterize the S-matrix as

$$S = PU(1 - RU)^{-1} P^\dagger, \tag{3.4}$$

with

$$R = Q^\dagger r Q.$$

In the above expression U is an $M \times M$ random unitary symmetric matrix taken from Dyson's circular orthogonal ensemble [11] (COE) and r is a unitary matrix of size $M - N$. The $N \times M$ matrix P and the $(M-N) \times M$ matrix Q are projection matrices with $P_{ij} = \delta_{i,j}$ and $Q_{ij} = \delta_{i+N,j}$. The matrix r is given by

$$r = \exp\left[-\frac{2\pi i}{M\Delta} H'\right], \tag{3.5}$$

where H' is an $(M-N)$ dimensional matrix with elements having a further matrix structure in spin space. It generates the perturbations to the dot Hamiltonian due to magnetic fields

and spin-orbit coupling [77,97]. In the previous chapter we saw its form in the case that H' describes a crossover between Dyson's three symmetry classes (Eq. (2.4)). Here we do not make any explicit reference to the particular form of the symmetry breaking perturbation, thus depending on the system under consideration, the model can describe these standard weak localization - weak antilocalization crossovers or the more complicated transitions between the symmetry classes identified by Aleiner and Falko [31].

To obtain the weak localization correction to shot noise power, one has to calculate the average

$$\mathrm{Tr}\left\langle tt^\dagger\left(1-tt^\dagger\right)\right\rangle = T_2 - T_4, \tag{3.6}$$

where

$$T_2 = \mathrm{Tr}\left\langle tt^\dagger\right\rangle, \quad T_4 = \mathrm{Tr}\left\langle tt^\dagger tt^\dagger\right\rangle.$$

The calculation can be done by expanding S in powers of U using (3.4) and averaging over the COE with the help of the diagrammatic technique of Ref. [104].

In the case of T_2, the result is already known from earlier studies of the conductance, $\langle G\rangle = G_0 T_2$ [77,97].

$$T_2 = \frac{2N_1N_2}{N} - \frac{N_1N_2}{N}\left(\mathcal{T}C\mathcal{T}\right)_{\rho\sigma,\rho\sigma}, \tag{3.7}$$

where we assumed summation for repeated indices. Here, $\mathcal{T} = \mathbb{I}_2 \otimes \sigma_2$, with $\mathbb{I}_2$ the 2×2 unit matrix and σ_j the Pauli matrices acting in spin space. The matrix C is defined as

$$C = \left\langle \left(M\mathbb{I}_2 \otimes \mathbb{I}_2 - \mathrm{tr}\, R\otimes\overline{R}\right)^{-1}\right\rangle, \tag{3.8}$$

where $\overline{R} \equiv \sigma_2 R^* \sigma_2$ (the asterisk denotes complex conjugate). The remaining average should be done with respect to the distribution of H'. The tensor product is defined with a backwards multiplication:

$$(\sigma_i \otimes \sigma_j)(\sigma_{i'} \otimes \sigma_{j'}) = (\sigma_i\sigma_{i'}) \otimes (\sigma_{j'}\sigma_j). \tag{3.9}$$

The trace in the second term is understood as

$$\left(\mathrm{tr}\, R\otimes\overline{R}\right)_{\alpha\beta,\gamma\delta} = R_{ij,\alpha\beta}\overline{R}_{ji,\gamma\delta},$$

where latin letters are channel indices, Greek letters refer to spin space. In (3.7), the contribution proportional to C enters through the summation of maximally crossed diagrams. Note that all the magnetic field and spin-orbit coupling dependence of the conductance is

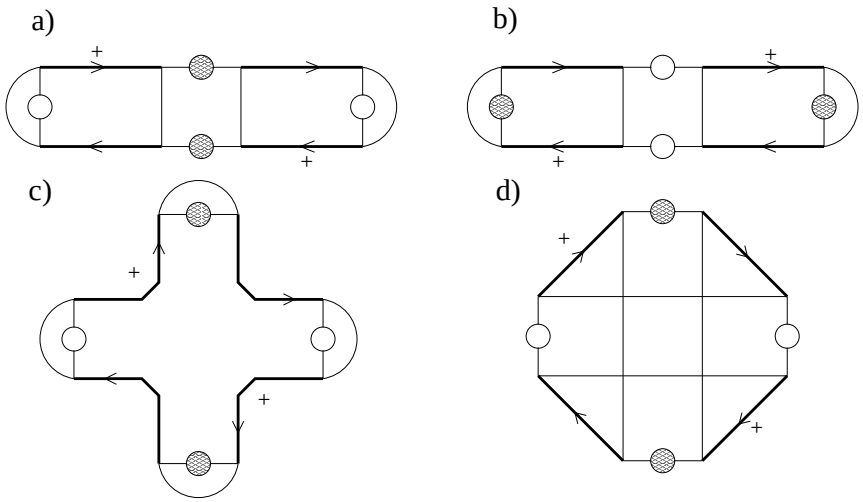

Figure 3.1: Diagrams representing the term T_4. See text for description.

encoded in this object [77, 97]. The same structure will play a key role in the case of the term T_4 too, determining its crossover behavior.

The fourfold product T_4 can be represented as the sum of four types of diagrams, which are schematically depicted on Fig. 3.1. The thick lines with and without + correspond to the series expansion of

$$U(1-RU)^{-1} \quad \text{and} \quad U^\dagger(1-R^\dagger U^\dagger)^{-1},$$

respectively. The line with empty circle represents the matrix C_1, the one with shaded circle corresponds to C_2, where $C_i = P^\dagger W_i^\dagger W_i P$. The thin lines that are either around the matrices C_i or connecting them are contractions corresponding to the diagrammatic method. The way these thin lines are drawn define the four distinct types of diagrams shown on Fig. 3.1.

In the case of the type a (Fig. 3.1a), the leading order diagrams have ladder structures on the left and right of the middle part containing the matrix C_2. These contribute in orders $O(N)$ and $O(1)$,

$$T_4^{(a,l)} = \frac{2N_1^2N_2}{(N+1)^2} = \frac{2N_1^2N_2}{N^2} - \frac{4N_1^2N_2}{N^3} + O\left(\frac{1}{N}\right).$$

An other $O(1)$ correction comes from inserting a maximally crossed part into one of the

ladders, resulting in

$$\delta T_4^{(a,mc)} = \frac{2N_1^2N_2}{N^3}\left(2 - N\left(\mathcal{T}C\mathcal{T}\right)_{\rho\sigma,\rho\sigma}\right).$$

The contribution from type b (Fig. 3.1b) can be obtained from type a by interchanging N_1 and N_2. In the case of type c (Fig. 3.1c), the leading order diagrams have ladder structures attached to the central part, which can be an U-cycle of length two or a T-cycle representing $\mathrm{tr}\left(RR^\dagger RR^\dagger\right)$ with tr denoting channel trace [129]. The corresponding contribution is

$$T_4^{(c,l)} = -\frac{2NN_1^2N_2^2}{(N+1)^4} = -\frac{2N_1^2N_2^2}{N^3} + \frac{8N_1^2N_2^2}{N^4} + O\left(\frac{1}{N}\right).$$

The higher order diagrams giving further $O(1)$ terms can be drawn again by inserting a maximally crossed part into one of the ladders or by opening the central part and putting the insertion between two neighboring ladders. Evaluating the diagrams we find

$$T_4^{(c,mc)} = -\frac{4N_1^2N_2}{N^4}\left(2 - N\left(\mathcal{T}C\mathcal{T}\right)_{\rho\sigma,\rho\sigma}\right).$$

Finally, as the contributions of type d (Fig. 3.1d) are at most of order $O(1/N^2)$, they can be disregarded in a weak localization calculation.

Collecting the contributions to T_4 and using (3.6) and (3.7), for the average shot noise power we find

$$\frac{\langle P\rangle}{P_0} = \frac{2N_1^2N_2^2}{N^3} + \frac{N_1N_2(N_1-N_2)^2}{N^3}\left(\mathcal{T}C\mathcal{T}\right)_{\rho\sigma,\rho\sigma}, \tag{3.10}$$

which is the main result of this chapter. Similarly to the case of the conductance, all the dependence on the magnetic fields and spin-orbit coupling is through the combination $\left(\mathcal{T}C\mathcal{T}\right)_{\rho\sigma,\rho\sigma}$. The concrete expressions for $\left(\mathcal{T}C\mathcal{T}\right)_{\rho\sigma,\rho\sigma}$ corresponding to the various symmetry class transitions can be found in Refs. [77,97]. In the particular case of an orthogonal-unitary crossover the semiclassical prediction (3.1) is recovered.

Together with (3.7), the formula (3.10) indeed implies that the relation (3.3) holds for all the crossovers due to magnetic fields and spin-orbit coupling studied in the context of transport in chaotic quantum dots. This means that the first quantum correction to the ensemble averaged shot noise is related to the first quantum correction to the ensemble averaged mean current $\langle\overline{I}\rangle = \langle G\rangle V$ by a simple multiplication with a factor that depends only on the channel number asymmetry of the system. It would be interesting to know if there is a similar relation for higher dimensional disordered mesoscopic conductors.

In summary, we gave an RMT prediction for the average shot noise power as a function of magnetic field and spin-orbit coupling. Our result can be applied to the various crossovers ranging from the standard weak localization - weak antilocalization transition to the interpolation between the symmetry classes identified by Aleiner and Falko [31]. We found that the remarkably simple relation (3.3) between δP and δG persists for all of these crossovers. In the special case of an orthogonal-unitary transition we recover the semiclassical prediction of Braun et al. [106].

Chapter 4

Spin-orbit coupling and the spectrum of chaotic Andreev billiards *

4.1 Introduction

A quantum dot in a two-dimensional electron gas has a mean level spacing which is independent of energy and depends only on geometrical factors (area) and material properties (effective mass). The nature of the electron dynamics (chaotic versus integrable) and the presence or absence of symmetries, such as time-reversal and spin-rotation symmetry, have no effect on the mean density of states. The situation changes if the quantum dot is coupled to a superconductor (see Fig. 4.1). The presence of the superconductor strongly affects the excitation spectrum of such an Andreev billiard. The density of states at the Fermi level is suppressed in a way which is sensitive to the nature of the dynamics and existing symmetries [78]. While the effect of broken time-reversal symmetry on the density of states has been studied extensively [81, 84, 130, 131], the effect of broken spin-rotation symmetry due to spin-orbit coupling has only been partially investigated [82, 94, 132].

In this chapter we study in computer simulations three effects of the spin-orbit coupling. All of these effects have been predicted by random-matrix theory (RMT) [82,91,92], but have so far not been confirmed in a dynamical model. The first two of these effects [91,92], present in the absence of a magnetic field, are the reduction of the sample-to-sample fluctuations of the excitation gap and the appearance of oscillations as a function of energy in the average density of states. The third effect appears in a magnetic field strong enough to close the

*This chapter is published in Phys. Rev. B **75**, 165307 (2007)

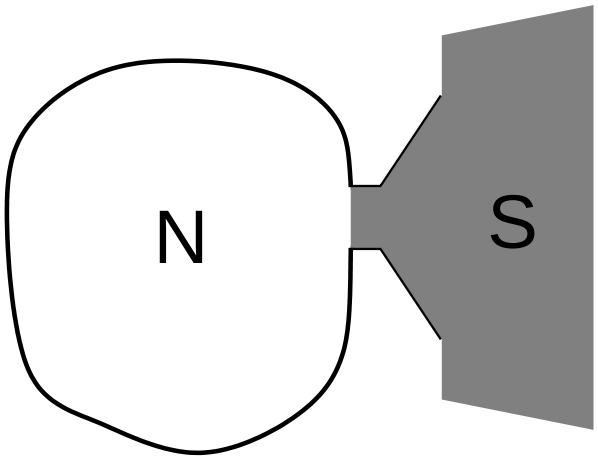

Figure 4.1: Sketch of an Andreev Billiard: A quantum dot (N) connected to a superconductor (S) by a point contact. Spin-orbit coupling is present in the quantum dot.

excitation gap[1]. While in the absence of spin-orbit coupling the average density of states vanishes at the Fermi level, in the presence of spin-orbit coupling it peaks at the Fermi level at twice the value in the normal state [82].

4.2 Predictions of random-matrix theory

We begin by briefly summarizing the RMT of the Andreev billiard [78]. In perturbation theory the density of states of non-degenerate levels (in zero or weak magnetic field) has a square root dependence on energy near the gap [83, 84],

$$\rho_{\rm pert}(E) = \frac{1}{\pi}\sqrt{\frac{E-E_{\rm gap}}{\Delta_{\rm gap}^3}}, \quad E \to E_{\rm gap}. \tag{4.1}$$

The parameters $E_{\rm gap}$ and $\Delta_{\rm gap}$ are given by

$$E_{\rm gap} = cE_T, \quad \Delta_{\rm gap} = \left(\frac{s\delta}{2}\right)^{2/3}\left(\frac{dE_T}{4\pi^2}\right)^{1/3}. \tag{4.2}$$

Here $\delta = 2\pi\hbar^2/mA$ is the mean level spacing in the isolated quantum dot (area A, effective mass m), $N = {\rm Int}[k_F W/\pi]$ is the number of modes in the ballistic point contact (width W,

[1] In this chapter, the magnetic field is assumed to be perpendicular to the plane of the dot.

Fermi wave vector k_F) connecting it to the superconductor, and $E_T = N\delta/4\pi$ is the Thouless energy (inverse dwell time). These parameters refer to two-fold degenerate levels and modes, corresponding to $s = 2$. If both spin-rotation and time-reversal symmetries are broken, the two-fold degeneracy is lifted and one should take [2] $s = 1$. The numerical coefficients c and d are magnetic field dependent. For $B = 0$ one has

$$c = 2\gamma^{5/2}, \quad d = (5 - 2\sqrt{5})\gamma^{5/2}, \tag{4.3}$$

with $\gamma = (\sqrt{5} - 1)/2$ the reciprocal of the golden ratio. For $B \neq 0$ they should be calculated from the RMT solution given in Ref. [84].

The perturbation theory has δ/E_T as a small parameter and gives the density of states with an energy resolution of order E_T, which is a macroscopic energy scale. Since spin-orbit effects typically appear as quantum corrections, no sign of spin-orbit coupling can be seen in such a calculation. In particular, the magnetic field dependence of the perturbative density of states is the same with and without spin-orbit coupling — the only difference being that in a magnetic field, in the absence of spin-rotation symmetry, there is no level degeneracy thus $\Delta_{\rm gap}$ is $2^{2/3}$ times smaller than in the spin-rotation symmetric case.

To capture the spectral properties on the mesoscopic energy scale of order $\Delta_{\rm gap}$, one needs to go beyond perturbation theory. According to the universality hypothesis of Vavilov *et al.* [92] the probability distribution of the lowest level E_1 in properly scaled units is universal and identical to the distribution of the smallest eigenvalue of random Gaussian matrices from the three symmetry classes of RMT. The appropriate scaling is in terms of the dimensionless variable $x_1 = (E_1 - E_{\rm gap})/\Delta_{\rm gap}$ and the universal distributions are given by [91, 133]

$$P_\beta(x_1) = -\frac{d}{dx_1} F_\beta(x_1), \tag{4.4}$$

[2] In this chapter, for $s = 2$, the density of states refers to the density of the degenerate doublets. The total density of states is given by $s\rho_{\rm pert}$ and $s\rho_\pm$ (See Eq. (4.7) later.)

where

$$F_1(x) = \sqrt{F_2(x)} \exp\left(-\frac{1}{2}\int_{-\infty}^{x} q(x')\,dx'\right), \tag{4.5a}$$

$$F_2(x) = \exp\left(-\int_{-\infty}^{x} (x-x')q(x')^2\,dx'\right), \tag{4.5b}$$

$$F_4\left(\frac{x}{2^{2/3}}\right) = \sqrt{F_2(x)}\mathrm{ch}\left(\frac{1}{2}\int_{-\infty}^{x} q(x')\,dx'\right). \tag{4.5c}$$

The function $q(x)$ is the solution of the differential equation

$$q''(x) = -xq(x) + 2q^3(x).$$

The boundary condition is $q(x) \to \mathrm{Ai}(-x)$ as $x \to -\infty$, with $\mathrm{Ai}(x)$ being the Airy function. The three distributions are plotted in Fig. 4.2 (top panel). The symmetry index β takes values $\beta = 1$ for time-reversal and spin-rotation invariant systems, $\beta = 4$ when time-reversal symmetry is present but spin-rotation symmetry is broken, and $\beta = 2$ for systems with broken time-reversal symmetry.

Near the gap, the average density of states in terms of the variable $x = (E - E_{\mathrm{gap}})/\Delta_{\mathrm{gap}}$ is given by [134, 135]

$$\rho_1(x) = \rho_2(x) + \tfrac{1}{2}\mathrm{Ai}(-x)\left[1 - \int_{-x}^{\infty} \mathrm{Ai}(y)dy\right], \tag{4.6a}$$

$$\rho_2(x) = x\mathrm{Ai}^2(-x) + [\mathrm{Ai}'(-x)]^2, \tag{4.6b}$$

$$2^{1/3}\rho_4\left(\frac{x}{2^{2/3}}\right) = \rho_2(x) - \frac{1}{2}\mathrm{Ai}(-x)\int_{-x}^{\infty} \mathrm{Ai}(y)dy. \tag{4.6c}$$

The distribution P_2 and the density of states ρ_2 are applicable in an intermediate magnetic field range, which exists because the flux needed to close the gap is much larger than the flux needed to break the time-reversal symmetry. For intermediate fluxes ($\Phi \gtrsim (h/e)N^{1/3}\sqrt{\tau_{\mathrm{fl}}\delta/\hbar}$ with $\tau_{\mathrm{fl}} = \sqrt{A}/v_{\mathrm{F}}$ the electron transit time and v_{F} the Fermi velocity), there will still be a gap, but its fluctuations are governed by the $\beta = 2$ symmetry class. In this case the presence or absence of spin-orbit coupling only affects the parameter Δ_{gap} (which is reduced by a factor $2^{2/3}$ in the absence of spin-orbit coupling, because the level degeneracy parameter goes from $s = 2$ to $s = 1$); the gap distribution P_2 and the density of states ρ_2 in rescaled variables do not depend on the presence or absence of spin-rotation symmetry.

If the flux is made much larger ($\Phi \gg (h/e)\sqrt{N\tau_{\rm fl}\delta/\hbar}$), such that the gap closes, spin-orbit coupling starts to play a role again. The reason is that an energy level E and its mirror level at $-E$ can repel each other, and this repulsion depends on the presence or absence of spin-orbit coupling. When there is still a gap these levels are widely separated and this repulsion is not effective [82].

According to Altland and Zirnbauer [82], the RMT of an Andreev billiard in strong magnetic field is in a new symmetry class called C (D) in the absence (presence) of spin-orbit coupling. The average density of states in these symmetry classes is

$$\rho_{\pm}(E) = \frac{4}{s\delta}\left[1 \pm \frac{\sin(8\pi E/s\delta)}{8\pi E/s\delta}\right]. \tag{4.7}$$

The minus (plus) sign should be taken for symmetry class C (D). This result expresses the fact that in the absence of spin-orbit coupling, a level and its mirror level repel each other leading to a vanishing density of states at $E = 0$. In the presence of spin-orbit coupling the repulsion disappears and levels pile up at the Fermi level, leading to a peak in the density of states at $E = 0$.

For the cases where the absence of spin rotation symmetry is important, i.e. for $\beta = 4$, and symmetry class D, we assume that the spin orbit time $\tau_{\rm so}$ is much shorter than the dwell time $\tau_{\rm dwell}$.

4.3 Spin Andreev map

To verify these predictions of RMT in a dynamical model we combine the general construction of an Andreev map [49] with the spin kicked rotator (Sec. 1.3.3) [45, 51]. The starting point of our discussion is the spin generalized Bogoliubov-De Gennes Hamiltonian [86]

$$\mathcal{H}_{\rm BdG} = \begin{pmatrix} H - E_{\rm F} & \Delta \\ \Delta^* & E_{\rm F} - \mathcal{T}H\mathcal{T}^{-1} \end{pmatrix}. \tag{4.8}$$

Here H is the single particle Hamiltonian, $E_{\rm F}$ is the Fermi energy, and Δ is the superconducting pair-potential. The operator $\mathcal{T}$ stands for time-reversal, and will be specified later.

With the Bogoliubov-De Gennes Hamiltonian as a guide we construct the spin Andreev map. First we note that if an electron in the normal metal evolves with time-evolution

operator $F(t)$, the hole evolves with the transformed time-evolution operator $\mathcal{T}F(t)\mathcal{T}^{-1}$. Second, since we are interested in low energy phenomena, only the dynamics on long time scales is important. On time scales much larger than τ_{fl}, the dynamics can be described as a mapping on a two-dimensional Poincaré surface of section. This amounts to a stroboscopic description where we are only concerned with the state of the electron when it bounces off the boundary. This effective reduction of dimensionality allows for a much faster simulation than a numerical solution of Schrödinger equation would. Since we are going to be interested in the limit of large number N of modes in the leads, this will be very important as the full 2D numerical solution is limited in practice to small N. The quantum map approach catches the generic features of a chaotic billiard, as opposed to effects that rely on the specific properties of the system such as geometry, the precise form of the spin-orbit coupling, etc.

The quantum map we use is the computationally efficient spin kicked rotator, given in terms of a Floquet matrix [3] [45, 51],

$$F_{ll'} = e^{i\varepsilon_0}(\Pi U X U^\dagger \Pi)_{ll'}, \quad l, l' = 0, 1, \ldots, M-1. \tag{4.9}$$

The integer M sets the level spacing $\delta = 2\pi/M$. The $M \times M$ matrices appearing in Eq. (4.9) have matrix elements with a structure in spin space, and are given by

$$\Pi_{ll'} = \delta_{ll'} e^{-i\pi(l+l_0)^2/M}\sigma_0, \tag{4.10a}$$

$$U_{ll'} = M^{-1/2} e^{-i2\pi ll'/M}\sigma_0, \tag{4.10b}$$

$$X_{ll'} = \delta_{ll'} e^{-i(M/4\pi)V(2\pi l/M)}, \tag{4.10c}$$

with

$$V(\theta) = K\cos(\theta+\theta_0)\,\sigma_0 + K_{\text{so}}(\sigma_1 \sin 2\theta + \sigma_3 \sin\theta), \tag{4.11}$$

where σ_i are the Pauli matrices and σ_0 is the 2×2 unit matrix. The matrix X corresponds to the spin-orbit coupled free motion inside the dot and Π gives scattering off the boundaries of the dot. This map is classically chaotic for kicking strength $K \gtrsim 7.5$. The parameter K_{so} breaks spin-rotation symmetry, θ_0 breaks time-reversal symmetry and l_0 breaks other

[3] This representation corresponds to recording the dynamics at half-integer multiples of the stroboscopic time,

$$\mathcal{F} = \mathrm{T}\exp\left[-\frac{i}{\hbar_{\text{eff}}}\int_{-1/2}^{1/2} H(t)dt\right],$$

instead of the definition (1.43).

symmetries of the map to make sure that the map has no symmetries that are not present in the physical system. The spin-orbit coupling time τ_{so} (in units of the stroboscopic period $\tau_0 \approx \tau_{\mathrm{fl}}$) is related to K_{so} through $\tau_{\mathrm{so}} = 32\pi^2/(K_{\mathrm{so}}M)^2$. The connection between the magnetic flux Φ and θ_0 is given by $\Phi/\Phi_0 = CKM\theta_0/(4\pi)$, where C is a numerical constant of order unity and $\Phi_0 = h/e$ is the flux quantum [51]. The parameter ε_0 corresponds to the Fermi energy. In the above representation of the Floquet matrix, the time-reversal operator is given by $\mathcal{T} = i\sigma_2\mathcal{K}$ where $\mathcal{K}$ is the operator of complex conjugation [51]. Therefore, the hole Floquet matrix is given by $\sigma_2 F^* \sigma_2 \equiv \bar{F}$.

The spin Andreev map is constructed from the electron and hole Floquet matrices in the same way as in the absence of spin-orbit coupling [49],

$$\mathcal{F} = \mathcal{P} \begin{pmatrix} F & 0 \\ 0 & \bar{F} \end{pmatrix}, \tag{4.12a}$$

$$\mathcal{P} = \begin{pmatrix} 1 - P^T P & -iP^T P \\ -iP^T P & 1 - P^T P \end{pmatrix}. \tag{4.12b}$$

The projection matrix P projects onto the contact with the superconductor. Its matrix elements are $P_{kl} = \delta_{kl}\sigma_0 \sum_{i=1}^{N} \delta_{l,n_i}$ where the set of indices $\{n_i\}$ corresponds to the modes coupled to the superconductor. The dynamics described by the model (4.12a) is analogous to the open kicked rotator introduced in Sec. 1.3.3 (Eq. (1.49)), but here the absorption at the leads is replaced by an electron-hole conversion with a phase shift $-i$, valid for excitation energies $E \ll \Delta$ (Sec. 1.4, Eq. (1.57)). The dwell time is $\tau_{\mathrm{dwell}} = M/N$. The corresponding Thouless energy is $E_T = N\delta/4\pi = (2\tau_{\mathrm{dwell}})^{-1}$. As shown in Ref. [84], the magnetic field scale at which the gap closes is given by $\theta_c = 4\pi\sqrt{N}/(KM^{3/2})$. From the definitions in Eq. (4.2) the scaling parameters in the spin Andreev map become

$$E_{\mathrm{gap}} = \frac{cN}{2M}, \quad \Delta_{\mathrm{gap}} = \frac{(s^2 dN)^{1/3}}{2M}. \tag{4.13}$$

The Floquet matrix has the symmetry

$$\mathcal{F} = \mathcal{C}\mathcal{T}\mathcal{F}(\mathcal{C}\mathcal{T})^{-1}, \quad \mathcal{C} = \begin{pmatrix} 0 & -1 \\ 1 & 0 \end{pmatrix}, \tag{4.14}$$

corresponding to the $\mathcal{C}\mathcal{T}$-antisymmetry of $\mathcal{H}_{\mathrm{BdG}}$, the fundamental discrete symmetry of

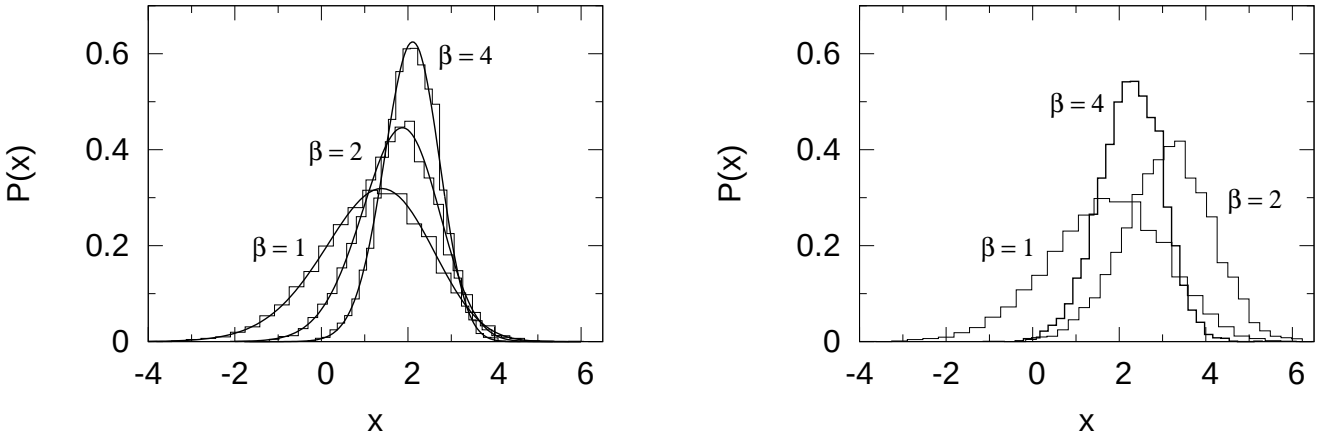

a. Fitted data b. Raw data

Figure 4.2: Probability distribution of the rescaled excitation gap $x = (E_1 - E_{\rm gap})/\Delta_{\rm gap}$. Smooth curves (left panel) are the predictions of random-matrix theory, for the three symmetry classes $\beta = 1, 2, 4$. Histograms are the results of the numerical simulation of the spin Andreev map, without spin-orbit coupling (zero magnetic field, $\beta = 1$) and with spin-orbit coupling (zero magnetic field, $\beta = 4$; weak magnetic field, $\beta = 2$). The histograms in the right panel are plotted without any fitting, while in the left panel $E_{\rm gap}$ and $\Delta_{\rm gap}$ are treated as fit parameters.

normal-superconducting systems [82]. The eigenphases of the Floquet matrix $\mathcal{F}$, defined as the solutions of

$$\det(\mathcal{F} - e^{-i\varepsilon}) = 0, \tag{4.15}$$

play the role of the discrete excitation energies in the Andreev billiard. From the symmetry (4.14) it follows that they come in pairs, $\pm\varepsilon$, as required.

4.4 Numerical results and comparison with RMT

In Fig. 4.2 we plot the excitation gap distribution (histograms) from our numerical simulation with parameters $K = 41.123$, $M = 4096$, $N = 205$. The smallest ε solving Eq. (4.15) was calculated for some 6000 different Fermi energies and positions of the contact to the superconductor. To generate the three symmetry classes we took: $\theta_0/\theta_c = 0$, $\tau_{\rm dwell}/\tau_{\rm so} = 0$ ($\beta = 1$); $\theta_0/\theta_c = 0$, $\tau_{\rm dwell}/\tau_{\rm so} = 625$ ($\beta = 4$); $\theta_0/\theta_c = 0.4$, $\tau_{\rm dwell}/\tau_{\rm so} = 625$ ($\beta = 2$). The values of the parameters c and d for $\theta_0/\theta_c = 0$ are given by Eq. (4.3). For $\theta_0/\theta_c = 0.4$ we calculate $c = 0.427$, $d = 0.339$ from Ref. [84]. The data is shown without any fit parameter in the right

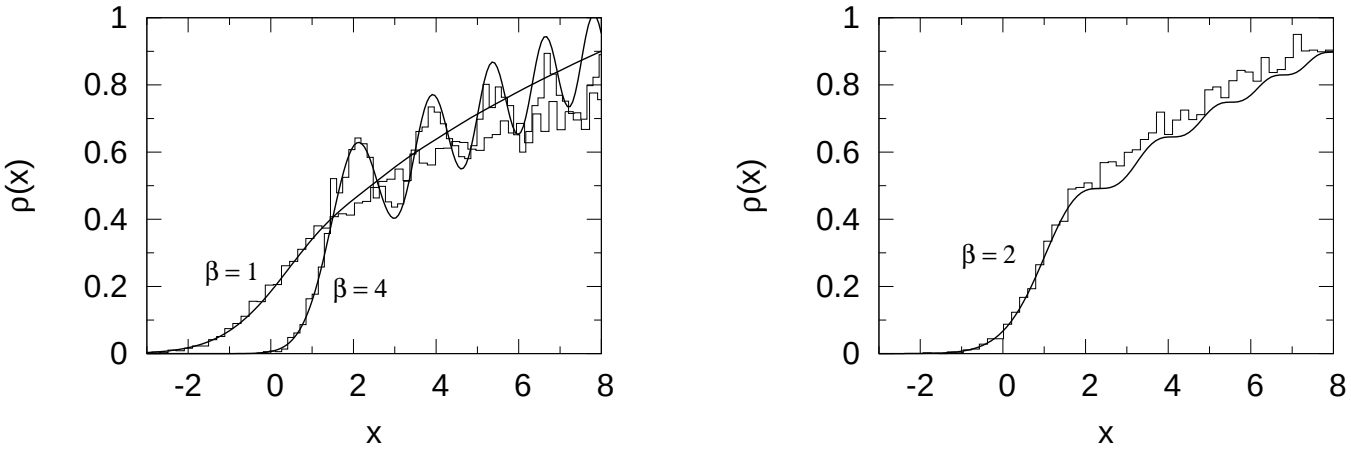

a. Scaled DOS $\beta = 4$.

b. Scaled DOS $\beta = 2$.

Figure 4.3: Average density of states in rescaled energy units, $x = (E - E_{\rm gap})/\Delta_{\rm gap}$, in zero magnetic field (left panel, $\beta = 1, 4$) and in a weak magnetic field (right panel, $\beta = 2$). The smooth curves are the RMT predictions, the histograms are the results of the simulation (using the same values of the fit parameters $E_{\rm gap}, \Delta_{\rm gap}$ as in the left panel of Fig. 4.2).

panel and with $E_{\rm gap}$, $\Delta_{\rm gap}$ as fit parameters in the left panel. (A similar fitting procedure was used in Ref. [136].) The fitted values of $E_{\rm gap}$ and $\Delta_{\rm gap}$ do not vary much (by about 5% and 10%, respectively) from their nominal values [given by Eq. (4.13)], but the agreement with the RMT predictions improves considerably if we allow for this variation [137].

The characteristics of the gap distribution are clearly obtained in our simulation. In zero magnetic field, the gap distribution becomes narrower as the strength of spin-orbit coupling is increased ($\beta = 1 \to 4$). The RMT prediction for the standard deviation of the scaled distributions $P_\beta(x)$ is $\sigma_1 = 1.27$ and $\sigma_4 = 0.64$. The corresponding values obtained in our numerical simulation *without any fitting* are $\sigma_1 = 1.34$ and $\sigma_4 = 0.72$. If a weak magnetic field is present ($\beta = 2$), the width of the distribution is predicted to be intermediate between the cases with $\beta = 1, 4$. As seen, the dynamical model follows the prediction. The theoretical value of the standard deviation is $\sigma_2 = 0.90$, the numerical result (without fitting) is $\sigma_2 = 0.99$.

Using the same fit parameters as in Fig. 4.2 we plot the average density of states close to the gap in Fig. 4.3. As seen, the numerical data follow closely the analytical predictions, the deviations becoming significant only outside the universal regime $|E - E_{\rm gap}| \ll E_T$, i.e. $|x| \ll N^{2/3}$. In the absence of magnetic field the spin-orbit coupling induced oscillations are

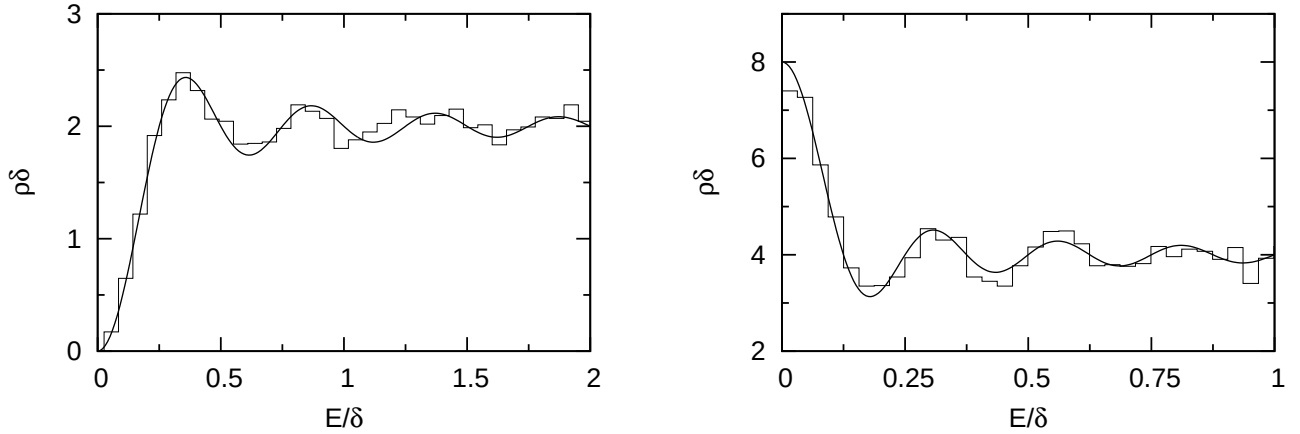

a. DOS in strong magnetic field: without SO coupling b. DOS in strong magnetic field: with SO coupling

Figure 4.4: Average density of states in a magnetic field sufficiently strong to close the excitation gap. Left panel: without spin-orbit coupling; Right panel: with spin-orbit coupling. The smooth curves are the RMT predictions from Eq. (4.7) and the histograms are the results of the simulation (now without any fit parameters).

clearly obtained.

The density of states in a strong magnetic field is given in Fig. 4.4. The magnetic field was characterized by $\theta_0/\theta_c = 25$. The left panel shows the data without spin-orbit coupling [131], and the right panel shows what happens if spin-rotation symmetry is broken. The numerical data follows closely the analytical prediction (4.7) of RMT. In particular the enhanced density of states in the presence of spin-orbit coupling is clearly seen. The first oscillations in the density of states are also captured in the dynamical model. The frequency doubling due to the reduced degeneracy ($s = 2 \to s = 1$) is apparent.

4.5 Conclusion

In conclusion, we have introduced a quantum map for the dynamics of a chaotic quantum dot with spin-orbit coupling connected to a superconductor. We have demonstrated three effects of spin-orbit coupling on the excitation spectrum of this Andreev billiard: The narrowing of the distribution of the excitation gap and the appearance of oscillations in the density of states in the absence of a magnetic field; and the peak in the density of states at the Fermi level in strong magnetic field. Our numerical simulations confirm the predictions of random-matrix theory. The third effect is particularly interesting from an experimental point of view.

In view of the possibility to tune the strength of spin-orbit coupling in quantum dots [5, 6], one can imagine tuning the density of states at the Fermi level from zero to a value of twice the normal density of states.

Chapter 5

Splitting of Andreev levels in a Josephson junction by spin-orbit coupling *

5.1 Introduction

A Josephson junction is a weak link between two superconductors with an adjustable phase difference ϕ. The weak link may be a tunnel barrier or a normal metal. Fig. 5.1 shows, for example, a Josephson junction consisting of a small piece of normal metal (a quantum dot), connected to the superconductors by a pair of narrow constrictions (quantum point contacts). The excitation spectrum below the superconducting gap Δ consists of discrete energies, called Andreev levels. In zero magnetic field, the energy levels ε_n are determined by the normal-state transmission eigenvalues T_n if $\Delta \ll \hbar/\tau_{\rm dw}$, where $\tau_{\rm dw}$ is the dwell time of an electron in the normal region (before it is converted into a hole by Andreev reflection at the superconductor). The relationship is [80]

$$\varepsilon_n = \Delta\sqrt{1 - T_n \sin^2(\phi/2)} + \mathcal{O}(\Delta^2\tau_{\rm dw}/\hbar). \tag{5.1}$$

Each level is twofold spin-degenerate (Andreev doublet).

Recently the effect of spin-orbit coupling on Josephson junctions became a subject of investigation [94, 132, 138–140]. This is a subtle effect for the following reason: On the

*This chapter is submitted to Phys. Rev. B (preprint: arXiv:0709.3054)

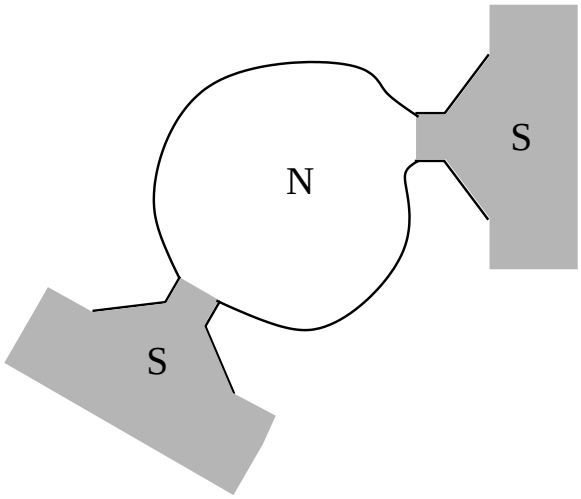

Figure 5.1: Sketch of a quantum dot Josephson junction: the quantum dot (N) is connected to two superconductors (S) by point contacts. Spin-orbit coupling splits the energy levels of the system when the superconductors have a nonzero phase difference.

one hand, in the absence of magnetic fields the normal-state transmission eigenvalues T_n are Kramers degenerate because of the time-reversal invariance of the normal system. On the other hand, one would expect a breaking of the degeneracy of the Andreev doublets because the phase difference between the superconducting contacts breaks the time-reversal symmetry of the system. Still, to leading order in $\Delta\tau_{\rm dw}/\hbar$ the one-to-one relationship (5.1) between ε_n and T_n ensures that the Andreev levels remain degenerate for nonzero ϕ. As was pointed out by Chtchelkatchev and Nazarov [94], to see a splitting of the Andreev doublets as a result of the combined effect of spin-rotation symmetry breaking by spin-orbit coupling and time-reversal symmetry breaking by the phase difference one has to go beyond the leading order in $\Delta\tau_{\rm dw}/\hbar$. This tunable level splitting was exploited in a proposal of Andreev qubits for quantum computation [94].

In this chapter we examine the splitting of the Andreev doublets quantitatively by calculating the first order correction to the energy levels in the small parameter $\Delta\tau_{\rm dw}/\hbar$. We concentrate our attention on the case when the quantum point contacts support one propagating mode each. We give a simple relation between the effective Hamiltonian for the level splitting of Chtchelkatchev and Nazarov [94] and the Wigner-Smith time delay matrix,

$$Q = -iS^\dagger \frac{dS}{d\varepsilon}, \tag{5.2}$$

where S is the scattering matrix of the normal system. As an application, we calculate how the splittings are distributed for an ensemble of systems where the two superconductors are connected by a chaotic quantum dot, assuming that the spin-orbit coupling in the dot is strong enough that the dot Hamiltonian can be modeled as a member of the symplectic ensemble of Random Matrix Theory (RMT) [11,29]. The present study in the regime $\Delta \ll \hbar/\tau_{\rm dw}$ complements earlier work [82,93] in the opposite regime $\Delta \gg \hbar/\tau_{\rm dw}$.

The chapter is organized as follows. In Sec. 5.2 we employ the scattering matrix approach for calculating the first order correction in $\Delta\tau_{\rm dw}/\hbar$ to the Andreev levels, and obtain the effective Hamiltonian for the level splitting in terms of the time delay matrix Q. For simplicity, we consider the single-channel case in Sec. 5.2 and give the multichannel extension in an Appendix. We apply our single-channel formula to a calculation of the splitting distribution for an ensemble of chaotic Josephson junctions in Sec. 5.3. We conclude in Sec. 5.4 with a comparison of the splitting distribution of the Andreev doublets and the Wigner surmise of RMT.

5.2 Splitting Hamiltonian and Wigner-Smith matrix

For energies below the superconducting gap Δ the Josephson junction supports bound states, with excitation energies given by the roots of the secular equation [80]

$$\mathrm{Det}\,\left[\mathbb{I} - \alpha(\varepsilon)^2 r_{\rm A}^* S_{\rm e}(\varepsilon) r_{\rm A} S_{\rm h}(\varepsilon)\right] = 0, \tag{5.3}$$

where

$$\alpha = \exp\left[-i\arccos\left(\frac{\varepsilon}{\Delta}\right)\right],\ r_{\rm A} = \begin{pmatrix} e^{i\phi/2}\mathbb{I} & 0 \\ 0 & e^{-i\phi/2}\mathbb{I} \end{pmatrix}, \tag{5.4}$$

and $S_{\rm e}(\varepsilon)$ and $S_{\rm h}(\varepsilon)$ are the scattering matrices of the normal system for electrons and holes. They are related as

$$S_{\rm h}(\varepsilon) = \mathcal{T} S_{\rm e}(-\varepsilon)\mathcal{T}^{-1}, \tag{5.5}$$

where $\mathcal{T} = i\sigma_2 K$ is the time-reversal operator for spin-1/2 particles. The matrix σ_2 is the second Pauli matrix acting on the spin degree of freedom and K is the operator of complex conjugation. Relation (5.5) reflects the fact that in the normal part the dynamics of the

holes is governed by the Hamiltonian [86]

$$H_{\rm h} = -\mathcal{T} H_{\rm e} \mathcal{T}^{-1}, \tag{5.6}$$

the negative of the time reversed electron Hamiltonian $H_{\rm e}$.

We consider the case when the normal part is time-reversal invariant, which imposes the self duality condition $S = \sigma_2 S^T \sigma_2$ on the scattering matrix. (The superscript T refers to matrix transposition.) The elements of $S_{\rm e}(\varepsilon)$ change significantly if ε is changed on the scale of $\hbar/\tau_{\rm dw}$, therefore to leading order in $\Delta\tau_{\rm dw}/\hbar$ one can neglect the energy dependence of $S_{\rm e}(\varepsilon)$, and take it at the Fermi energy, $S_{\rm e}(\varepsilon) \approx S_{\rm e}(0)$. Making use of the self-duality of the scattering matrix, and introducing the usual block structure

$$S = \begin{pmatrix} r & t' \\ t & r' \end{pmatrix}, \tag{5.7}$$

the secular equation (5.3) can be simplified to [80]

$$\mathrm{Det}\left[\left(1 - \frac{\varepsilon^2}{\Delta^2}\right) - t^\dagger t \sin^2\left(\frac{\phi}{2}\right)\right] = 0. \tag{5.8}$$

From this equation follows the relation (5.1) between the energies and the transmission eigenvalues.

The correction of order $\Delta^2\tau_{\rm dw}/\hbar$ comes from considering the energy dependence of the scattering matrix to first order, $S(\varepsilon) \approx S(0) + (dS/d\varepsilon)\varepsilon$. For simplicity, we restrict ourselves here to the case of two single-channel point contacts. (The extension to multichannel point contacts is given in App. A.) For single-channel point contacts the self-duality of the scattering matrix implies

$$r = \rho \mathbb{I}_2,\ r' = \rho' \mathbb{I}_2,\ t' = \sigma_2 t^T \sigma_2,\ t = \sqrt{T} U, \tag{5.9}$$

where $\rho,\ \rho'$ are complex numbers, $\mathbb{I}_2$ is the 2×2 unit matrix, $1 \geq T \geq 0$ and U is a 2×2 unitary matrix. Writing the energy as $\varepsilon_0 + \delta\varepsilon$ with

$$\varepsilon_0 = \Delta\sqrt{1 - T\sin^2(\phi/2)}, \tag{5.10}$$

and keeping terms up to linear order in the small quantities $\delta\varepsilon = \mathcal{O}(\Delta^2\tau_{\rm dw}/\hbar)$ and $\Delta\tau_{\rm dw}/\hbar$,

one finds the eigenvalue equation

$$\mathrm{Det}\left[\frac{\Delta^2}{4}\left(\sigma_2 Q_{11}^T \sigma_2 - Q_{11}\right)\sin(\phi) - \frac{\Delta^2}{4}(\mathrm{Tr}\ Q)\frac{\varepsilon_0}{\Delta}\sqrt{1-\frac{\varepsilon_0^2}{\Delta^2}}\,\mathbb{I}_2 - \delta\varepsilon\right] = 0 \tag{5.11}$$

for the energy correction $\delta\varepsilon$. The matrix Q has the block structure

$$Q = \begin{pmatrix} Q_{11} & Q_{12} \\ Q_{21} & Q_{22} \end{pmatrix}, \tag{5.12}$$

inherited from the transmission-reflection block structure (5.7) of the scattering matrix.

The second term in the determinant (5.11) shifts both eigenvalues by the same amount $\delta\varepsilon_{\mathrm{shift}}$, while the first, manifestly traceless term is responsible for the splitting $\pm\delta\varepsilon_{\mathrm{split}}$ of the doublet. We see that the splitting is determined by the effective Hamiltonian

$$H_{\mathrm{eff}} = \Delta\frac{\tau_{\mathrm{dw}}\Delta}{\hbar}\ \Sigma\ \sin(\phi), \tag{5.13}$$

with Σ a traceless Hermitian 2×2 matrix having matrix elements of order unity. This is the result of Chtchelkatchev and Nazarov [94]. Our analysis gives an explicit relation [141] between the matrix Σ and the time delay matrix Q,

$$\Sigma = \frac{\hbar}{4\tau_{\mathrm{dw}}}\left(\sigma_2 Q_{11}^T \sigma_2 - Q_{11}\right). \tag{5.14}$$

This is the key relation that will allow us, in the next section, to calculate the level splitting distribution from the known properties of the time delay matrix in a chaotic system.

We conclude this section with a symmetry consideration. The shift $\delta\varepsilon_{\mathrm{shift}}$ is even in ϕ, just like the zeroth order term ε_0. In contrast, the splitting $\delta\varepsilon_{\mathrm{split}}$ is odd in ϕ. This is in accord with the symmetry of the Hamiltonian H that gives the full excitation spectrum of the Josephson junction. Under time reversal, in our case of a time-reversal invariant normal part, it transforms as $\mathcal{T}H(\phi)\mathcal{T}^{-1} = H(-\phi)$, therefore, for an eigenstate Ψ one has

$$\begin{array}{lcl} H(\phi)\Psi(\phi) & = & \varepsilon(\phi)\Psi(\phi), \\ H(\phi)\mathcal{T}\Psi(-\phi) & = & \varepsilon(-\phi)\mathcal{T}\Psi(-\phi). \end{array} \tag{5.15}$$

An Andreev doublet is therefore of the form $\{\varepsilon(\phi), \varepsilon(-\phi)\}$. The decomposition of $\varepsilon(\phi)$

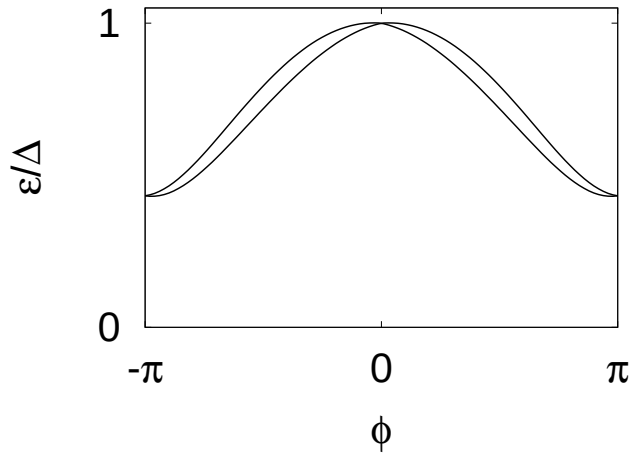

Figure 5.2: A schematic illustration of the splitting of the Andreev doublet as a function of the phase difference ϕ for a single-channel Josephson junction with spin-orbit coupling. The energies are the sum of a degenerate part $\varepsilon_0 + \delta\varepsilon_{\rm shift}$ that is even in ϕ and a splitting $\pm\delta\varepsilon_{\rm split}$ that is odd in ϕ, as explained in the text. The maximal splitting is reached at $\phi = \pi/2$.

into even and odd parts in ϕ amounts to a decomposition of the doublet into a degenerate even part and an odd splitting part. The resulting ϕ dependence of the doublet is shown schematically in Fig. 5.2.

5.3 Splitting distribution in chaotic Josephson junctions

As an application of our general result (5.14) we calculate how the level splittings are distributed for an ensemble of Josephson junctions where the normal part is a chaotic quantum dot. We assume that the spin-orbit coupling inside the dot is strong enough that the dot Hamiltonian can be modeled as a member of the symplectic ensemble of RMT, i.e. that the spin-orbit time $\tau_{\rm so}$ is much shorter than $\tau_{\rm dw}$.

The splitting distribution can be obtained from the known distribution of the scattering matrix [11], and of the dimensionless symmetrized Wigner-Smith matrix [142],

$$Q_E = -i\,\frac{\hbar}{\tau_{\rm dw}}\,S^{-1/2}(dS/d\varepsilon)S^{-1/2}. \tag{5.16}$$

The distributions of S and Q_E are independent [142], which makes it advantageous to express

Q in terms of S and Q_E:

$$Q = \frac{\tau_{\rm dw}}{\hbar} S^{-1/2} Q_E S^{1/2}. \tag{5.17}$$

In the single-channel case one has

$$\begin{aligned} Q_E &= M_1 \begin{pmatrix} 1/\gamma_1 \, \mathbb{I}_2 & 0 \\ 0 & 1/\gamma_2 \, \mathbb{I}_2 \end{pmatrix} M_1^\dagger, \\ S &= M_2 \begin{pmatrix} e^{i\varphi_1} \mathbb{I}_2 & 0 \\ 0 & e^{i\varphi_2} \mathbb{I}_2 \end{pmatrix} M_2^\dagger. \end{aligned} \tag{5.18}$$

The rates γ_n are distributed according to [142]

$$P(\gamma_1, \gamma_2) \propto |\gamma_1 - \gamma_2|^4 \; \gamma_1^4 \gamma_2^4 \; \exp[-4(\gamma_1 + \gamma_2)]. \tag{5.19}$$

The distribution of the phases ϕ_n is [11]

$$P(\phi_1, \phi_2) \propto |e^{i\phi_1} - e^{i\phi_2}|^4. \tag{5.20}$$

The matrices of eigenvectors M_1 and M_2 are members of the group Sp(2) of 4×4 unitary symplectic matrices, and are uniformly distributed with respect to the Haar measure of the group [11, 142]. The Haar measure is given as

$$d\mu \propto \sqrt{|{\rm Det} g|} \Pi_j dx_j, \tag{5.21}$$

in terms of the metric tensor g, defined by

$$\mathrm{Tr}\left(dM dM^\dagger\right) = \sum_{ij} g_{ij} dx_i dx_j. \tag{5.22}$$

Here $\{x_i\}$ is a set of independent variables parameterizing the Sp(2) matrix M.

A convenient choice to parameterize Sp(2) is the decomposition

$$M = \begin{pmatrix} \cos(\theta) & \sin(\theta) \; W \\ -\sin(\theta) \; W & \cos(\theta) \end{pmatrix} \begin{pmatrix} U & 0 \\ 0 & V \end{pmatrix}, \tag{5.23}$$

where W, U and V are SU(2) matrices, and $\theta \in [0, \pi/2]$. It is seen that the SU(2)$\otimes$SU(2)

factor corresponding to the block-diagonal matrix with U and V cancels from the spectral decomposition (5.18) of Q_E and S. Using the Euler angle parameterization for SU(2),

$$U=\begin{pmatrix} e^{-i(\phi_U+\psi_U)/2}\cos(\theta_U/2) & -e^{i(\psi_U-\phi_U)/2}\sin(\theta_U/2) \\ e^{i(\phi_U-\psi_U)/2}\sin(\theta_U/2) & e^{i(\phi_U+\psi_U)/2}\cos(\theta_U/2) \end{pmatrix}, \tag{5.24}$$

$$\phi_U \in [0,2\pi],\ \psi_U \in [0,4\pi],\ \theta_U \in [0,\pi],$$

and similarly for the matrices V, W, one finds that the Haar measure on Sp(2) corresponding to the chosen parameterization is

$$d\mu(M) \propto \sin^3(\theta)\cos^3(\theta)d\theta \prod_{j=U,V,W} \sin(\theta_j)d\phi_j d\theta_j d\psi_j. \tag{5.25}$$

We define the maximal dimensionless splitting q of the Andreev levels (reached at $\phi = \pi/2$) by the formula

$$\delta\varepsilon_{\rm split} = q\Delta\frac{\Delta\tau_{\rm dw}}{\hbar}\sin(\phi). \tag{5.26}$$

The distribution of q is given by

$$P(q) = \int d\mu(S)d\mu(Q_E)\delta(q-\sqrt{-{\rm Det}(\Sigma)}),$$

$$d\mu(Q_E) = d\mu(M_1)d\gamma_1 d\gamma_2 P(\gamma_1,\gamma_2), \tag{5.27}$$

$$d\mu(S) = d\mu(M_2)d\varphi_1 d\varphi_2 P(\varphi_1,\varphi_2).$$

Eq. (5.27) can be evaluated numerically. The resulting distribution is shown in Fig. 5.3. The first two moments of q are

$$\langle q\rangle = 0.181, \quad \sqrt{\langle q^2\rangle - \langle q\rangle^2} = 0.152\ . \tag{5.28}$$

The splitting distribution near zero behaves as

$$P(q) \sim q^2 \quad (q\to 0). \tag{5.29}$$

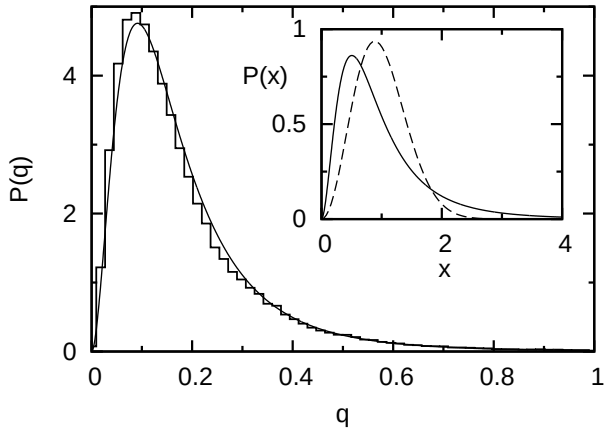

Figure 5.3: Main plot: Distribution of the maximal splitting of the Andreev levels (reached at $\phi = \pi/2$) in units of $\Delta^2\tau_{\rm dw}/\hbar$. The smooth curve is the prediction of Random Matrix Theory calculated from Eq. (5.27), the histogram is the result of a numerical simulation using the spin kicked rotator. Inset: comparison of the Andreev doublet splitting distribution (solid line) and the Wigner surmise (dashed line). For this comparison, the energies are rescaled such that the mean of the distributions is unity.

For large splittings we find

$$P(q) \sim q^{-6} \quad (q \to \infty). \tag{5.30}$$

In order to check our prediction (5.27) for the level splitting distribution, we have numerically simulated the chaotic quantum dot Josephson junction of Fig. 5.1 using the spin kicked rotator [45, 51]. The spin kicked rotator is a dynamical model, from which one can extract scattering matrices characteristic of chaotic cavities. These scattering matrices are given by

$$S(\varepsilon) = \mathcal{P}[e^{-i\varepsilon} - \mathcal{F}(1 - \mathcal{P}^T\mathcal{P})]^{-1}\mathcal{F}\mathcal{P}^T, \tag{5.31}$$

where $\mathcal{F}$ is a $2M \times 2M$ matrix giving the stroboscopic time evolution of the model and $\mathcal{P}$ is a $4 \times 2M$ projection matrix projecting onto the two single-channel point contacts (the factors of 2 in the dimensions are because of the spin). The quasienergy ε plays the role of the energy variable, measured in units of $\hbar/\tau_0$ with τ_0 the stroboscopic time.

Scattering matrices generated through Eq. (5.31) are inserted into the secular Eq. (5.3), and the roots are found by varying the quasienergy. The dwell time in this model is $\tau_{\rm dw} = M/2$ (again in units of τ_0). We take $M = 100$ and $\Delta = 2 \cdot 10^{-4}$ (in units of $\hbar/\tau_0$), so that $\Delta\tau_{\rm dw}/\hbar = 10^{-2} \ll 1$. By sampling about 10^5 different $\mathcal{F}$, P, and ϕ we numerically obtain the

distribution $P(q)$ shown in Fig. 5.3 together with the analytical result (5.27). The agreement is very good.

5.4 Discussion

5.4.1 Summary

We have investigated the effect of spin-orbit coupling on the subgap spectrum of single-channel Josephson junctions. Using the scattering matrix approach and considering the energy dependence of the scattering matrix to first order we obtained a simple relation, Eq. (5.14), between the effective Hamiltonian governing the level splitting and the quantum mechanical time delay matrix $Q = -iS^\dagger dS/d\varepsilon$. This relation allowed us to find the splitting distribution for an ensemble of chaotic Josephson junctions using the known properties of Q. We verified our result numerically by simulating the chaotic Josephson junction using the spin kicked rotator, and we found excellent agreement.

5.4.2 Comparison of the splitting distribution with the Wigner surmise

In the inset of Fig. 5.3 we compare the splitting distribution of the Andreev doublet with the Wigner surmise of RMT [29],

$$P_{\mathrm{W}}(x) = \frac{32}{\pi^2}\, x^2\, \exp\left(-\frac{4x^2}{\pi}\right). \tag{5.32}$$

(For this comparison the energy scale is set such that the average splitting is unity.) The motivation behind this comparison is the fact that the Wigner surmise is also a splitting distribution: as shown in App. B it describes the distribution of the splittings of Kramers doublets for normal chaotic quantum dots with spin-orbit coupling in the case that the time-reversal symmetry is broken by a magnetic field.

At small splittings, both P and P_{W} decay quadratically. This quadratic decay is a generic feature of the splitting of a Kramers degenerate level due to time-reversal symmetry breaking. It follows from the fact that the splitting Hamiltonian is a 2×2 Hermitian traceless matrix without further symmetries and from a power counting argument [143] similar to the one leading to the quadratic decay of P_{W}.

While at small splittings the two distributions decay in the same way, we find qualitative differences in the opposite limit. At large splittings P decays like a power law in contrast to the exponential decay of P_{W} [cf. Eqs. (5.30) and (5.32)].

We attribute the deviation of P from the Wigner surmise to the nonuniform way in which time-reversal symmetry is broken: While the magnetic field in App. B acts *uniformly* throughout the normal quantum dot, the superconducting phase difference in the Josephson junction acts *nonuniformly* at the point contacts.

Appendix A: Splitting Hamiltonian for multichannel Josephson junctions

We generalize the relation (5.14) between the splitting Hamiltonian and the time delay matrix to the case that each of the two point contacts supports $N/2$ propagating modes. (The single-channel case of Sec. 5.2 therefore corresponds to $N = 2$.) In the multichannel case, after the steps leading to Eq. (5.11) one arrives at the equation

$$\mathrm{Det}\left[H_0 + \frac{\Delta^2}{2}\, K - \delta\varepsilon\right] = 0, \tag{5.33}$$

where

$$H_0 = \frac{\Delta^2}{2\varepsilon_n^{(0)}}\left[1 - \left(\frac{\varepsilon_n^{(0)}}{\Delta}\right)^2 - t^\dagger t \sin^2\left(\frac{\phi}{2}\right)\right], \tag{5.34}$$

$$\varepsilon_n^{(0)} = \Delta\sqrt{1 - T_n \sin^2(\phi/2)}, \tag{5.35}$$

and K is a matrix with elements of order $\tau_{\mathrm{dw}}/\hbar$. An eigenvector of $t^\dagger t$ with eigenvalue T_n is also an eigenvector of H_0 with zero eigenvalue. The first order correction to the zeroth order energy $\varepsilon_n^{(0)}$ is the first order perturbative correction to this zero eigenvalue.

We introduce the $N \times 2$ matrices W_n and W_n' which contain the two orthonormal eigenvectors of, respectively, $t^\dagger t$ and $t'^\dagger t'$, both corresponding to the eigenvalue T_n. In terms of these matrices we define the matrices q_{1n} and q_{2n} by

$$q_{1n} = W_n^\dagger Q_{11} W_n, \quad q_{2n} = W_n'^\dagger Q_{22} W_n' \,. \tag{5.36}$$

We find that the shift of the Andreev doublet at $\varepsilon_n^{(0)}$ is given by

$$\delta\varepsilon_n^{\rm shift} = -\frac{\Delta^2}{4}\frac{\varepsilon_n^{(0)}}{\Delta}\sqrt{1-\left(\varepsilon_n^{(0)}/\Delta\right)^2}\,(\mathrm{Tr}\; q_{1n} + \mathrm{Tr}\; q_{2n})\,, \tag{5.37}$$

while the splitting $\delta\varepsilon_n^{\rm split}$ is given by the two eigenvalues of the traceless Hermitian matrix

$$H_{\rm eff}^{(n)} = \frac{\Delta^2}{4}\left(\sigma_2\; q_{1n}^T\sigma_2 - q_{1n}\right)\sin(\phi). \tag{5.38}$$

Appendix B: Splitting distribution for normal chaotic quantum dots

We calculate the splitting distribution of a Kramers degenerate level for normal chaotic quantum dots with spin-orbit coupling, in the case that the time-reversal symmetry is broken by a weak perpendicular magnetic field.

The Hamiltonian of the system is decomposed into two parts,

$$H = H_0 + A, \qquad H_0^\dagger = H_0,\;\; A^\dagger = A, \tag{5.39}$$

where H_0 and A are $2M \times 2M$ matrices (the factor of two is due to the spin). They satisfy

$$\mathcal{T}H_0\mathcal{T}^{-1} = H_0, \quad \mathcal{T}A\mathcal{T}^{-1} = -A. \tag{5.40}$$

The matrix H_0 models the time-reversal invariant part of the Hamiltonian and A is a time-reversal symmetry breaking term.

The eigenvalues of H_0 are doubly degenerate (Kramers degeneracy). Considering a doublet with energy E_0, with corresponding eigenvectors u_1, $u_2 = \mathcal{T}u_1$,

$$H_0u_1 = E_0u_1, \quad H_0u_2 = E_0u_2, \tag{5.41}$$

and treating A as a perturbation, first order degenerate perturbation theory leads to the splitting of the Kramers doublet by an amount $\pm\delta\varepsilon_{\rm split}$. We find

$$\delta\varepsilon_{\rm split} = \sqrt{\langle u_1, Au_1\rangle^2 + |\langle u_1, Au_2\rangle|^2}. \tag{5.42}$$

For chaotic billiards, the splitting distribution is given by [29]

$$P(\lambda) = \int dU\ \rho(U) \int dA\ P(A)\delta\big(\lambda - \delta\varepsilon_{\rm split}\big), \tag{5.43}$$

where U is the matrix of eigenvectors of H_0, distributed according to $\rho(U)$. (The form of $\rho(U)$ is not needed for the derivation.) The matrix A has distribution

$$P(A) \propto \exp\left(-v^2 {\rm Tr}\ A^2\right), \tag{5.44}$$

where v is a positive number. Using the fact that $P(A)dA$ is invariant under a unitary transformation with the matrix of eigenvectors of H_0, one finds

$$P(\lambda) = \int da\ db\ dc\ P(a,b,c)\delta(\lambda - \sqrt{a^2+b^2+c^2}), \tag{5.45}$$

where

$$P(a,b,c) \propto \exp[-2v^2(a^2+b^2+c^2)]. \tag{5.46}$$

After changing to polar coordinates the integral (5.45) can be evaluated straightforwardly, and after rescaling from λ to x, defined by $\int dx\ P(x)x = 1$, one arrives at the Wigner surmise (5.32).

Bibliography

[1] D. Awschalom, D. Loss, and N. Samarth, *Semiconductor Spintronics and Quantum Computation* (Springer, 2002).

[2] marcuslab.harvard.edu/research.shtml.

[3] H.-A. Engel, E. I. Rashba, and B. I. Halperin, *Handbook of Magnetism and Advanced Magnetic Materials* (John Wiley & Sons Ltd, Chichester, UK, 2007), chap. Theory of Spin Hall Effects in Semiconductors, pp. 2858–2877.

[4] C. W. J. Beenakker and H. van Houten, Solid State Phys. **44**, 1 (1991).

[5] D. M. Zumbühl, J. B. Miller, C. M. Marcus, K. Campman, and A. C. Gossard, Phys. Rev. Lett. **89**, 276803 (2002).

[6] J. B. Miller, D. M. Zumbuhl, C. M. Marcus, Y. B. Lyanda-Geller, D. Goldhaber-Gordon, K. Campman, and A. C. Gossard, Phys. Rev. Lett. **90**, 076807 (2003).

[7] D. M. Zumbühl, J. B. Miller, C. M. Marcus, D. Goldhaber-Gordon, J. S. Harris, K. Campman, and A. C. Gossard, Phys. Rev. B **72**, 081305 (R) (2005).

[8] R. Winkler, *Spin-Orbit Coupling effects in Two-Dimensional Electron and Hole Systems* (Springer, 2003).

[9] W. Knap, C. Skierbiszewski, A. Zduniak, E. Litwin-Staszewska, D. Bertho, F. Kobbi, J. L. Robert, G. E. Pikus, F. G. Pikus, S. V. Iordanskii, *et al.*, Phys. Rev. B **53**, 3912 (1996).

[10] J. J. Krich and B. I. Halperin, Arxiv preprint cond-mat/0702667 (2007).

[11] C. W. J. Beenakker, Rev. Mod. Phys. **69**, 731 (1997).

[12] R. Landauer, IBM J. Res. Dev **1**, 223 (1957).

[13] R. Landauer, Z. Phys. B **68**, 217 (1987).

[14] Y. Imry, in G. Grinstein and G. Mazenko, eds., *Directions in Condensed Matter Physics* (World Scientific, Singapore, 1986), p. 101.

[15] M. Büttiker, Phys. Rev. Lett. **57**, 1761 (1986).

[16] M. Büttiker, IBM J. Res. Dev. **32**, 317 (1988).

[17] M. Büttiker, Phys. Rev. Lett. **65**, 2901 (1990).

[18] G. Bergmann, Sol. State Commun. **42**, 815 (1982).

[19] B. L. Altshuler and B. D. Simons, in E. Akkermans, J.-L. Pichard, and J. Zinn-Justin, eds., *Mesoscopic Quantum Physics* (North-Holland, Amsterdam, 1995).

[20] S. Hikami, A. Larkin, and Y. Nagaoka, Prog. Theor. Phys. **63**, 707 (1980).

[21] G. Bergmann, Phys. Rep **107**, 1 (1984).

[22] E. P. Wigner, Can. Math. Congr. Proc., University of Toronto Press, Toronto, Canada pp. 174–184 (1957).

[23] O. Bohigas, M. J. Giannoni, and C. Schmit, Phys. Rev. Lett. **52**, 1 (1984).

[24] K. B. Efetov, Sov. Phys. JETP **56**, 467 (1982).

[25] K. B. Efetov, Adv. in Phys. **32**, 53 (1983).

[26] A. V. Andreev, O. Agam, B. D. Simons, and B. L. Altshuler, Phys. Rev. Lett. **76**, 3947 (1996).

[27] S. Müller, S. Heusler, P. Braun, F. Haake, and A. Altland, Phys. Rev. Lett. **93**, 014103 (2004).

[28] S. Müller, S. Heusler, P. Braun, F. Haake, and A. Altland, Phys. Rev. E **72**, 046207 (2005).

[29] M. L. Mehta, *Random Matrices* (Elsevier Ltd., 2004), 3rd ed.

[30] Z. Pluhař, H. A. Weidenmüller, J. A. Zuk, and C. H. Lewenkopf, Phys. Rev. Lett. **73**, 2115 (1994).

[31] I. L. Aleiner and V. I. Fal'ko, Phys. Rev. Lett. **87**, 256801 (2001), **89**, 079902(E) (2002).

[32] K. M. Frahm and J.-L. Pichard, J. Phys. I **5**, 847 (1995).

[33] O. Agam, I. Aleiner, and A. Larkin, Phys. Rev. Lett. **85**, 3153 (2000).

[34] P. G. Silvestrov, M. C. Goorden, and C. W. J. Beenakker, Phys. Rev. B **67**, 241301 (2003).

[35] R. S. Whitney and P. Jacquod, Physical Review Letters **96**, 206804 (2006).

[36] A. Ossipov, J. H. Bardarson, J. Tworzydlo, M. Titov, and C. W. J. Beenakker, Europhys. Lett. **76**, 115 (2006).

[37] C. Mahaux and H. A. Weidenmüller, *Shell-model approach to nuclear reactions* (North-Holland, 1969).

[38] J. J. M. Verbaarschot, H. A. Weidenmüller, and M. R. Zirnbauer, Physics Reports **129**, 367 (1985).

[39] P. W. Brouwer, Phys. Rev. B **51**, 16878 (1995).

[40] H. U. Baranger and P. A. Mello, Phys. Rev. Lett. **73**, 142 (1994).

[41] P. W. Brouwer, K. M. Frahm, and C. W. J. Beenakker, Waves in Random Media **9**, 91 (1999).

[42] E. Ott, *Chaos in Dynamical Systems* (Cambridge University Press, 2002).

[43] S. Ree and L. E. Reichl, Phys. Rev. E **60**, 1607 (1999).

[44] F. M. Izrailev, Phys. Rep. **196**, 299 (1990).

[45] R. Scharf, J. Phys. A **22**, 4223 (1989).

[46] M. Thaha, R. Blümel, and U. Smilansky, Phys. Rev. E **48**, 1764 (1993).

[47] Y. V. Fyodorov and H.-J. Sommers, JETP Lett. **72**, 422 (2000).

[48] A. Ossipov, T. Kottos, and T. Geisel, Europhys. Lett. **62**, 719 (2003).

[49] P. Jacquod, H. Schomerus, and C. W. J. Beenakker, Phys. Rev. Lett. **90**, 207004 (2003).

[50] J. Tworzydło, A. Tajic, H. Schomerus, and C. W. J. Beenakker, Phys. Rev. B **68**, 115313 (2003).

[51] J. H. Bardarson, J. Tworzydlo, and C. W. J. Beenakker, Phys. Rev. B **72**, 235305 (2005).

[52] I. L. Aleiner, P. W. Brouwer, and L. I. Glazman, Physics Reports **358**, 309 (2002).

[53] A. G. Huibers, S. R. Patel, C. M. Marcus, P. W. Brouwer, C. I. Duruöz, and J. S. Harris, Phys. Rev. Lett. **81**, 1917 (1998).

[54] B. L. Altshuler, A. G. Aronov, and D. E. Khmelnitsky, J. Phys. C **15**, 7367 (1982).

[55] B. L. Altshuler and A. G. Aronov, in *Electron-Electron Interaction in Disordered Systems*, edited by A. L. Efros and M. Pollak (North Holland, Amsterdam) p. 1 (1985).

[56] M. Büttiker, Phys. Rev. B **33**, 3020 (1986).

[57] M. Büttiker, IBM J. Res. Dev. **32**, 63 (1988).

[58] C. M. Marcus, R. M. Westervelt, P. F. Hopkins, and A. C. Gossard, Phys. Rev. B **48**, 2460 (1993).

[59] H. U. Baranger and P. A. Mello, Phys. Rev. B **51**, 4703 (1995).

[60] P. W. Brouwer and C. W. J. Beenakker, Phys. Rev. B **51**, 7739 (1995).

[61] P. W. Brouwer and C. W. J. Beenakker, Phys. Rev. B **55**, 4695 (1997).

[62] D. S. Golubev and A. D. Zaikin, Phys. Rev. Lett. **81**, 1074 (1998).

[63] I. L. Aleiner, B. L. Altshuler, and M. E. Gershenson, Phys. Rev. Lett. **82**, 3190 (1999).

[64] D. S. Golubev and A. D. Zaikin, Phys. Rev. Lett. **82**, 3191 (1999).

[65] D. S. Golubev and A. D. Zaikin, Phys. Rev. B **59**, 9195 (1999).

[66] D. S. Golubev and A. D. Zaikin, Phys. Rev. B **62**, 14061 (2000).

[67] D. S. Golubev, A. D. Zaikin, and G. Schön, J. Low Temp. Phys. **126**, 1355 (2002).

[68] I. L. Aleiner, B. L. Altshuler, and M. G. Vavilov, J. Low Temp. Phys. **126**, 1377 (2002).

[69] D. S. Golubev and A. D. Zaikin, J. Low Temp. Phys. **132**, 11 (2003), cond-mat/0208140.

[70] I. Aleiner, B. Altshuler, and M. Vavilov, Arxiv preprint cond-mat/0208264 (2002).

[71] T. R. Kirkpatrick and D. Belitz, Phys. Rev. B **65**, 195123 (2002), cond-mat/0111398.

[72] D. S. Golubev, A. D. Zaikin, and G. Schön, Arxiv preprint cond-mat/0111527 (2001).

[73] Y. Imry, Arxiv preprint cond-mat/0202044 (2002).

[74] P. Mohanty, E. M. Q. Jariwala, and R. A. Webb, Phys. Rev. Lett. **78**, 3366 (1997).

[75] P. Mohanty and R. A. Webb, Phys. Rev. B **55**, R13452 (1997).

[76] A. G. Huibers, J. A. Folk, S. R. Patel, C. M. Marcus, C. I. Duruöz, and J. S. Harris, Phys. Rev. Lett. **83**, 5090 (1999).

[77] J.-H. Cremers, P. W. Brouwer, and V. I. Fal'ko, Phys. Rev. B **68**, 125329 (2003).

[78] C. W. J. Beenakker, Lect. Notes Phys. **667**, 131 (2005).

[79] A. F. Andreev, Zh. Eksp. Teor. Fiz. **46**, 1823 (1964).

[80] C. W. J. Beenakker, Phys. Rev. Lett. **67**, 3836 (1991), **68**, 1442(E) (1992).

[81] A. Altland and M. R. Zirnbauer, Phys. Rev. Lett. **76**, 3420 (1996).

[82] A. Altland and M. R. Zirnbauer, Phys. Rev. B **55**, 1142 (1997).

[83] J. A. Melsen, P. W. Brouwer, K. M. Frahm, and C. W. J. Beenakker, Europhys. Lett. **35**, 7 (1996).

[84] J. A. Melsen, P. W. Brouwer, K. M. Frahm, and C. W. J. Beenakker, Physica Scripta **T69**, 223 (1997).

[85] C. W. J. Beenakker, in: Transport phenomena in Mesoscopic Systems, edited by H. Fukuyama and T. Ando (Springer, Berlin) p. 235 (1992).

[86] P. G. de Gennes, *Superconductivity of Metals and Alloys* (Benjamin, New York, 1966).

[87] K. K. Likharev, Rev. Mod. Phys. **51**, 101 (1979).

[88] R. A. Jalabert, J. L. Pichard, and C. W. J. Beenakker, Europhys. Lett. **27**, 255 (1994).

[89] B. Béri and J. Cserti, Phys. Rev. B **74**, 235314 (2006).

[90] B. Béri and J. Cserti, Phys. Rev. B **75**, 041308 (2007).

[91] C. A. Tracy and H. Widom, Commun. Math. Phys. **177**, 727 (1996).

[92] M. G. Vavilov, P. W. Brouwer, V. Ambegaokar, and C. W. J. Beenakker, Phys. Rev. Lett. **86**, 874 (2001).

[93] B. Béri, J. H. Bardarson, and C. W. J. Beenakker, Phys. Rev. B **75**, 165307 (2007).

[94] N. M. Chtchelkatchev and Y. V. Nazarov, Phys. Rev. Lett. **90**, 226806 (2003).

[95] B. Béri, J. H. Bardarson, and C. W. J. Beenakker, arXiv:0709.3054 (2007).

[96] H. Mathur and A. D. Stone, Phys. Rev. Lett. **68**, 2964 (1992).

[97] P. W. Brouwer, J. N. H. J. Cremers, and B. I. Halperin, Phys. Rev. B **65**, 081302 (2002).

[98] Y. V. Nazarov, Phys. Rev. B **52**, 4720 (1995).

[99] Y. M. Blanter, H. Schomerus, and C. W. J. Beenakker, Physica E **11**, 1 (2001).

[100] K. E. Nagaev, P. Samuelsson, and S. Pilgram, Phys. Rev. B **66**, 195318 (2002).

[101] Regarding the relation between the spin-orbit time $\tau_{\rm SO}$ and the Rashba/Dresselhaus parameters we refer to Refs. [77,97].

[102] Y. M. Blanter and M. Büttiker, Physics Reports **336**, 1 (2000).

[103] H. Lee, L. S. Levitov, and A. Y. Yakovets, Phys. Rev. B **51**, 4079 (1995).

[104] P. W. Brouwer and C. W. J. Beenakker, J. Math. Phys. **37**, 4904 (1996).

[105] Y. V. Nazarov, in H. A. Cerdeira, B. Kramer, and G. Schön, eds., *Quantum Dynamics of Submicron Structures* (Kluwer, Dordrecht, 1995), vol. 291 of NATO ASI Series E: Appl. Sci.

[106] P. Braun, S. Heusler, S. Müller, and F. Haake, J. Phys. A **39**, L159 (2006).

[107] C. W. J. Beenakker and C. Schönenberger, Phys. Today **56**, 37 (2003).

[108] M. J. M. de Jong and C. W. J. Beenakker, Phys. Rev. B **46**, 13400 (1992).

[109] A. M. S. Macêdo, Phys. Rev. B **49**, 1858 (1994).

[110] A. M. S. Macêdo and J. T. Chalker, Phys. Rev. B **49**, 4695 (1994).

[111] A. M. S. Macêdo, Phys. Rev. Lett. **79**, 5098 (1997).

[112] B. I. Halperin, A. Stern, Y. Oreg, J. N. H. J. Cremers, J. A. Folk, and C. M. Marcus, Phys. Rev. Lett. **86**, 2106 (2001).

[113] J. A. Folk, S. R. Patel, K. M. Birnbaum, C. M. Marcus, C. I. Duruöz, and J. S. Harris, Phys. Rev. Lett. **86**, 2102 (2001).

[114] We note that in the classical regime when $\tau_{\rm E}$ is comparable to $\tau_{\rm dw}$, the effect of spin-orbit coupling on the shot noise is qualitatively different from a weak localization correction, see Ref. [36].

[115] C. W. J. Beenakker and H. van Houten, Phys. Rev. B **43**, 12066 (1991).

[116] Y. M. Blanter and E. V. Sukhorukov, Phys. Rev. Lett. **84**, 1280 (2000).

[117] R. G. Nazmitdinov, H.-S. Sim, H. Schomerus, and I. Rotter, Phys. Rev. B **66**, 241302(R) (2002).

[118] P. Jacquod and E. V. Sukhorukov, Phys. Rev. Lett. **92**, 116801 (2004).

[119] E. V. Sukhorukov and O. M. Bulashenko, Phys. Rev. Lett. **94**, 116803 (2005).

[120] F. Aigner, S. Rotter, and J. Burgdörfer, Phys. Rev. Lett. **94**, 216801 (2005).

[121] S. Oberholzer, E. V. Sukhorukov, C. Strunk, C. Schönenberger, T. Heinzel, and M. Holland, Phys. Rev. Lett. **86**, 2114 (2001).

[122] S. Oberholzer, E. V. Sukhorukov, and C. Schönenberger, Nature **415**, 765 (2002).

[123] D. V. Savin and H.-J. Sommers, Phys. Rev. B **73**, 081307 (2006).

[124] Z. Pluhar, H. A. Weidenmüller, J. A. Zuk, C. H. Lewenkopf, and F. J. Wegner, Ann. Phys. (N.Y.) **243**, 1 (1995).

[125] K. M. Frahm, Europhys. Lett. **30**, 457 (1995).

[126] S. Heusler, S. Müller, P. Braun, and F. Haake, Phys. Rev. Lett. **96**, 066804 (2006).

[127] V. A. Khlus, Sov. Phys. JETP **66**, 1243 (1987).

[128] G. B. Lesovik, JETP Lett. **49**, 592 (1989).

[129] M. L. Polianski and P. W. Brouwer, J. Phys. A **36**, 3215 (2003).

[130] K. M. Frahm, P. W. Brouwer, J. A. Melsen, and C. W. J. Beenakker, Phys. Rev. Lett. **76**, 2981 (1996).

[131] M. C. Goorden, P. Jacquod, and C. W. J. Beenakker, Phys. Rev. B **72**, 064526 (2005).

[132] O. V. Dimitrova and M. V. Feigel'man, JETP **102**, 652 (2006).

[133] A. Edelman and P.-O. Persson, math-ph/0501068.

[134] P. J. Forrester, T. Nagao, and G. Honner, Nucl. Phys. B **553**, 601 (1999).

[135] C. A. Tracy and H. Widom, Ann. Inst. Fourier (Grenoble) **55**, 2197 (2005).

[136] A. Kormanyos, Z. Kaufmann, C. J. Lambert, and J. Cserti, Phys. Rev. B **70**, 052512 (2004).

[137] Ref. [49] reported good agreement for the $\beta = 1$ gap distribution between RMT and the Andreev kicked rotator — without any need to fit $E_{\rm gap}$ and $\Delta_{\rm gap}$. We now believe that this good agreement was fortuitous, and that some 5–10% variation of these parameters is needed for a good agreement.

[138] E. V. Bezuglyi, A. S. Rozhavsky, I. D. Vagner, and P. Wyder, Phys. Rev. B **66**, 052508 (2002).

[139] I. V. Krive, S. I. Kulinich, R. I. Shekhter, and M. Jonson, J. Low Temp. Phys. **30**, 554 (2004).

[140] L. Dell'Anna, A. Zazunov, R. Egger, and T. Martin, Phys. Rev. B **75**, 085305 (2007).

[141] With a little algebra one can show that the replacement of Q_{11} with Q_{22} in the definition (5.14) of Σ amounts to a unitary transformation. It is, therefore, a matter of choice to use Q_{11} or Q_{22} to obtain the level splitting.

[142] P. W. Brouwer, K. M. Frahm, and C. W. J. Beenakker, Phys. Rev. Lett. **78**, 4737 (1997).

[143] F. Haake, *Quantum Signatures of Chaos*, Springer Series in Synergetics (Springer, 2001), 2nd ed.

Summary

This thesis reports on our research on the effects of spin-orbit coupling in chaotic quantum dots. The material presented in the thesis can be divided to two parts. The first part deals with quantum transport through chaotic quantum dots, with the focus being on the weak localization - weak antilocalization transition of linear statistics. Using Random Matrix Theory (RMT) we have analytically investigated the transition as a function of spin-orbit coupling strength and magnetic field. We concentrated our attention on the limit of large number of modes in the pair of point contacts connecting the dot to the electron reservoirs. In the case that the contacts support the same number of modes we calculated $\delta\rho(T)$, the weak localization correction to the density of transmission eigenvalues, in the crossover between Dyson's three standard symmetry classes. We found that the singular nature of $\delta\rho(T)$ in the known limit of pure symmetry classes persists to the crossover regime, whereas the type of the singularity changes from Dirac delta peaks at the endpoints of the transmission eigenvalue spectrum to a broadened, inverse square root eigenvalue dependence. The shot noise was investigated in a more general situation, i.e., the transitions were allowed to interpolate between the extended symmetry classes identified by Aleiner and Falko, and the number of modes in the contacts could be different. We found that the ratio of the weak localization correction to the shot noise power to the weak localization correction to the conductance is independent of the degree and the way time-reversal and spin-rotation symmetries are broken, it depends only on the number of modes in the contacts.

The second part of the thesis deals with the spectral properties of normal-superconducting heterostructures, so-called Andreev quantum dots. We have introduced the spin Andreev map which describes the dynamics of a chaotic Andreev quantum dot with spin-orbit coupling in the limit that the superconducting gap Δ is much larger than the inverse dwell time $\hbar/\tau_{\rm dw}$. Using the spin Andreev map we have demonstrated the effects of spin-orbit coupling on the distribution of the excitation gap and on the average density of states. These effects have been predicted by RMT but have not been confirmed in a dynamical model before. Our other study concentrated on the limit $\Delta \ll \hbar/\tau_{\rm dw}$. We have investigated the splitting of Andreev levels in a Josephson junction by spin-orbit coupling. We have established a simple relation between the effective Hamiltonian for the splitting and the Wigner-Smith time delay matrix. We calculated the distribution of splittings for an ensemble of chaotic single-channel Josephson junctions with strong spin-orbit coupling. We found that for small splittings universality dictates a quadratic decay of the distribution, similar to the case of normal dots with magnetic field split Kramers doublets. For large splittings, however, the behavior of the distribution is markedly different, it has a power law tail in Josephson junctions, in contrast to the exponential decay in normal dots.

Összefoglalás

Doktori disszertációm a spin-pálya csatolással kapcsolatos, kaotikus kvantum dotokban fellépő effektusok témájában folytatott kutatásainkat foglalja össze. A dolgozat két részre osztható. Az első rész a kvantum dotokon keresztüli kvantum transzporttal foglalkozik, a hangsúlyt a lineáris statisztikák gyenge lokalizáció – gyenge antilokalizáció átmenetére helyezve. Véletlen mátrix elmélet (RMT) segítségével analitikusan vizsgáltuk az átmenet mágneses tértől és a spin-pálya csatolás erősségétől való függését. Figyelmünk középpontjába azt az esetet helyeztük, mikor a dotot az elektronrezervoárokhoz csatoló két pontkontaktusban a módusok száma jóval nagyobb egynél. Feltéve, hogy a két pontkontaktusban a módusszám megegyezik, kiszámoltuk $\delta\rho(T)$-t, a transzmissziós sajátérték-sűrűség gyenge lokalizációs korrekcióját Dyson három szimmetriaosztálya közti átmenetekre. Azt találtuk, hogy $\delta\rho(T)$ a szimmetriaosztályok határeseteiben mutatott ismert szinguláris viselkedése az átmenetekben sem tűnik el, jóllehet a szingularitás típusa megváltozik, a transzmissziós sajátérték spektrum szélein elhelyezkedő Dirac-delták inverz gyökfüggésű csúcsokká szélesednek. A sörétzaj vizsgálatát általánosabb helyzetre végeztük, az átmenetek történhettek Aleiner és Falko általánosított szimmetriaosztályai között, és a módusszám sem kellett, hogy egyezzen a két pontkontaktusban. Azt találtuk, hogy a sörétzaj és a vezetőképesség gyenge lokalizációs korrekciójának hányadosa nem függ az időtükrözési és a spinforgatási szimmetriák sérülésének módjától, sem mértékétől, a hányadost a pontkontaktusokban levő módusok száma meghatározza.

A dolgozat második fele normál-szupravezető heterostruktúrák, úgynevezett Andreev kvantum dotok spektrális tulajdonságait vizsgálja. A spin-pálya csatolással is jellemezhető dotok dinamikájának leírására bevezettük a spin-Andreev leképezést. Ez a modell arra a határesetre érvényes, mikor a szupravezető gap Δ jóval nagyobb, mint az inverz szökési idő $\hbar/\tau_{\mathrm{dw}}$. A spin-Andreev leképezés segítségével kimutattunk spin-pálya csatolás okozta, a gerjesztési spektrum gap-eloszlásában és az átlagos állapotsűrűségben fellépő effektusokat. Az effektusokra RMT jóslatok álltak rendelkezésre, munkánk ezek első, dinamikai modellen alapuló igazolása. A témában végzett második kutatásunk a $\Delta \ll \hbar/\tau_{\mathrm{dw}}$ határesetre összpontosított. Vizsgálatunk tárgya Josephson-átmenetek Andreev-szintjeinek spin-pálya csatolás jelenlétében történő felhasadása volt. Levezettünk egy egyszerű összefüggést a Wigner-Smith mátrix és a felhasadást meghatározó effektív Hamilton operátor között. Ezt felhasználva kiszámoltuk a felhasadások eloszlását kaotikus egycsatornás Josephson-átmenetekre erős spin-pálya csatolás esetén. Azt találtuk, hogy kis felhasadásokra az univerzalitás az eloszlás négyzetes lecsengését írja elő, normál dotok Kramers-kettőseinek mágneses térben történő felhasadásához hasonlóan. Nagy felhasadásokra azonban szembetűnően más az eloszlás viselkedése, hatványfarkú Josephson-átmenetekben, szemben a normál dotokbeli exponenciális lecsengéssel.